Transport Phenomena of Lithium Metal and Solid Electrolyte in All-Solid-State Batteries

By

Wahid Zaman

Dissertation
Submitted to the Faculty of the
Graduate School of Vanderbilt University
in partial fulfillment of the requirements
for the degree of

DOCTOR OF PHILOSOPHY
in
Mechanical Engineering

December 17, 2022

Nashville, Tennessee

Approved:

Kelsey B. Hatzell, Ph.D.

Deyu Li, Ph.D.

Jason Valentine, Ph.D.

Carlos Silvera Batista, Ph.D.

David Cliffel, Ph.D.

Dedication

I dedicate this thesis to my loving parents, Nurun Naher and Obaid Ullah. I would not be here without their blessings and unconditional love.

Acknowledgment

I would like to thank my Ph.D. advisor, Dr. Kelsey Hatzell, for her guidance, help, encouragement, and support throughout this journey. I am grateful for the opportunity she has given me to explore my research interests in the realm of energy storage systems. Dr. Hatzell's dynamic, innovative and unique style of mentoring has significantly improved my problem-solving skills and research acumen over the years, which will surely have a long-lasting impact on my career ahead. I thank her for sharing her enthusiasm for research which molded me into a thinker and a scholar. I would also like to thank my committee members: Dr. Deyu Li, Dr. Jason Valentine, Dr. Carlos Silvera Batista, and Dr. David Cliffel. I highly appreciate their feedback, critical assessments, and evaluations to make this work impactful.

It is impossible to deny the tremendous amount of impact my coworkers and friends have made throughout this journey. I thank my "solid-state" brethren, Dr. Marm Dixit, for his mentoring, help, and friendship over the years. I thank Dr. Fengyu Shen for teaching me all the necessary skills I needed to kickstart my research work. I thank Dr. Nicholas Hortance, Yanjie Zheng, and Brice Harkey for their support and help on the projects I have worked on. Working with these people has been a privilege and I am also grateful for their friendships. I also thank the youngsters in our lab whom I had the good fortune to mentor: Xinlin Zhong, Stella Vujic, Devon Campbell, Latif Gbadamoshie, and Kyra Owensby.

I would like to thank our collaborators who made significant contributions to this work over the years; Dr. Marta Hatzell, Yousuf Bootwala, Carol Liu, Ray Matsumoto, Matt Thompson, Dr. Peter Cummings, Le Zhao, Dr. Jane Wang, and Dr. Stephen Harris. I gratefully acknowledge the help and guidance of our National Lab collaborators; Dr. Ethan Crumlin, Dr. Slavomir Nemsak and Dr. Lorenz Falling from LBNL, Dr. Anton

Ievlev from ORNL, and Dr. Vincent De Andrade from ANL. I gratefully acknowledge the financial support of the National Science Foundation (NSF), the Department of Energy (DOE), and Toyota North American Research Institute (TRINA). I also would like to thank my masters advisor from Georgia Southern University, Dr. Mujibur Khan, for giving me the opportunity to start as an independent researcher.

This grad life has been busy but worthwhile because of the good people I call my friends. A big "Thank You" to the honorable people of the “Unhappy Coffee hours”: Matt Galazzo, Nicole Moehring, Katie Browning, Alberto Linares, Lucinda Pastora, Lihong Bishop, Andrew Naclerio, Steve Culver, David Zimenecki, Murtaza Zohair, Matt Fitzgerald, Elena Kovalik, Carcia Carson, Janna Eaves, Dan Shae, Mars Pullen, Garrett Marshall, John Williams and Ben Hacker for their unwavering friendship. I also thank the VINSE people; Dr. Alice Leach, William Martinez, Kurt Heinrich, Dr. James Mcbride, and Dr. Tony Hmelo to teach me the invaluable skill sets for electron microscopy and cleanroom techniques. I also thank the people in administration in ME department and ISSS; Dr. Eric Barth, Myrtle Daniels, Sarah Nagy, Melody Kekez, Chris Lindsey and Radhika Reddy to take care of my paperwork over the years. Thanks to the evergreen people of the Bangladeshi Community in Nashville, life has been good because of them.

I thank my family members; my loving parents, my sister Razia and my niece Eliza (who was born during my PhD) for being the continuous source of inspiration for years. I also thank my in-laws, Steven and Davena Garcia for their love and support. Last but not least, I thank my beloved wife, Simone Garcia for being in my life. Words simply cannot describe how many sacrifices she has made for me and my career over the years. I am extremely lucky and grateful for her unconditional love and support, and I cannot wait to start the next phase of our life together.

TABLE OF CONTENTS

Page

DEDICATION . . . . **iii**

ACKNOWLEDGMENTS . . . . **iv**

LIST OF TABLES . . . . **viii**

LIST OF FIGURES . . . . **ix**

Chapter

1 Introduction **1**

1.1 Current State of Battling Climate Change 1
1.2 Electrification of Transportation 2
1.3 Li-ion Battery Technologies 3
1.4 Solid-state Batteries: Safer Alternatives 4
1.5 Metal Anodes for Solid-state Batteries 8
1.6 Cathodes for Solid-state Batteries 13
1.7 Solid-state Battery Architectures 15
1.8 Scalable Manufacturing of All Solid-state Batteries 18
1.9 Research Questions and Outlook 31

2 Experimental Methods **33**

2.1 Battery Testing Setups 33
2.2 Electrochemical Measurements 34
2.3 Synchrotron X-ray Nanotomography 40

3 Percolation and Ion Transport in Hybrid Solid Electrolytes for Li-metal Batteries **45**

3.1 Introduction 45
3.2 Materials Synthesis and Processing 47
3.3 Material Characterization 48
3.4 Synchrotron Nanotomography 48
3.5 Measurements of Transport Properties 49
3.6 Continuum Percolation Model 50
3.7 Results and Discussion 52
3.8 Conclusions 60

4 Creep Effect and Interfacial Dynamics in Garnet-based Solid-state Li Metal Batteries . . . 62

4.1 Introduction . . . 62
4.2 Materials Synthesis and Processing . . . 65
4.3 Electrochemical Measurements . . . 66
4.4 Characterization . . . 67
4.5 Computational Modeling . . . 67
4.6 Results and Discussion . . . 69
4.7 Conclusion . . . 88

5 Electrodeposition Dynamics in Solid-state Batteries: From Lithium metal toward Anode-free Approaches . . . 90

5.1 Introduction . . . 90
5.2 Experimental . . . 93
5.3 Results and Discussion . . . 96
5.4 Conclusion . . . 105

6 Summary and Conclusions . . . 106

6.1 Summary . . . 106
6.2 Conclusion . . . 110

Appendix

A Supporting Information: Chapter 3 . . . 112

B Supporting Information: Chapter 4 . . . 116

C Supporting Information: Chapter 5 . . . 125

REFERENCES . . . 126

LIST OF TABLES

Table Page

1.1 Summary of solid electrolytes (Li^+ ion conductor) and their properties . 9

3.1 Activation energy and transference number for hybrid electrolytes 53

LIST OF FIGURES

Figure Page

1.1 (a) Global Greenhouse gas emissions by the (a)economic sector, (b)transportation sector. Growth of electric vehicle sales across (a) region and (d) transport mode. The plots are outsourced from IEA (2021). . . 2

1.2 Schematic diagram showcasing difference in architectures of a (a) conventional Li-ion battery and (b) solid-state Li-metal battery. 4

1.3 (a) Classification of available electrolytes in Li-ion batteries. Different classes of solid electrolytes (Polymer, ceramic and hybrid) are shown. (b) Different material properties of the electrolytes, illustrating the pros and cons of solid electrolytes. 8

1.4 Schematic diagram illustrating different interfacial challenges that exist in a solid-state battery 10

1.5 Causes of Li dendrite growth and failure modes in solid electrolytes. (a) The high electronic conductivity of solid electrolytes initiates internal Li deposition, (b) dendrite propagation and crack formation in electrolytes, (c) uncontrollable Li nucleation at interfacial voids and (d) pressure-induced extrusion of Li metal into the solid electrolyte. 11

1.6 Summary of interfacial phenomena observed within Li metal and solid electrolytes. Investigations were carried out via scanning and transmission electron microscopy. (a) Void formation in Li|SE interface during multiple stripping (Kasemchainan et al. (2019)), *Copyright 2019, Springer Nature*. (b) Morphological changes in Li metal after long-term dissolution (Krauskopf et al. (2019b)), *Copyright 2019, American Chemical Society*. (c) Thick interphase regions between Li and solid electrolyte (Lee et al. (2021a)), *Copyright 2021, American Chemical Society*. (d) Reactivity of Li upon contact with solid electrolyte (Lewis et al. (2019)), *Copyright 2019, American Chemical Society*. (e) Li growth morphology on solid electrolyte upon electrodeposition (Krauskopf et al. (2019c)), *Copyright 2019, Elsevier*. (f) Li precipitation process along surface defects of solid electrolyte (Wang et al. (2021b)), *Copyright 2022, John Wiley and Sons*. 14

1.7 Schematic of (a) battery-driven applications, (b) battery architecture from low to high energy density, corresponding weights of battery components (c) manufacturing processes of ASSBs with respect to scalability and (d) cell type with respect to production cost. *Copyright 2022, Elsevier*. 18

1.8 Prospects of available scaled up technologies and cell formats for solid-state battery manufacturing. Each technology requires three key steps to check: mixing of materials, annealing and thinning/calendering, followed by stacking cell assembly. The figure shows better opportunity for slurry/tape casting manufacturing for solid-electrolytes and cathodes. For metal anode processing, extrusion/pressure-assisted lamination is preferred. *Copyright 2022, Elsevier*. 23

1.9 Role of pressure and temperature in different steps of manufacturing solid-state batteries with solid electrolytes: (a) electrolyte processing (ionic conductivity as a function of processing pressure and temperature), (b) cell manufacturing for good interfacial contact (<10 Ωcm^2), (c) operating range for batteries with oxide, sulfide, argyrodite and halide electrolytes. *Copyright 2022, Elsevier*. 29

2.1 (a) Schematic of the 3-electrode setup for a symmetric cell. Li foil was used as a reference electrode. (b) 3D model of the 3-electrode setup assembly and (c) dimensions of the PEEK chamber. 35
2.2 (a) A representative Nyquist plot for LLZO solid electrolyte with ion-blocking electrode and (b) ion-conducting electrode (Li metal). Corresponding equivalent circuits were also shown. Black circles represent experimental data and red line represents fitted data. 37
2.3 (a) Nyquist plots of a symmetric cell Li|PEO-LLZO|Li showing the change in cell resistance, before and after the DC polarization. (B) Current profile of the symmetric cell showing initial current (I_0) and steady-state current (I_{SS}). 38
2.4 (a) Schematic of the X-ray nanotomography source (APS beamline 32ID). (b) Snapshot of the experimental setup. 42
2.5 Schematic of the sample preparation of hybrid electrolytes. The samples were glued with epoxy on graphite and mounted on the stage. 44

3.1 Schematic of percolation regimes that exist in hybrid electrolytes (a) and ionic conductivity measurements for hybrid electrolytes with varying concentrations of inorganic (LLZO) fillers (b). Ionic conductivity represented as a function of volume fraction to highlight temperature dependent optimum (c). 52
3.2 Hybrid electrolytes are typical solution processed (a) into free standing films of varying thickness (b,c). Optical images demonstrating the surface morphology of a hybrid electrolyte composed of (d) 5 vol%, (e) 15 vol% (f) 50 vol%. (g) A schematic of a how the inorganic microstructure can be extracted using synchrotron nano tomography. (h) A geometric analysis on 3-D reconstructions to determine best volume ($15\times15\times15$ μm^3) for quantitative analysis of reconstructed samples. 55
3.3 (a) Stack of binarized images demonstrate polymer and ceramic region in a hybrid electrolyte. (b) The normalized ceramic area at different cross-sections in hybrid electrolytes containing 5, 15, and 50 vol% Al-LLZO. (c) 10 largest percolated (aggregated) structures in a sub-volume for 5, 15, and 50 vol% Al-LLZO and (d) exploded view of top three aggregated structures in each electrolyte. 57
3.4 Reconstructed images for hybrid solid electrolytes of 5, 10, 15, 25 and 50 vol% loading of LLZO. 59

3.5 (a) Schematic of the difference between theoretical (percolation theory) and experimentally observed percolation of particles. (b) Ionic conductivity of hybrid electrolytes (measured both experimentally and theoretically) and normalized surface area (measured from nano-CT image analysis) of hybrid electrolytes. 60

4.1 In a 3-electrode setup, (a) Nyquist plots showing the interfacial resistance of the working electrode (stripping) for four different symmetric cells. (b) Stripping profiles of the symmetric cells and (c) change in interfacial resistances due to Li creep. (d) Contact area (Li coverage on LLZO) evolution due to Li creep after stripping. (e) Schematic of void formation and creep-induced recovery of Li|LLZO interface. 72
4.2 In 3-electrode system, (a,c) voltage profiles of the working electrode at current density of 0.3 and 0.5 mA/cm^2. (b,d) Corresponding change in interfacial resistances over time due to Li creep after stripping. 74
4.3 In a 3 electrode setup, step-wise stripping test (1 mAh/cm^2 per step) at 0.8 mA/cm^2, followed by resting for 2 hours. (a) Voltage profiles of Li stripping at 5, 10, and 15 MPa stack pressure and (b) creep-induced change in interfacial resistances during the resting period. EIS plots showing improvement of interfacial resistance due to Li creep during the resting period at (c) 5 MPa, (d) 10 MPa, and (e) 15 MPa. 77
4.4 (a) Stripping and plating profiles of a symmetric cell in the 3-electrode setup, showing the plating induced shorting at 0.8 mA/cm^2. The stripping side has a negligible impact on cell shorting. (b) Plating profiles of a symmetric cell at 0.3, 0.5 and 0.8 mA/cm^2. (c) Schematic of Li plating mechanism at low and high current density, displaying the effects of irregular and isolated Li deposition on LLZO. 79
4.5 (a) Comparison of critical current density (CCD) of LLZO at 20°C, with and without creep protocol. (b) CCD of LLZO at 60°C. (c) Comparison of room-temperature (20-25°C) critical current densities reported for Li metal and LLZO. "Bare LLZO" represents the CCD of Li|LLZO without any interlayer or surface alterations Sharafi et al. (2016); Wang et al. (2019b); Chang et al. (2021); Yang et al. (2021a); Cheng et al. (2015). "Interlayer/Alloy" represents the CCD where a thin interlayer or alloying mechanism was used to increase the wettability Dussart et al. (2021); Ma & Xu (2022); Huang et al. (2018); Su et al. (2019); Lu et al. (2018); Chen et al. (2022); Mu et al. (2022). "Surface modification" represents the CCD where surface structure of LLZO was modified by patterning Xu et al. (2021c); Fu et al. (2020). 81

4.6 (a) Nyquist plots of a Li|LLZO|LFP full cell displaying interfacial evolution during the first charge and discharge. The yellow, pink, grey, and blue semicircles represent the resistance of bulk, grain boundary, and anodic and cathodic interface. (b) Schematic of interfacial change during full cell cycling, (c) Change in interfacial resistance of LFP|LLZO and Li|LLZO during first charge and discharge. Stack pressure dependent cycling performance of a Li|LLZO|LFP full cell at 5, 10 and 15 MPa at (d) 0.2C, 20°C and (e) 0.4C, 60°C. The areal capacity of the cathode was 2.2-2.3 mAh/cm^2. 83
4.7 (a) Cell resistance evolution of Li |LLZO|LFP full cells with the thicker cathode (4.6 mAh/cm^2 areal capacity) after cycling at 0.2C and 0.4C. (b) Galvanostatic charge/discharge profiles at high current density showing cell failure at 0.4C at the 13th cycle and subsequent recovery after slow discharging (0.1C). (c) Cycling performance of the cell at 0.2C and 0.4C. The operating temperature was 20°C and stack pressure was 10 MPa. (d) Schematic of the cell cycling, failure, and recovery demonstrating the reversible shorting behavior in full cells. 86

5.1 Schematic of the pressure cell setup for operando stress monitoring. . . . 95
5.2 Stress response of a symmetric cell during critical current density measurement at (a) 20°C and (b) 65°C. Differential pressure (dp/dt) response of the corresponding cycles at (c) 20°C and (d) 65°C. 96
5.3 Stress response of a Li stripping test at 0.3, 0.5, 0.8 and 1 mA/cm^2. Pressure differential *(dp/dt)* was calculated for stripping at each current density. 98
5.4 (a) Galvanostatic charge-discharge profile of a Li|LLZO|LFP full cell at 0.2C and 60°C. Stress and capacity-derivative differential pressure response of the corresponding cycles are shown below. (b) C-rate dependence of the full cell cycling at 60°C. At 2C, cell shorting was observed which was also monitored from the sudden pressure drop. 100
5.5 (a) Room temperature Li plating profile on a graphite foil in a Li|LLZO|Gr half-cell configuration. Around 3.5 mAh/cm^2 (18 μm thick) Li was plated. (b) Nyquist plot showing the impedance drop after plating, signifies the surface coverage of Li on a 4 mm graphite foil. (c) Stripping-plating profile of the half cell at 3 different stack pressures (5, 10 and 15 MPa). 1 mAh/cm^2 of Li was stripped and plated in each cycle. (d) Plating profile of the half cell at 60°C. (e) Nyquist plot signifying the growth of Li coverage over time. (f) Extended stripping and plating (1 mAh/cm^2) for over 60 hours, showing gradual decrease of Li loss. 102

1.1 (a) XRD and (b) TGA of PEO-LLZO electrolytes at different loading . . . 112
1.2 (a) Reconstructed images at 5, 10 and 15 μm sub-volume and (b) normalized area of 10 largest clusters 112
1.3 (a) SEM image of Al-LLZO powder and (b) LLZO particle size distribution from dynamic light scattering (DLS) 113

2.1 Schematic of the solid-state cell types used in this work, (a) symmetric cell, (b) 3-electrode symmetric cell with Li foil as reference electrode and (c) full cell with composite cathode (LFP). 116
2.2 SEM images of LLZo showing of (a) rough surface LLZO and (b) smooth surface. (c) SEM image of a FIB section of LLZO, showing microstructural pores. 116
2.3 (a) Nyquist plots showing stack pressure dependence on interfacial resistance of Li-LLZO. (b) Zoomed in plot of (a) highlighting the change in bulk resistance, indicating Li electrode area expansion. (c) EIS spectra fitting and (d) change in interfacial resistance with respect to pressure. . . 117
2.4 Nyquist plot showing negligible ($\approx 0\Omega.cm^2$) of interfacial resistance after heat-treatment at 220°C. 117
2.5 Stack pressure and subsequent time-dependent creep (pure) effect on a Li|LLZO interface at 5, 10 and 15 MPa. Li was attached on LLZO pellet and no electrochemistry was conducted. Simulation was carried out on model LLZO surface. 118
2.6 In a 2-electrode setup, stripping and plating profile of a Li|LLZO|Li symmetric cell at 5,10 and 15 MPa at (a) 20°C, (b) 35°C and (c) 50°C. During post-strip hold, change in interfacial resistance due to Li creep at (d) 20°C, (e) 35°C and (f) 50°C. 119
2.7 Critical 'stripping' current density measurement of Li|LLZO|Li symmetric cell at room temperature. This demonstrates that Li can be stripped at a substantial higher current density than the typical current density limit of LLZO. It should be noted that at the end of each stripping/plating period, a resting period of 15 minutes was introduced in the measurement protocol to allow Li creep. 119
2.8 Snapshot of stripped and plated LLZO. 120
2.9 Charge/discharge curves of Li|LLZO|LFP full cells at 20°C and 0.2C under (a) 5 MPa, (b) 10 MPa and (c) 15 MPa of stack pressure. 120
2.10 EIS fitting of a full cell. Deconvolution of the spectra shows resistance from bulk, grain boundary, anodic interface and cathodic interface. 121
2.11 Room temperature Nyquist plot of a symmetric and full cell, (b) corresponding Bode plots and (c) DRT curves. 121
2.12 Nyquist plots of a full cell showing interfacial impedance evolution during charging and discharging (C-rate 0.4) at 60°C. 122
2.13 X-ray diffraction results of cubic LLZO powder, LLZO pellet and LLZO pellet (shorted). 122
2.14 (a) Cyclic voltammetry (CV) comparison of LFP|LLZO|Li full cells at 20°C and 60°C. (b) CV plot of full cells over multiple cycles at 60°C. . . . 123
2.15 3D surface mapping of polished LLZO surface. 123
2.16 Contact map of Li-LLZO interface after applying stack pressure of (a) 5 MPa, (b) 10 MPa and (C) 15 MPa. Corresponding contact maps of the same interfaces after pure creep of Li at (c) 5 MPa, (d) 10 MPa and (e) 15 MPa. Yellow represents contact regions and blue represents non-contact regions in the plots. 124

3.1 Stress evolution and differential pressure (dP/dQ) profile of a Li|LLZO|LFP full cell cycling at 20°C. 125
3.2 Stress evolution of a full cell at 0.1C and 0.2C (20°C). 125

Chapter 1

Introduction

1.1 Current State of Battling Climate Change

The energy demand over the last few decades experienced a massive surge due to the rapid growth of the population and technological advances. Despite posing severe environmental threats, fossil fuels remain the main contributor to meeting the increasing energy demand. As a result, Greenhouse gases (GHG) are frequently emitted in large quantities during the combustion process of fossil fuels. Greenhouse gases (GHGs) include 82% carbon dioxide (CO_2), 10% methane (CH_4), 5% nitrous oxide (N_2O) and 3% fluorinated gases (Administration (2022); Lamb et al. (2021); Brand & Boardman (2008)).This is expected to further increase over time due to the rapid industrial growth. As a result, we are currently observing the severest period of climate change. This has caused an increase in global temperatures (1.1°C from 1901 to 2020) and sea-level rise (3.2 mm/year from 1993 to 2020) (Asif & Muneer (2007); Combustion (2015)). Climate change also refers to changes in weather patterns like drought and flooding, causing immense harm to the ecosystems (Zhang & Fujimori (2020); Olabi & Abdelkareem (2022)).Therefore, the current status of climate change poses an existential threat to civilization. Almost all countries have recently started to implement several strategies to adopt green energy policies so that the prolonged effect of climate change can be avoided. In 2015, the Paris Agreement sets out a global framework to limit the global temperature to well below 2°C and pursuing efforts to further decrease it to 1.5°C. It also aims to strengthen every country's ability to deal with the impacts of climate change and support them in their efforts (Schleussner et al. (2016); Delbeke et al. (2019)). Therefore, a massive infrastructural change is required from the technological aspects to socioeconomic policy-making (Bolsen et al. (2014); Åhman et al. (2017)). The most eminent challenges to adopting these pathways are to overcome the technological and commercial barriers to decarbonization and energy sectors (Schiffer & Manthiram (2017)).

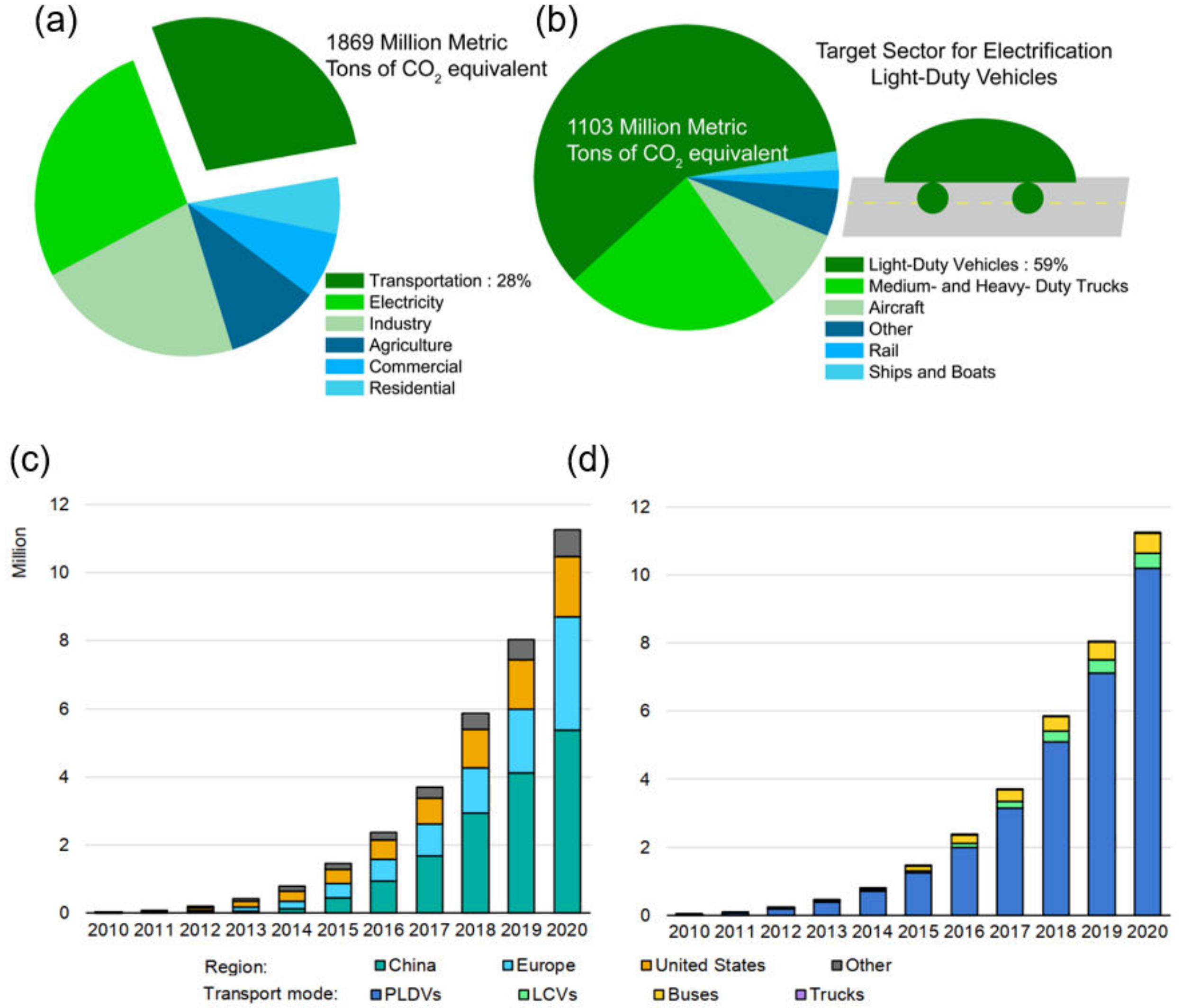

Figure 1.1: (a) Global Greenhouse gas emissions by the (a)economic sector, (b)transportation sector. Growth of electric vehicle sales across (a) region and (d) transport mode. The plots are outsourced from IEA (2021).

1.2 Electrification of Transportation

Recent reports have shown that almost 60% of the energy produced in the United States in 2022 is in the form of fossil fuels and the low efficacy of renewable sources continues to impede the growth of this sector (Energy Information Administration (EIA) (2013)). Because of the intermittency of renewable energy sources like wind, solar, and tidal; there exists a vital need for reliable forms of energy storage. Electric power (39%) and transportation (27%) are the largest emitters of CO_2 in the US **(Figure 1.1a)** (IEA (2021)). The transportation sector consists of passenger cars, light-duty trucks, medium and heavy-duty trucks, and aircraft; amongst which passenger vehicles consume the most energy **(Figure 1.1b)**. CO_2 emissions closely follow energy use because the primary source of energy is petroleum-based. Thus, electrifying transportation by enabling new technologies such as electric vehicles (EVs) including battery electric vehicles (BEVs) and plugin hybrid electric vehicles (PHEVs) is a strategy to substantially reduce CO_2 emissions. In recent years, the transportation sector has witnessed remarkable progress in the area of vehicle electrification, however, widespread adoption of electric vehicles remains severely limited **(Figure 1.1c,d)**. One of the biggest challenges impeding the growth of electric vehicles is the performance limitation of conventional battery technologies. While Li-ion batteries are currently the industry standard for electric and hybrid electric vehicles, the limited specific energy density and high production cost are becoming major roadblocks to the widespread electrification of the transportation sector (Sripad & Viswanathan (2017)). Compared to fossil fuels, the energy densities of current batteries are extremely low, which requires significantly higher volumes of batteries to provide comparable driving ranges. In addition, a longer time is generally needed to fully recharge the car batteries. The safety of the battery pack in EVs also plays an important role, as this often leads to fire hazards and explosions. Finally, the cost of current battery technologies is still too high ($ 132/KWh), which is exacerbated by the shorter battery lifetimes (Nykvist & Nilsson (2015); BloombergNEF (2021)). Therefore, many challenges remain toward the rapid electrification of the transportation sector.

1.3 Li-ion Battery Technologies

Portable electronics and electric vehicles greatly benefit from advanced energy storage technologies. Li-ion batteries (LIBs) are state-of-the-art energy storage systems for these applications. LIBs typically contain a graphite anode, an intercalation cathode, a separator, and two current collectors. Upon assembly, These are flooded with a liquid electrolyte (Wang et al. (2021d)). The electrodes serve as a charge storage media and the electrolyte facilitates ion transport from the cathode to the anode. The chemical potential of graphite is 0.2V (vs SHE), which has a theoretical capacity of 372 mAh/g. Li metal (-3.4V vs SHE) is an excellent alternative for graphite which has a higher theoretical capacity (3860 mAh/g) and low density (0.59 gm/cm^3). Thus, moving toward Li metal anodes could lead to an increase in energy density for Li-ion batteries (Armand (1983a)). However, there are several challenges associated with lithium metal. First, lithium tends to chemically react with most electrolytes which result in material decomposition and faster cell failure (short lifetime). Secondly, lithium metal undergoes large volume expansions and can form dendrites during cycling which leads to short-circuiting events (Janek & Zeier (2016a); Albertus et al. (2021)).

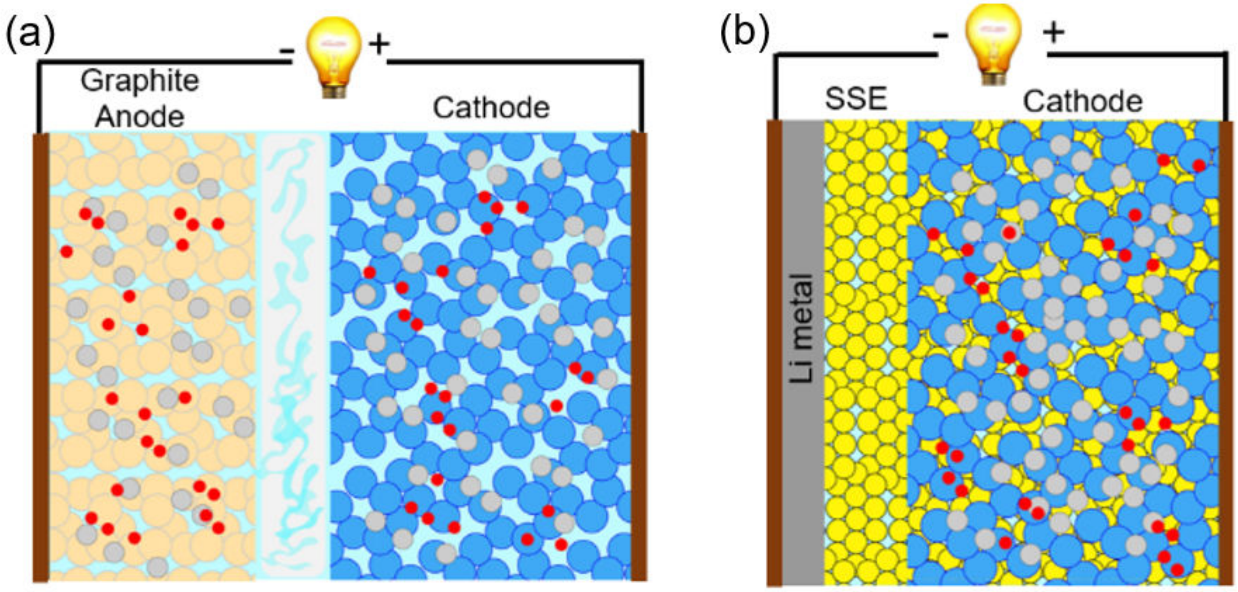

Figure 1.2: Schematic diagram showcasing difference in architectures of a (a) conventional Li-ion battery and (b) solid-state Li-metal battery.

1.4 Solid-state Batteries: Safer Alternatives

The limited energy density of conventional Li-ion batteries restricts their implications in large-scale energy storage systems. The liquid electrolyte in Li-ion battery is comprised of a salt ($LiPF_6$ or LiTFSi) dissolved in organic solvents (e.g.; ethylene carbonate, dimethyl carbonate, propylene carbonate, etc.) **(Figure 1.2a)**. These electrolytes are highly flammable and can lead to a thermal runaway of batteries. Recently, there has been a renewed interest in all-solid-state batteries to address and resolve these safety concerns. Solid-state batteries are safer alternatives due to the non-flammability of solid electrolytes. Here, ions move through a solid ion-conductor which acts as both separator and electrolyte. The unwanted chemical reactions between electrodes and liquid electrolytes can be highly circumvented in solid-state batteries **(Figure 1.2b)**. Due to their excellent mechanical and thermal stability, solid-state batteries hold great promise to enable Lithium metal as the anode (Famprikis et al. (2020); Schwietert et al. (2020)). In addition, solid electrolytes have wider electrochemical windows. Hence, high voltage cathodes such as $LiNiMnCoO_2$ (NMC) and $LiNiCoAlO_2$ (NCA) can be employed in solid-state batteries to increase battery pack energy densities (Muy et al. (2019); Zhu et al. (2021)). Coupling Li metal and advanced cathodes with solid-state electrolyte can thus potentially meet the gravimetric (500 Wh/kg) and volumetric (800 Wh/L) energy density requirements for future EV applications (Zaman & Hatzell (2022); Ding et al. (2019)).

1.4.1 Solid Electrolytes

Fast ion transport through crystalline solids has been recognized for the development of all-solid-state electrochemical systems such as batteries and fuel cells (Keplinger et al. (2013); Al & Po (2018); Kendrick et al. (2007)). Currently, there is a wide range of solid ion conductors available due to an increased interest in solid-state battery applications (Dawson et al. (2019); Li et al. (2019b)). Several families of these solid electrolytes exhibit super ion-conducting properties which even, exceed the conductivity of liquid electrolytes (Kato et al. (2016a); Hu et al. (2018)). However, the chemical and mechanical properties of these solid electrolytes dictate their compatibility with battery electrodes which often possess several limitations on a cell level.

1.4.1.1 High Ionic Conductivity

One of the major limiting factors of early-developed solid electrolytes is their inability to match with the ionic conductivity (>1 mS/cm) of liquid electrolytes (Bruce & West (1982)). In general, higher ionic conductivity is necessary to reduce the ohmic losses in batteries. Room-temperature ionic conductivity of solid electrolytes varies from 10^{-7}-10^{-2} S/cm (Zhang et al. (2018a)). In addition, most inorganic solid electrolytes exhibit a high transference number of ≈1 which indicates a higher cation selectivity. However, inorganic solids are generally polycrystalline materials, and ion transport through the electrolytes is often limited by the presence of numerous grain boundaries (Dawson et al. (2018); Zhou et al. (2020). This severely affects the overall ionic conductivity which has been mostly observed in garnet, perovskite, and phosphate families of solid electrolytes (Meesala et al. (2017)). Such features are usually absent in amorphous sulfide electrolytes such as Li_3PS_4, Li_6PS_5Cl and $Li_{10}GePS_{12}$. The latter offers the highest ionic conductivity (10^{-2} S/cm) than any other solid electrolytes (Kato et al. (2016b); Choi et al. (2018)). On the other hand, organic solid electrolytes are polymer or soft crystal based and exhibit very low room-temperature ionic conductivity (10^{-5} S/cm) and therefore, require high temperature based operations (Armand (1983b); Jin et al. (2014); Wang et al. (2021e)).

1.4.1.2 Low Electronic Conductivity

Most solid electrolytes generally exhibit a comparably lower but noteworthy electronic conductivity (<10^{-8} S/cm) (Han et al. (2019); Liu et al. (2021)). As a result, solid electrolytes often experience internal short-circuiting during battery cycling (Ping et al. (2020)). The local electronic structure of solid electrolytes significantly varies with higher electronic conductivity which leads to internal Li reduction and metallic filament formation within grain boundaries. These self-discharging phenomena are further exacerbated at high-rate cycling and are responsible for dendrite-induced failure (Tewari & Mukherjee (2020). Hence, achieving zero/negligible electronic conductivity is a major concern for solid electrolyte development.

1.4.1.3 High Chemical and Electrochemical Stability

Electrochemical stability against high voltage cathodes and Li metal is critical for developing high-performance solid-state batteries. A solid electrolyte with high chemical and thermodynamic stability not only prevents unwanted SEI layer formation but also facilitates efficient ion transport. Experimental evidence suggests that only a few solid electrolytes are stable against alkali metal anodes, while others either form interfacial byproducts or experience chemical decomposition (Schwöbel et al. (2015); Garcia-Mendez et al. (2020); Connell et al. (2020); Lewis et al. (2019)). Similar phenomena were also observed for cathode compatibility (Park et al. (2016); Delluva et al. (2020)).

1.4.1.4 High Thermal and Mechanical Stability

The ionic conductivity of solid electrolytes significantly increases at elevated temperatures. Therefore, a thermally stable solid electrolyte can enable better cyclability at high temperatures without causing thermal runaways (Chen et al. (2020b)). In addition, solid electrolytes should have higher mechanical stiffness to inhibit any dendrite growth of Li. Inorganic solid electrolytes generally exhibit significantly higher shear modulus (>8 GPa) than polymer electrolytes (<0.1 GPa) (Hikima et al. (2022); Yu et al. (2016); Wang et al. (2020b)). However, polymer electrolytes hold several advantages over brittle inorganic electrolytes due to their flexibility.

1.4.1.5 Comparison of Solid Electrolytes

There are significant challenges associated with developing standard electrolytes for high-performance batteries. The inorganic electrolytes can further be classified as glassy, amorphous, or crystalline solids **(Figure 1.3a)**. A side-by-side comparison of different solid electrolytes is shown to reveal their properties **(Figure 1.3b)**. Both garnets and sulfides are rigid ceramics that are restricted to mechanical flexibility. Due to their soft nature, polymer electrolytes are adaptable to large volume changes in electrode materials (e.g.; Li metal) but suffer from low room-temperature ionic conductivity (Park et al. (2006)). Hence, a hybrid (polymer-ceramic) electrolyte is considered a suitable approach for cell-level implications of solid-state batteries (Yu & Manthiram (2020)).

1.5 Metal Anodes for Solid-state Batteries

Alkali metal anodes (e.g.; Li) have the highest specific capacities and hence, offer huge opportunities for next-generation rechargeable batteries (Zheng et al. (2016a)). Unlike Graphite or Silicon, alkali metals are hostless anodes with low reduction potentials (Chen et al. (2020a)).Among those, Li metal exhibits the lowest reduction potential (-3.04 V vs SHE) and hence, is the most desirable anode for Li-ion batteries. A major advantage of solid electrolytes is to safely enable Li metal. However, Li metal undergoes significant volume change during electrochemical cycling which can lead to catastrophic cell failure due to irreversible dendrite formation (Dixit et al. (2020c); Krauskopf et al. (2020b); Chen

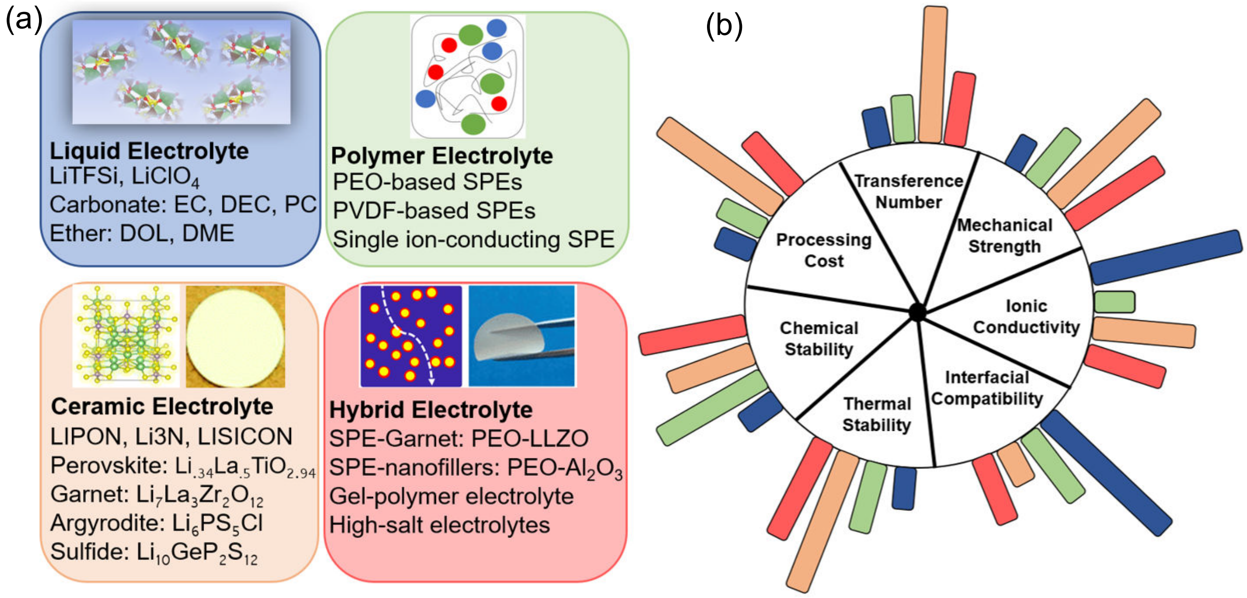

Figure 1.3: (a) Classification of available electrolytes in Li-ion batteries. Different classes of solid electrolytes (Polymer, ceramic and hybrid) are shown. (b) Different material properties of the electrolytes, illustrating the pros and cons of solid electrolytes.

Table 1.1: Summary of solid electrolytes (Li^+ ion conductor) and their properties

Type	Composition	Ionic Conductivity (RT) **(S/cm)**	Voltage Window **(V)**	Stability
Garnet	$Li_7La_3Zr_2O12$	10^{-5}-10^{-3}	0-6	Li metal
Perovskite	$LiLaTiO_3$	10^{-6}-10^{-4}	0-2	Unstable
Phosphate	Li_3PO_4	10^{-6}-10^{-5}	0-5.5	Li metal
Sulfide	Li_7PS_4	10^{-4}-10^{-3}	0-3	Unstable
	$Li_{10}GeP_2S_{12}$	10^{-3}-10^{-2}	0-3	Unstable
Argyrodite	Li_6PS_5Cl	10^{-3}	0-6	Unstable
Halide	Li_5YZrCl_6	10^{-3}-10^{-2}	0-5	Unstable
Polymer	PEO	10^{-7}-10^{-5}	0-4	Stable
	PAN	10^{-7}-10^{-5}	0-4	Stable
	PVDF	10^{-7}-10^{-6}	0-4	Stable

et al. (2020c); Yan et al. (2019)). The morphology and structure of lithium dendrites can take a variety of different forms. Prior work on lithium dendrite formation in polymer solid electrolytes has shown that needle-like dendritic features can form at low current densities where concentration gradients at solid | solid interfaces are minimized (Maslyn et al. (2018)). These structures can grow across the electrolyte and short the cell. In contrast, at high current densities, concentration gradients at solid|solid interfaces can lead to the formation of moss-like lithium deposits (Krauskopf et al. (2019c); Porz et al. (2017); LePage et al. (2019)). Theoretical studies have suggested that charge compensation has to occur because of a concentration depletion effect at the negative electrode. This instability can drive dendrite formation (Hatzell et al. (2020); Taylor et al. (2018)). The dynamics of lithium vacancies at the solid electrolyte interface can also affect stable lithium cycling.

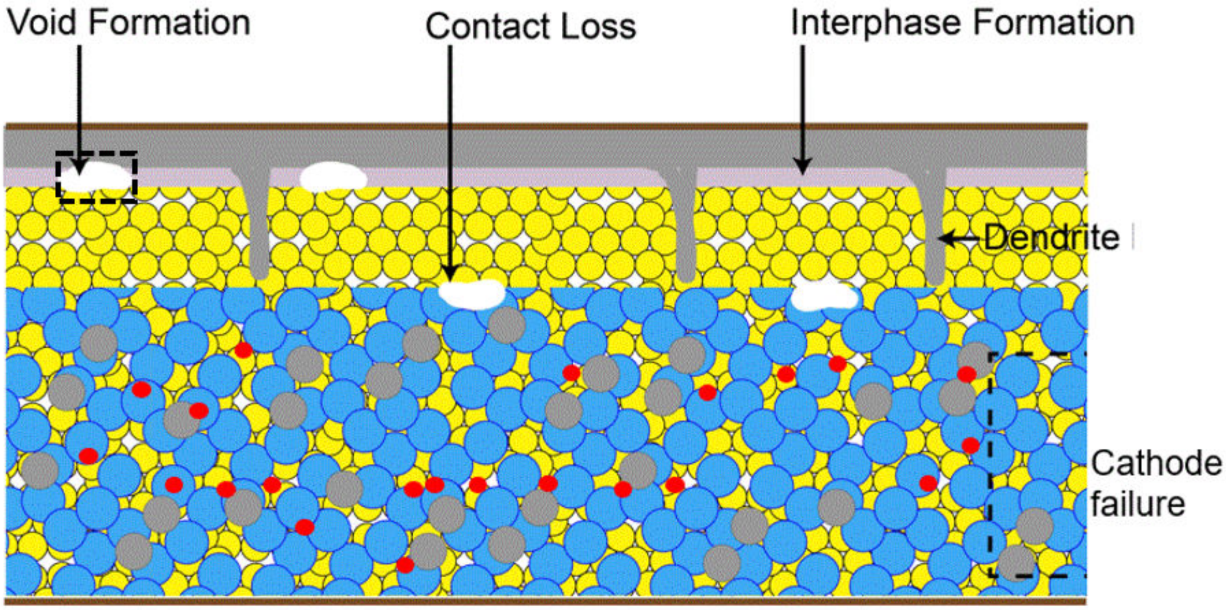

Figure 1.4: Schematic diagram illustrating different interfacial challenges that exist in a solid-state battery

Large voids are generated (driven by vacancy accumulation) at the interface which is found to precede the dendritic growth of Li. Therefore, it is a major challenge to find compatible electrolytes that are thermodynamically and kinetically stable against Li metal. In addition, the accumulation of passivated ("dead") Li over multiple cycles can drastically decrease the coulombic efficiency of Li-metal cells (Chen et al. (2020b)).

1.5.1 Electro-chemo-mechanics of Li metal and Solid Electrolytes

The prospect of Li metal as an anode requires an extensive understanding of its physicochemical and electrochemical properties. Li metal has a low density (0.534 g/cm^3) and a molar volume of 13 cm^3/mol at room temperature. As it exhibits a strong reactivity with adjoining materials, the stability of Li metal in contact with a solid electrolyte is imperative for designing functional batteries. An ideal solid electrolyte should impede the chemical and electric potential-driven reactions at the interface where the electron can transfer from Li to the solid electrolyte. Thermodynamic stability is ensured when the conduction band minimum (CBM) of solid electrolyte lies above the Fermi level of Li metal. The kinetic stability of solid electrolytes is also important as this largely dictates the interfacial charge transfer resistance R_{CT} evolution upon contact with Li metal. The kinetics of interphase formation depends on the type of solid electrolytes. For example, superionic conductors like sulfides (Li_3PS_4, $Li_{10}GeP_2S_{12}$) and phosphates (LAGP) form several decomposition products at the interface by contacting with Li metal (Wenzel et al. (2015b)). These can be considered as regions of mixed conducting interphase (MCI) regions. This is different than the formation of a kinetically self-limiting but ion-conducting metastable SEI layer which is observed in the case of liquid electrolytes. Lithium flux across these interphase layers j_{Li} can be calculated by:

$$j_{Li} = \frac{\sigma_e . \sigma_{Li}^{+}}{F^2(\sigma_e + \sigma_{Li}^{+})} \frac{\mu_{Li}^{0}}{l_{SEI}} \tag{1.1}$$

Here σ_e and σ_{Li} represent electronic and ionic conductivity of the electrolyte, respectively. Local chemical potential, μ_{Li}^{0} is normalized by the thickness of SEI layer, l_{SEI} (Wenzel et al. (2018)).

The effects of such reactive SEI layers in solid-state batteries are highly detrimental. The transient growth of SEI layers dramatically reduces the capacity and cyclability. In addi-

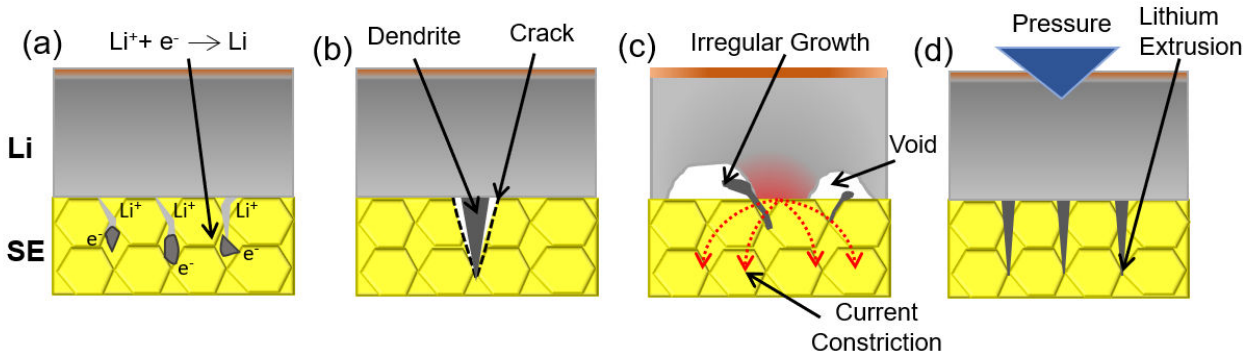

Figure 1.5: Causes of Li dendrite growth and failure modes in solid electrolytes. (a) The high electronic conductivity of solid electrolytes initiates internal Li deposition, (b) dendrite propagation and crack formation in electrolytes, (c) uncontrollable Li nucleation at interfacial voids and (d) pressure-induced extrusion of Li metal into the solid electrolyte.

tion, insufficient contact points between Li and SE significantly distort the electric current lines closer to the contact points and increase the constriction resistance ($R_{contact}$) (Fleig et al. (1998)). In a battery system, the combination of such phenomena causes high overpotential and cell resistance which results in low power density, reduced active material utilization, and low energy efficiency. Electrochemically, the rate-determining process in a Li-SE interface can be complicated to identify. Generally, Electrochemical Impedance Spectroscopy (EIS) is widely used to determine the overall interfacial resistance R_{int}. To evaluate the interfaces in solid-state battery, this can be written as:

$$R_{int} = R_{ct} + R_{scl} + R_{contact} \tag{1.2}$$

Here R_{scl} is the space-charge layer resistance which is negligible small and does not contribute at cell resistance (De Klerk & Wagemaker (2018)). The charge-transfer resistance depends on the exchange current density, i_0:

$$R_{ct} = \frac{RT}{Fi_0} \tag{1.3}$$

Here R is the cell resistance and F is Faraday constant.

Experimental studies on pristine Li|SE interfaces estimated the value of $R_{ct} < 0.1\ \Omega.\mathrm{cm}^2$ (Krauskopf et al. (2019c)). Hence, the interfacial transport limitation in solid electrolytes can be mostly attributed to the contact resistance $R_{contact}$. This is commonly referred to as interfacial resistance in literature. The lack of active contact points between Li and SE is responsible for forming constriction zones that impede the ion migration process, and increase the local electric field and overall electrode polarization (Kasemchainan et al. (2019)). The constriction zones possess a substantially higher local current density (10-100x of applied current density) which act as primary hotspots for dendrite nucleation (Dixit et al. (2020c)). Therefore, the maximization of the contact area between Li and SE is highly preferred during electrochemical cycling to eliminate current constriction. However, the goal to achieve negligible contact resistance (<1 Ωcm^2) is frequently hindered by severe surface contamination, high density of defects, and low interfacial wettability. For example, garnet oxide solid electrolytes (e.g.; LLZO) react with atmospheric CO_2 and generate thin carbonate (Li_2CO_3) layer on the surface which is lithiophobic (Sharafi et al. (2016)). Similar phenomena were observed for sulfide electrolytes (e.g.; Li_6PS_6Cl) where a high stack pressure (>15 MPa) is required to achieve conformal contact (Lewis et al. (2021)). During electrochemical cycling, morphological changes in the lithium metal take place due to the strong volume change combined with the low plasticity of the solid electrolyte and limited lithium vacancy diffusion. Due to its large contribution to both vacancy annihilation and diffusion, the microstructure and non-equilibrium defects of lithium metal play a large role in the dissolution kinetics. At low current density, Li adatom transfer to fill a Li vacancy at the surface is largely governed by self-diffusion and plastic flow of Li metal. This mechanism is greatly affected when the current density is higher.

1.6 Cathodes for Solid-state Batteries

Solid-state batteries can potentially employ all the widely used cathode materials. However, the charge transport and reaction mechanisms of cathode-solid electrolyte interfaces are yet to be explored. The intrinsic electronic conductivity of the cathode and anode electrodes are different. For example, metallic Li anode has high electronic conductivity, whereas, cathodes are semiconductor-type materials. Most often, cathodes are mixed with ionically (Li salt/solid electrolyte) and electronically conductive (conducting carbon) materials to improve their electrochemical performance. Due to the complex structure of the composite, charge transport is often hindered due to a more tortuous path. In general, the mostly used cathodes for solid-state battery research are $LiFePO_4$ (LFP), $LiCoO_2$ (LCO), $LiNiMnCoO_2$ (NMC) and $LiNiMnO_2$ (LNMO) (Wang et al. (2021a); Kim et al. (2020); Asano et al. (2018); Delluva et al. (2020); Sastre et al. (2019)). The chemical and electrochemical stability of cathodes in solid-state batteries has drawn significant interest. In conventional batteries, the pores in composite cathodes are filled with liquid electrolytes which facilitates ion transport. In solid-state cathodes, these pores act as ion-blocking regimes. During electrochemical cycling, shrinkage/expansion of active materials due to lithiation/delithiation gradually can increase the intra-particle stress and frequently initiate cracks within composite cathodes. Such mechanical failure drastically affects the cell performance, which is often seen by faster capacity decay (Ohno et al.

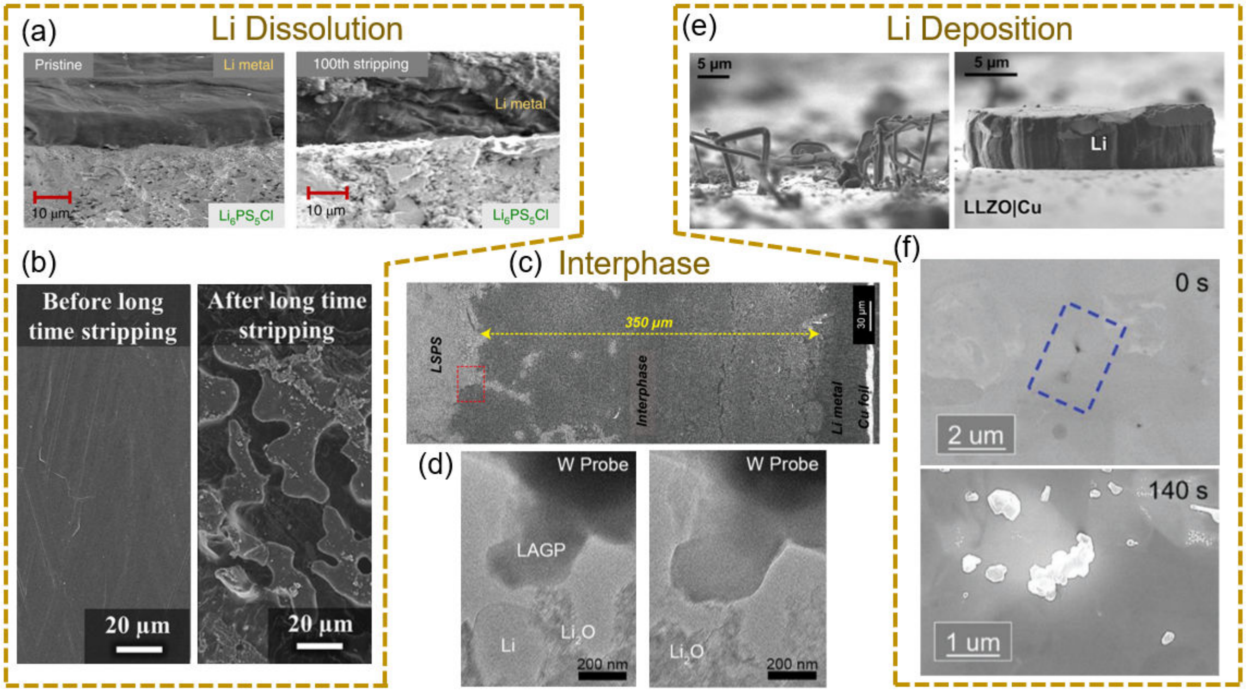

Figure 1.6: Summary of interfacial phenomena observed within Li metal and solid electrolytes. Investigations were carried out via scanning and transmission electron microscopy. (a) Void formation in Li|SE interface during multiple stripping (Kasemchainan et al. (2019)), *Copyright 2019, Springer Nature*. (b) Morphological changes in Li metal after long-term dissolution (Krauskopf et al. (2019b)), *Copyright 2019, American Chemical Society*. (c) Thick interphase regions between Li and solid electrolyte (Lee et al. (2021a)), *Copyright 2021, American Chemical Society*. (d) Reactivity of Li upon contact with solid electrolyte (Lewis et al. (2019)), *Copyright 2019, American Chemical Society*. (e) Li growth morphology on solid electrolyte upon electrodeposition (Krauskopf et al. (2019c)), *Copyright 2019, Elsevier*. (f) Li precipitation process along surface defects of solid electrolyte (Wang et al. (2021b)), *Copyright 2022, John Wiley and Sons*.

(2020); Yu et al. (2019); Zhao et al. (2017)). The rate capability of a solid-state battery strongly depends on the balance of the electronic and the ionic paths within the composite cathode, thus chemo-mechanical stability of the composite microstructure is of high importance (Shen et al. (2019a); Shi et al. (2020b)).

1.7 Solid-state Battery Architectures

Although the current discovery and development of novel solid electrolytes holds great promises to replace the state-of-the-art liquid electrolytes, their integration into high-performance and large-format battery packs are yet to be established. The challenges are primarily associated to the different types of interfaces that exist in a solid-state battery. The chemo-mechanical behavior of a solid|solid interface differs a lot from its solid|liquid counterpart. As a result, a typical solid-state battery suffers from high interfacial resistances which stem from poor contact points within cathode|electrolyte, cathode|binder, cathode|conducting particle, anode|electrolyte interfaces (Banerjee et al. (2020)). An interfacial resistance can also exist within a solid electrolyte due to grain boundaries and dissimilar constituents (for hybrid electrolytes). In addition, interphase also can spontaneously form due to the mismatch of the chemical potential of the interfaces (Chen et al. (2016)). In aqueous batteries, these interphases often form passivation layers at the anode and cathode. However, a negative impact is usually observed in case of solid-state batteries. The combined effect of interface and interphase lead to non-optimal material utilization and poor ion transport in a battery. Electrochemical cycling of the battery can further worsen the interfaces which is reflected by poor cycling performance and catastrophic cell failures (shorting). Resolving chemo-mechanical degradation within the interfaces is one the major challenges for developing high-performance solid-state batteries (Chen et al. (2016); Xu et al. (2021a)). Overcoming degradation processes at buried solid interfaces is necessary for realization of high rate, high capacity solid state batteries (350 Wh.kg^{-1}). This requires engineering architectures that can adequately address chemo-mechanical phenomena (dendrites, physical voids, chemically unstable interfaces, sluggish transport kinetics) and manufacturing challenges (Albertus et al. (2018); Balaish et al. (2021); Schnell et al. (2020)). Stress gradients can occur during materials assembly and operations which impact degradation modes (Bartsch et al. (2018)). In addition, potential gradients can also arise at interfacial inhomogeneities and drive dendrite formation and subsequent failure (Krauskopf et al. (2019c); Kasemchainan et al. (2019); Mistry & Mukherjee (2020)). Chemo-mechanical degradation and material transformations are also exacerbated in solid state batteries because of dense electrodes and electrolytes with high stiffness. This can lead to material fracture during dynamic operating conditions that require volume expansion Dixit et al. (2020c). Composite solid state cathodes experience repeated expansion/contraction which contribute to loss of interfacial contact and cracking during cycling (Shi et al. (2020b)). It is desirable to have composite cathodes with high densities and limited voids to ensure efficient ion transport (Hlushkou et al. (2018)). Novel solid-state battery architectures are needed to address stress and potential gradients that arise due to chemo-mechanical dynamics within a solid state battery (Kim et al. (2021); Delluva et al. (2020)).

Cold-pressed powder processing produces thin film pellets (0.5-2 mm diameter) and is widely used with research and development laboratories **(Fig.1.7b-i)** (Krauskopf et al. (2019c); Sharafi et al. (2016); Culver et al. (2019). Pellet-based solid electrolytes typically operate under pressure which leads to further densification Doux et al. (2020a). Full cells can be assembled via manually stacking the anode, solid electrolyte and cathode on top of each other **(Fig.1.7c-ii)**. Stack pressure can impact full cell performance and has been shown to be an effective strategy for preventing unwanted void formation and delamination at the anode (Doux et al. (2020b); Wang et al. (2020a)). This approach is widely utilized in research laboratories but is unlikely to scale for industrial production due to electrolyte thickness and low energy density (Oh et al. (2017); Kim et al. (2021)). Composite cathodes account for less than 7% of total cell weight in pellet-based architectures **(Fig.1.7b-i)**. To achieve target gravimetric energy densities requires decreasing the solid electrolyte by an order of magnitude (<10μm) and increasing the cathode content by 8× (Yang et al. (2021c)).

Scalable SSB designs should mimic conventional LIBs where ions flow continuously between the anode and cathode via well percolated pores filled with a liquid electrolyte. Solid state batteries employ percolated regions of solid electrolyte materials instead of percolating pores. Thus, cathodes contain both active material (cathode) and solid electrolyte and are known as composite cathodes **(Fig.1.7b)**. Solid state cathodes can be processed by either direct mixing approaches or multi-step infiltration processes. The latter process requires infiltration of the solid electrolyte either via solvent or melting directly onto a preformed cathode sheet (Chen & Vereecken (2019); Xiao et al. (2021)). Infiltrating cathode material into a porous framework has been widely explored within the solid oxide fuel cell community and utilizes facile processing approaches (tape casting) which enables high densities (>98%) and rigid electrolytes. Porous frameworks are known as bilayer or tri-layer cells which are promising for large-format ASSB production (Zhang & Fujimori (2020); Zhao et al. (2020)). Bi/tri-layer architectures require the use of a colloidal precursor or slurry which combines a binder and pore former (Fig. 1.7c-iv). When the film is sintered the pore former will burn away leaving behind a porous structure (Hitz et al. (2019); Liu et al. (2018)). Recent reports have shown that composite architectures with thin dense solid electrolytes can demonstrate higher energy densities (195 Wh kg^{-1}) with 99% coloumbic efficiency (Liu et al. (2018)). Higher active material density (>95%) and thicker electrodes (>5 mAh.cm^{-2}) can further increase the cell-level energy density **(Fig.1.7b-iii)** (Judez et al. (2018)). However, thick cathodes can be challenging to implement in practice because of mechanical failure (cracking) and transport limitations (Kato et al. (2018)). Ineffective ion and electron transport within thicker electrodes can contribute to low-material utilization and poor rate performance (Hlushkou et al. (2018)). Therefore, identifying cost-effective manufacturing processes which provide exquisite control over multi-material processing is critical for thick electrodes to be realized (Xu et al. (2021b)).

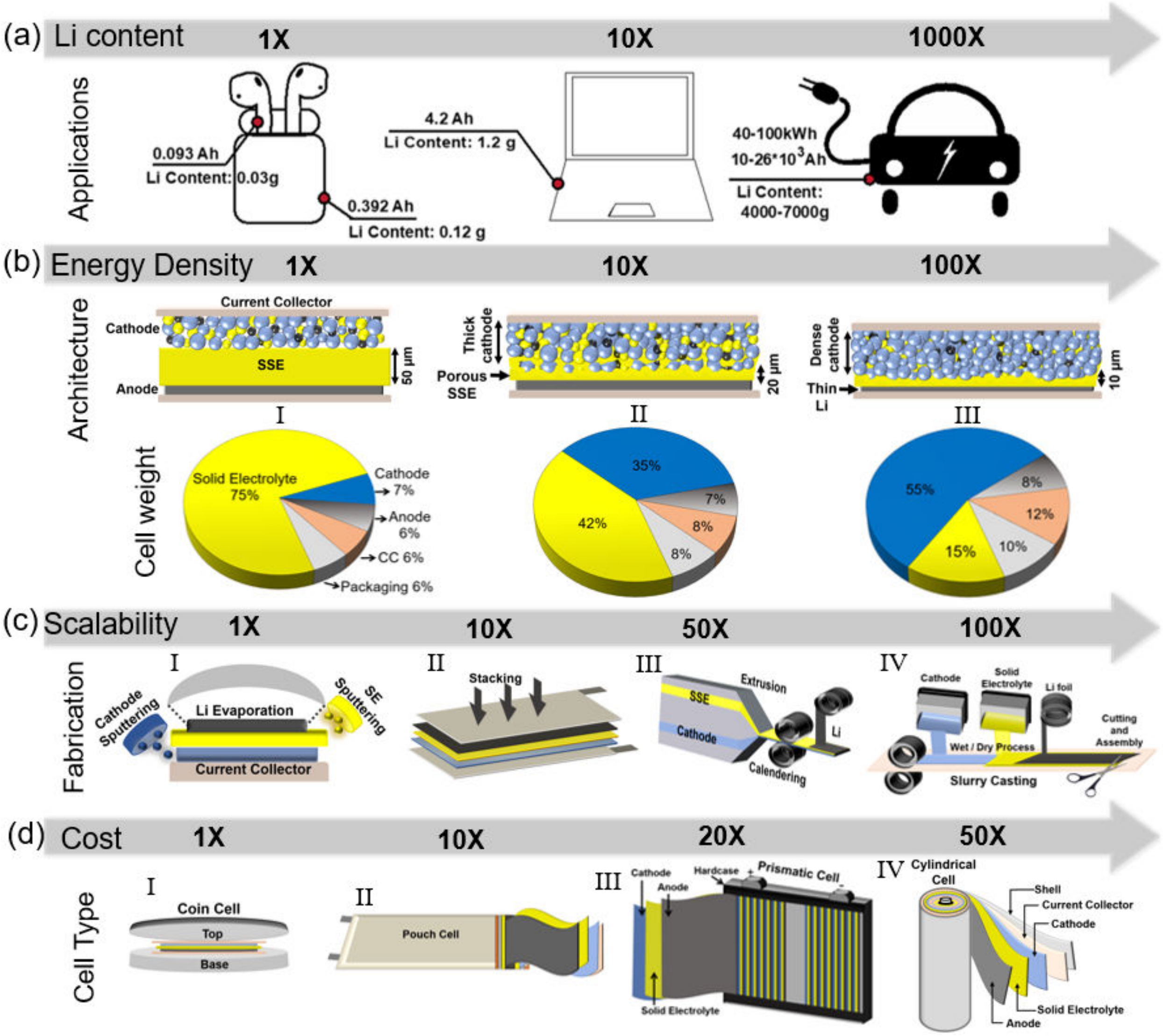

Figure 1.7: Schematic of (a) battery-driven applications, (b) battery architecture from low to high energy density, corresponding weights of battery components (c) manufacturing processes of ASSBs with respect to scalability and (d) cell type with respect to production cost. *Copyright 2022, Elsevier*.

1.8 Scalable Manufacturing of All Solid-state Batteries

The environmental footprint and technoeconomics of SSB manufacturing rely heavily on material supply chain, recycling and repurposing opportunities. Simultaneous development of materials processing, cell design, and recycling strategies is important for rapid integration of solid state batteries. There is growing attention on recycling conventional LIBs where materials (mostly cathodes) are recovered from several extractive metallurgical approaches (pyrometallurgy, hydrometallurgy) and direct recycling (Tan et al. (2020a); Xu et al. (2020); Azhari et al. (2020)). Direct recycling approaches may be adopted in SSB because individual components can be directly separated. Supply chain (mining, processing, refining, shipping) for solid state batteries is anticipated to be more challenging than conventional LIBs, due to the use of critical elements (e.g.; Ge, Ta) and increases in lithium content (Fig. 1.7a,b). Both resource availability and materials processing costs will be critical for identification of key battery chemistry and architectures for adoption of next generation all solid state batteries.

Materials selection and processing approach will dictate strategies for manufacturing large-format solid-state batteries. Currently available solid-state batteries are thin film and have low (<1 mAh) nominal capacities. Most thin film architectures employ vacuum deposition methods which are difficult to scale-up for EV applications. In addition, many solid-state battery materials are air/moisture sensitive and require inert environments for processing. All of these considerations are critical for engineering low-cost solid state batteries (**(Fig.1.7c,d)**).

Recently, there have been promising commercial demonstrations which utilize roll-to-roll manufacturing to produce multi-layered solid-state batteries with 20 Ah cell capacity. Despite this progress there are three key manufacturing challenges to overcome: (1) thin defect-free solid electrolyte processing, (2) dense composite cathode fabrication and (3) thin lithium metal processing. A host of approaches are being considered to address these challenges including and not limited to tape casting, screen printing, extrusion and aerosol deposition. Tape casting or screen-printing method are widely examined for composite cathodes and solid electrolytes because it can enable high-throughput and scalable production volumes. However, high-throughput coating processes may require an additional calendaring step to alter part density. Extrusion or melt processing is being examined for lithium metal and alloy materials. Processing of lithium metal is a significant challenge because any contamination can drastically impact performance. Furthermore, a lot is unknown regarding how shear- and stress- experienced during processing can influence lithium metal properties. Finally, three-dimensional printing approaches are also be examined because they enable solid state batteries with controlled microstructures. All 3D printed batteries can offer a wide range of form factors and low manufacturing cost with increased scalability (Ahn et al. (2022)). Recently, Sakuu Inc. successfully employed their multi-material 3D printing technology to manufacture solid-state batteries in their 2.5 MWh pilot facility. Three-dimensional printing strategies (e.g.; inkjet printing) need to be further explored but are unlikely for large capacity applications.

1.8.1 Manufacturing of solid electrolytes

A wide range of inorganic (ceramic) and organic (polymer) Li-ion conductors are being examined for solid-state batteries. Technoeconomics analyses suggest that the solid electrolyte should be less than 35% of the total manufacturing cost (Balaish et al. (2021); Schnell et al. (2018)). Unfortunately, current solid electrolyte processing is estimated to be nearly 70% of the cost associated with manufacturing a solid state battery. One kilogram of LLZO, LGPS and Li_6PS_5Cl costs \$2000, \$69,500 and \$36,000 (Balaish et al. (2021); Karabelli et al. (2021)). The cost of solid polymers such as PEO and Li-salt is \$700/kg and \$1,980/kg. Processing cost of polymer or polymer-composite electrolytes (e.g., PEO-LLZO, PEO-LGPS) can therefore vary from \$7,000-50,000/Kg. Due to simpler and cost-efficient processing, polymer or hybrid electrolyte based SSB manufacturing is anticipated to cost less than oxides or sulfides (≈\$110/kWh). Material selection and manufacturing choice will dictate this end cost.

Garnet oxides (LLZO) are known for outstanding mechanical rigidity ($E_{modulus}$ = 129 GPa), satisfactory ionic conductivity (10^{-4} S/cm) and excellent electrochemical stability (Delluva et al. (2020)). While other inorganic electrolytes are known to form reactive interphases at the interfaces, LLZO only forms a slightly less ion-conducting (tetragonal) but stable interphase. Synthesis of LLZO requires mechanochemical milling (e.g.; ball milling) and high temperature sintering. The sintering step generally requires additional sacrificial LLZO as "mother-powder" to prevent Li loss (Yang et al. (2021b)). High temperature processing is critical for grain growth and densification of polycrystalline LLZO. High densities of LLZO (>90%) are attained through pelletization via external isostatic pressure (>300 MPa). Rapid induction hot pressing (RIHP) has been shown to be an effective strategy for achieving higher densities (>98%) (Sharafi et al. (2016)). These processing strategies, when transferred to the plant scale, require large footprints and high production costs. Freeze tape casting of porous 3D LLZO scaffolds (<100μm) is one of the "pressure-free" scalable approaches which can be implemented directly in solid-state batteries (Buannic et al. (2019); Shen et al. (2020)). The 3D scaffolds were also featured in bi/tri-layer SSE architectures, which can be scaled up via tape casting (Hitz et al. (2019)). Another pathway for alleviating pressure during processing is to utilize aerosol and vacuum-based deposition processes. Pulsed layer deposition (PLD), magnetron sputtering and atomic layer deposition (ALD) are also effective in producing ultrathin (<10μm) solid electrolytes without stack pressure and at lower temperatures ($\leq$650C) (Loho et al. (2017); Saccoccio et al. (2017); Kazyak et al. (2020b); Sastre et al. (2020); Pfenninger et al. (2019); Ohashi et al. (2020)). Processing conditions (e.g. temperature, gas flow rates and deposition rate) all influence material properties (Sastre et al. (2019); Lobe et al. (2021)). Currently, a significant gap still exists between thin film and bulk solid electrolytes in terms of transport properties (e.g. ionic conductivity). Loss of lithium during processing is a considerable challenge for developing resilient processing chains.

Glassy amorphous sulfides (LPS, LGPS) and argyrodites (Li_6PS_5Cl) electrolytes display narrower voltage window but superior room temperature ionic conductivity when compared to oxides. Soft amorphous sulfide electrolytes offer several advantages including good interfacial contact and low grain boundary resistance (Liu et al. (2013); Ohno et al. (2020); Kerman et al. (2017)). Sulfide solid electrolytes are typically synthesized using mechanochemical milling (>40 hours) and can be compressed into thin pellets (<200 μm) (Kudu et al. (2018); Dietrich et al. (2017); Stöffler et al. (2019)). There are several on-going efforts to synthesize sulfide solid electrolyte via solution-processing approaches (Ghidiu et al. (2019); Miura et al. (2019)). Solution-processing synthesis may enable high volume materials production and low costs. However, solution-processing conditions can have a significant impact on transport properties (Hatz et al. (2021)). Stack pressure and heat treatment influences the densification, crystallinity and ionic conductivity of both electrolytes **(Fig.1.9a)** (Garcia-Mendez et al. (2020); Wang et al. (2018); Cronau et al. (2021)). Halide based electrolytes (e.g.; $Li_{3-x}M_{1-x}Zr_xCl_6$) are also an attractive class of superionic conductors (>1.4 mS/cm) and demonstrate better electrochemical stability (>4V) due to incorporation of halogens as anions **(Fig.1.9b)** (Liang et al. (2021); Manthiram et al. (2017a); Kwak et al. (2021); Yu et al. (2021); Riegger et al. (2021)). Unlike garnet oxides, sulfide solid electrolytes cannot be processed via vapor deposition approaches and thus require hot-, warm-, or room temperature isostatic pressing to achieve viable thicknesses and densities. Furthermore, sulfide solid electrolytes cannot form porous scaffolds and thus are Incorporated directly with the cathode material in composites.

The last class of solid electrolytes being examined are organic solid polymer electrolytes. These electrolytes combine a binary lithium salt with a bulk polymer material (Hallinan & Balsara (2013); Armand (1983a); Popovic (2021a); Zaman et al. (2019)). Lithium ions motion is governed by the polymer chain segmental mobility. The room-temperature ionic conductivity and mechanical stiffness of polymer electrolytes are lower than most inorganic solid electrolytes (<10^{-4} mS/cm, 2 MPa) (Harry et al. (2014)). Hybrid solid electrolytes are a family of solid electrolytes which combine a polymer and inorganic ion conductor. This hybrid or composite approach can lead to improved mechanical and transport properties (Zheng et al. (2016b); Liu et al. (2015); Zhang et al. (2017b)). Oxide-based HSEs demonstrate ionic conductivity up to 0.4 mS/cm and sulfide-based hybrid solid electrolytes demonstrated an ionic conductivity approaching 0.11 mS/cm **(Fig.1.9a)**

(Lee et al. (2021b); Oh et al. (2021)). Hybrid and all organic solid electrolytes can be processed under low temperature and pressure conditions using traditional coating approaches (Popovic et al. (2021)). However, similar to inorganic solid electrolyte, organic solid electrolytes can suffer from dendrite propagation, low ionic conductivity, mechanical and thermal stability (Chen et al. (2017a)). High solid electrolyte market penetration is dependent on developing low temperature, low pressure, and low cost manufacturing strategies. Traditional manufacturing steps include mixing, annealing, sintering, thinning/ and stacking. The quality of thin electrolytes processed via coating routes is highly dependent on coverage speed, viscosity, mixing parameters and volume flow **(Fig.1.8)**. Ultimately, there needs to be more work on understanding how processing conditions impact solid electrolyte performance before scale up can be realized.

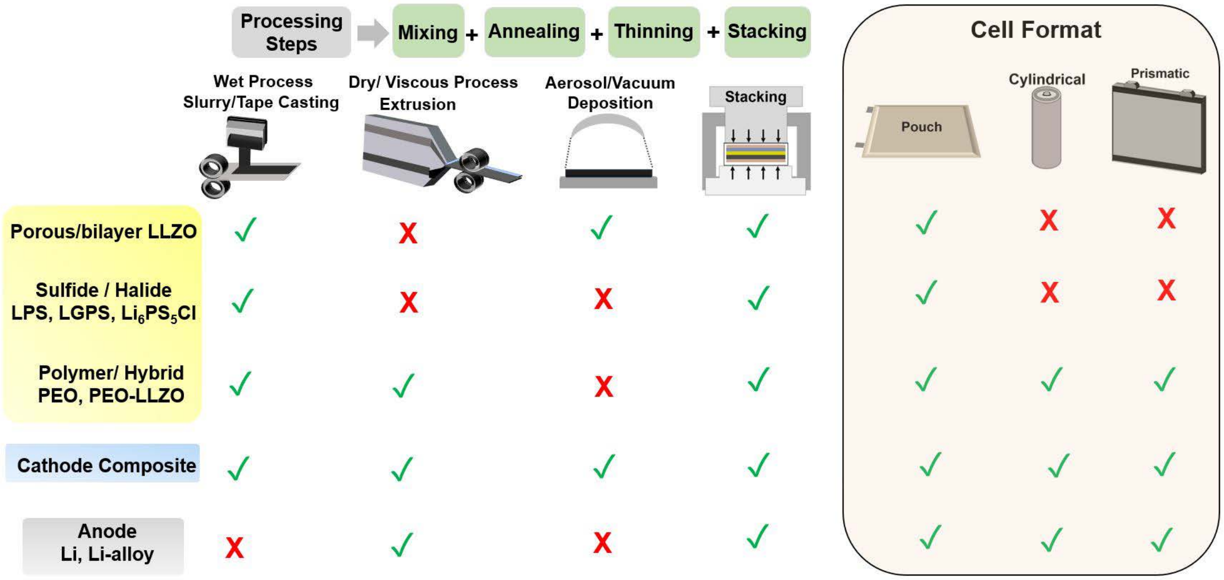

	Wet Process Slurry/Tape Casting	Dry/ Viscous Process Extrusion	Aerosol/Vacuum Deposition	Stacking	Pouch	Cylindrical	Prismatic
Porous/bilayer LLZO	✓	X	✓	✓	✓	X	X
Sulfide / Halide LPS, LGPS, Li_6PS_5Cl	✓	X	X	✓	✓	X	X
Polymer/ Hybrid PEO, PEO-LLZO	✓	✓	X	✓	✓	✓	✓
Cathode Composite	✓	✓	✓	✓	✓	✓	✓
Anode Li, Li-alloy	X	✓	X	✓	✓	✓	✓

Figure 1.8: Prospects of available scaled up technologies and cell formats for solid-state battery manufacturing. Each technology requires three key steps to check: mixing of materials, annealing and thinning/calendering, followed by stacking cell assembly. The figure shows better opportunity for slurry/tape casting manufacturing for solid-electrolytes and cathodes. For metal anode processing, extrusion/pressure-assisted lamination is preferred. *Copyright 2022, Elsevier*.

1.8.2 Manufacturing of Cathodes

Composite cathodes contain an active material (CAM >80 wt%), an electronic conductor (>10 wt%) and an ionic conductor (>10 wt%). Solid state cathodes are processed via traditional wet chemistry based coating manufacturing approaches. There has been ongoing interest in highly viscous and dry processing of composite cathodes via extrusion and powder bed mixing in order to minimize solvent handling (Zhang & Fujimori (2020)). For further densification of composites, co-sintering approaches (>700°C) are often employed which can lead to unwanted side reactions at the interfaces due to cross-diffusion (Park et al. (2016); Kim et al. (2020)). Composite cathodes rely on intimate contact between each constituent (e.g. cathode, electrolyte, and carbon). Many materials experience chemical decomposition at these triple points (Miara et al. (2016)). Active materials undergo frequent volume expansion/contraction during cycling, which causes gradual degradation and interfacial cracking. Both ionic and electronic percolation in composites are dependent on the cathode-solid electrolyte particle size ratio. Numerous theoretical studies have investigated the impact of particle size and composition on the composite cathode energy density (Kim & Rupp (2020); Shi et al. (2020a)). In practice, transport limitations in thick electrodes and chemical decomposition need to be resolved to achieve similar performances with conventional cathodes. This may require advanced manufacturing approaches that enable precise control over electrode microstructure during processing (Dixit et al. (2019)).

Similar to solid electrolytes, a range of vacuum deposition techniques are being explored for ASSB cathodes. Electrodeposition of additive and binder-free cathodes is a promising approach that allows 100% utilization of cathodes in solid-state batteries (Zahiri et al. (2021)). Pulsed layer deposition (PLD) and RF-magnetron sputtering can enable additive-free deposition of thin film cathodes (e.g.; LCO, LFP) with precision control in nanoscale (Sastre et al. (2020); Delluva et al. (2020)). The fabricated battery architectures can potentially achieve highest relative fraction of active materials (>60% of cell weight) **(Fig.1.7b-**

iii). But due to slow processing speed and high maintenance cost, these techniques are challenging to scale up and replace conventional slot-die/tape-casting based manufacturing (Hatzell & Zheng (2021)). Aerosol deposition enables room temperature fabrication of dense cathode films (LFP, NMC) via ejecting cathode particles from a source material (Kim et al. (2013); Iwasaki et al. (2014)). Despite the advantages, vacuum deposition techniques lack scalability to m^2/min levels. These are also challenging to apply in sulfur-based cathodes. Therefore, facile slurry-based and sintering-free coating of dense composite cathodes are considered to be industrially adaptable for ASSBs. The slurry based processing is comprised of conventional LIB coating strategies: wet/dry mixing of composites, layer formation, stacking and lamination **(Fig.1.8)** (Schnell et al. (2018)). For EV-compatible operation, cathodes must deliver a specific capacity of 500 Wh/kg^{-1} and areal capacity of >5 mAh/cm^2, which requires a thicker (>100 μm) or denser cathode (>95% active loading) (Randau et al. (2020)). Chemo-mechanical effects dominate at the cathode|SE interface and within the bulk cathode which currently limits the lifetime of these thick cathodes (Koerver et al. (2018); Shi et al. (2020b); Minnmann et al. (2021)). Therefore, the slurry-based method for ASSB may require higher stack pressure to achieve higher relative density (Wang et al. (2021c)). Tape casting or screen printing, followed by a calendering step will be a suitable approach for scaled-up production.

1.8.3 Manufacturing of anodes

There is a significant interest in using alkali metal-based anodes (e.g.; Lithium) in solid state batteries because the absence of a liquid solvent can reduce irreversible active material loss (Lin et al. (2017)). Solid electrolytes, if engineered effectively with lithium metal, can regularize lithium deposition-dissolution dynamics and enhance cycling efficiency of battery. Lab-scale and benchmarking studies typically employ an excess amount of Li metal (>200 μm) which is irrelevant for real applications. Li-metal thickness can be reduced to 10-20 μm by using stack pressure or extrusion (Mauger et al. (2017); Popovic

(2021b)). However, excessive handling and processing of lithium can increase the probability of creep induced deformation and pulverization which greatly affects Li|SSE interfacial homogeneity. Surface defects and irregular morphologies in such at electrode interfaces can drive the formation of unwanted filaments and dendrites (Kazyak et al. (2020b)). Lithium foil processing will require an energy-intensive purification process and inert (Argon) working environment. Due to its adhesive nature, roll-to-roll processing for lithium is difficult to employ. Instead, a lamination process via extrusion can be implemented to secure the anode material on the current collectors or solid electrolytes **(Fig.1.8)** (Schnell et al. (2018)). Surface passivation must be carried out in order to protect the anode during manufacturing steps that may occur in non-inert environments (Duffner et al. (2021)). A lithiophilic solid electrolyte surface is important for contiguous contact with the anode. The solid electrolyte surface can be modified via chemical or physical treatment (Sharafi et al. (2017a); Krauskopf et al. (2019c)). Artificial coatings/interlayers are widely used for solid electrolytes to avoid electrolyte decomposition when in contact with lithium metal (Xu et al. (2018); Han et al. (2017); Riegger et al. (2021)). These also improve lithium adhesion properties during battery cycling and prevent volume changes. The interlayers are employed by forming stable ion-conducting interphases, either by an *in situ* reaction or the addition of a surface coating. Another approach to processing lithium metal is melt-induced stacking and vacuum based deposition (Kazyak et al. (2020b); Sharafi et al. (2016); Connell et al. (2020); Chen et al. (2021b)). Melt-induced infusion is a convenient approach which allows plastic flow of lithium to achieve better contact with electrolyte (Xu et al. (2017)). Both techniques enable thin lithium layers but are too costly for high throughput production. In addition, these techniques are generally applicable for solid electrolytes with high yield strength and thermal stability (e.g.; LLZO).

One of the most exciting and promising approaches is an anode-free architecture (Wang et al. (2020a)). This approach can potentially eliminate the cost of anode manufacturing and increase gravimetric and volumetric energy density by 10% (Salvatierra et al. (2021)). However, there are many challenges that need to be overcome until anode-less architectures are realized. A large volume change during the first charge coupled with rapid capacity loss are common with anode-free architectures (Heubner et al. (2021)). Any lithium lost during discharging cannot be recovered (“dead Li") which leads to low coulombic efficiencies. Interfacial chemo-mechanics within the anodic current collector and solid electrolyte becomes increasingly important as unstable charge transfer reactions can drive delamination (Davis et al. (2021); Menkin et al. (2021); Chen et al. (2021c)). Improper contact between the solid electrolyte and current collector can lead to failure via immediate shorting (Ning et al. (2021)). Electrodeposition (charging) and dissolution (discharging) can be altered via an applied pressure, controlled surface energy, controlled surface morphology, and variable applied temperature (Fang et al. (2021)). While there are many technical challenges associated with attaining high performing anode-less geometries, there are significant gains in terms of manufacturing costs if achieved.

1.8.4 Effect of pressure and temperature on battery manufacturing and performance

External operating conditions during battery operating and battery manufacturing can play a large role on cell performance and plant design consideration. The conditions include working environment (e.g.; inert or ambient conditions), stack pressure, and processing temperature. Pressure and temperature are two important cost and rate determining factors in all the aspects of SSB production (material synthesis, cell assembly and cycling). During cell assembly, stack pressure and heat treatment are frequently employed to improve interfacial contact (Sharafi et al. (2017a); Han et al. (2017)). Artificial coatings at the interfaces can also aid in improving interfacial resistances but result in an additional step in manufacturing line Han et al. (2017). Overall, pressure and temperature can have significant impacts on the material properties. In particular, yield strength of both solid electrolyte and lithium is governed by the pressure dependent material density and calendaring. High temperature can exacerbate chemical decomposition and lithium loss during processing but may increase packing density. Thus, processing pressure and temperature can have competing results in each component.

Mechanically robust oxide materials (e.g.; LLZO) typically can withstand high pressure (>200 MPa) and temperature (300°C). Operation under elevated pressure and temperature has been shown to be effective way to lower the interfacial resistance between lithium metal and solid electrolytes (1-10 Ωcm^2) **(Fig.1.9b)** (Krauskopf et al. (2019c); Zhang & Fujimori (2020)). Thermal approaches to improve the wettability between lithium metal and sulfides and argyrodites-types solid electrolytes are challenging because many solid electrolytes exhibit chemical decomposition against Li metal, which is severe at high temperature. Therefore, stack pressure is the only mean to improve contact and prevent delamination (Krauskopf et al. (2019c); Bonnick et al. (2019)). Excessive stack pressure can cause electrolyte fracture and shorting (extrusion of lithium metal) (Doux et al. (2020a); Dixit et al. (2020c)).

Unwanted failure due to delamination, void formation, and/or dendrite propagation can occur in cells with low interfacial resistance (Wang et al. (2021a)). Degradation mechanisms are driven by material properties, interfacial interactions and operating conditions. These degradation processes lead to capacity decay and limits rate performance. Less than 15% capacity loss over 1000 cycles is necessary for real applications. Therefore, pressure and temperature during electrochemical cycling should be monitored to benchmark cell testing protocols. A recent report on a solid-state Li-S batteries (lab-scale) demonstrated good charge-discharge capacity (>3 mAh/cm^2 at 60°C) at an applied pressure of 30 MPa (Bonnick et al. (2019)). Solid state batteries require extensive pressure in material processing and operation. It is unclear how these pressure could be maintained in tradition battery geometries (e.g. pouch, jelly roll, etc.). Rigid external casing may be a pathway to control pressure without external pressure control. Garnet oxides have a

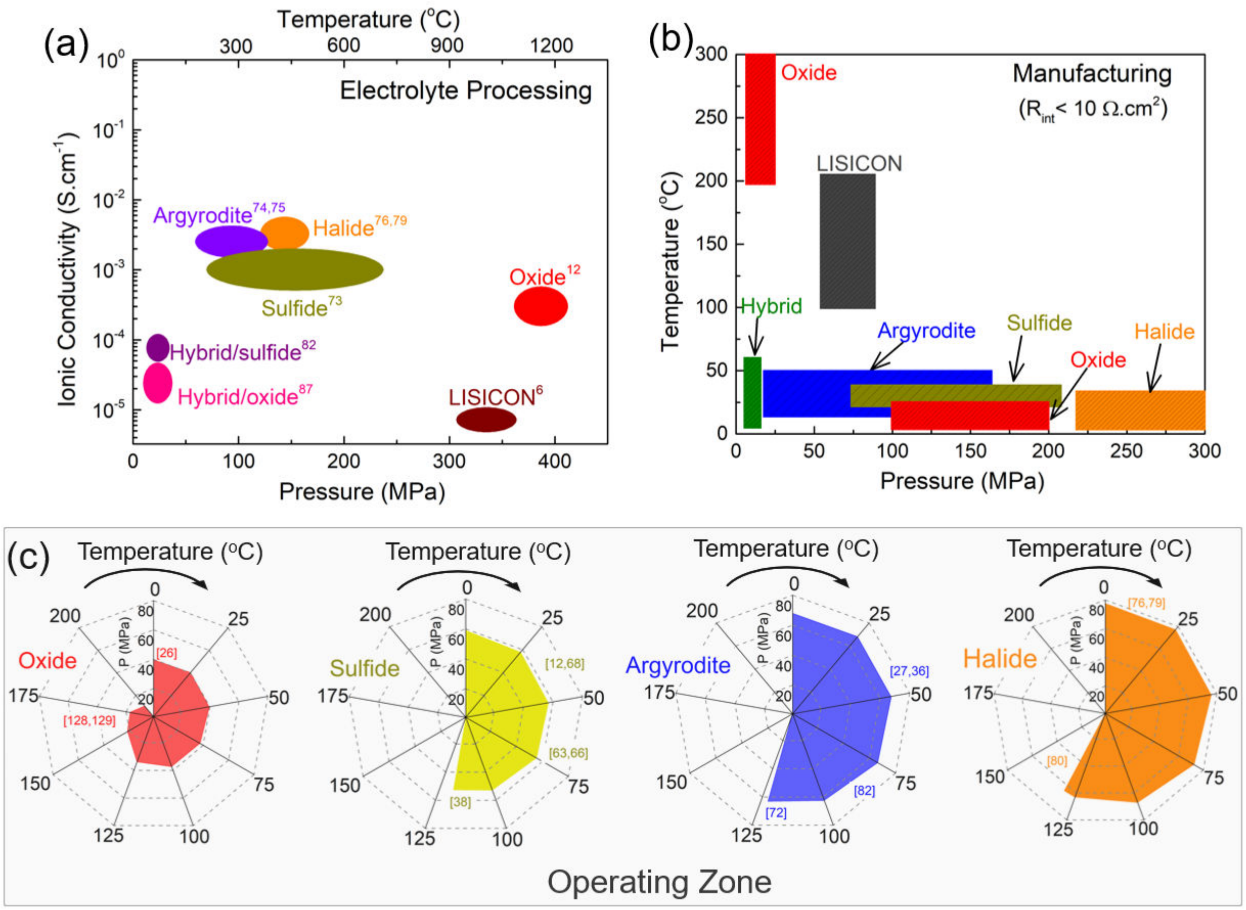

Figure 1.9: Role of pressure and temperature in different steps of manufacturing solid-state batteries with solid electrolytes: (a) electrolyte processing (ionic conductivity as a function of processing pressure and temperature), (b) cell manufacturing for good interfacial contact (<10 Ωcm^2), (c) operating range for batteries with oxide, sulfide, argyrodite and halide electrolytes. *Copyright 2022, Elsevier*.

wider temperature range (beyond the melting point of Li) but a small pressure range due to low ductility (<40 MPa) **(Fig.1.9c)** (Kinzer et al. (2021); Jin et al. (2018)). Argyrodites and sulfides are recommended to operate below 120°C but can withstand large stack pressure (>50 MPa) **(Fig.1.9C)** (Spencer Jolly et al. (2021); Kasemchainan et al. (2019)). Overall, material selection for SSBs is critical to design battery architectures and predict manufacturing strategies. Technoeconomic analyses should precede development because variably operating and manufacturing conditions may further increase the cost of the battery.

1.8.5 Cell formats in battery manufacturing

Conventional lithium ion batteries utilize cylindrical (jelly-roll), prismatic or pouch cell formats. Each of these formats present specific advantages and disadvantages when implemented with solid state battery materials. The most common form factor of currently produced SSBs is planar (prismatic or pouch cells). Planar cells retain the structural integrity of the solid electrolytes **(Fig.1.7d)** (Notten et al. (2007); Ashby et al. (2020)). For EV applications, this geometry offers a facile way for stacking batteries while maintaining uniform stress distributions on the cell. There is a significant interest in combining structural elements in a car with the battery pack. Planar cells are envisioned to enable this functionality via vertical stacking or Z-stacking of cells (Wu et al. (2020); Xu et al. (2021b)). Pouch cell are currently the most widely used format in solid-state battery manufacturing and can be integrated with all types of solid electrolytes **(Fig.1.8)**. It is also very important to adopt bipolar packing strategies for more effective material utilization (Schnell et al. (2020)). Cylindrical cells offer higher capacity and output voltage via assembling in series and parallel connection. These contain safer and stronger battery housing with well-defined production parameters. The cells consist of hard casing, winding format which provide excellent shock resistance in a module (Chen et al. (2021a)). However, most of the solid electrolytes lack mechanical flexibility and thus cylindrical formats are only envisioned for system with high polymer content (Wu et al. (2020); Li et al. (2019b)). Hybrid solid electrolytes are also promising because they can be integrated with a range of existing manufacturing approaches (roll-to-roll or extrusion based) **(Fig.1.8)**. High required stack pressure requirements will require the addition of stacking components (e.g., springs) into a battery housing which can dramatically increase the battery space and production cost. Therefore it is desirable that cells operated at or below 5 MPa. Ultimately, the choice of architecture is going to depend on the application. There are range of applications from portable electronics to electric vehicles which use vastly different architectures and system design.

1.9 Research Questions and Outlook

To enable high energy density, solid-state batteries will have to address the key interfacial challenges that are hindering their development. This requires novel battery and device engineering with proper tuning of parameters and modifying material synthesis and processing strategies. The literature survey in this chapter broadly focuses on the chemo-mechanical traits of solid-state battery components and interfaces. The buried solid|solid interfaces are primarily responsible for battery failure. Thus, understanding the transport and interfacial phenomena is highly important to engineering novel solid-state battery systems. The motivation of this work is to achieve a broad understanding of the transport and interfacial properties of solid-state battery constituents through in-depth electrochemical analysis and visualizing techniques. We hypothesized that the transport properties at various length scales are dependent on the processing-structure-function relationships of solid electrolytes and electrodes. Using various model systems, the behavior of the internal interfaces is rigorously studied under a variety of conditions. We briefly employed garnet LLZO electrolytes in our studies. Due to its higher chemical and thermodynamic stability than any other contemporary solid electrolyte, LLZO is an ideal model system for studying the transport phenomena in solid-state systems. In Chapter 3, we look to elucidate the transport mechanism and interfacial effects in hybrid solid electrolytes. Experimental evaluation of these buried interfaces is carried out via the use of advanced synchrotron-based characterization techniques. In Chapter 4, we briefly discuss the effects of operating conditions (e.g.; stack pressure and temperature) in solid-state batteries and how the interfacial evolution of Li metal dictates ion transport and cell stability. The experimental evaluations and findings are coupled with computational modeling. In Chapter 5, we investigate the chemo-mechanically induced stress evolution in solid-state batteries. Via operando stress monitoring, the evolution of stress parameters upon Li plating is evaluated in both symmetric and full cell configurations. Furthermore, we investigate the deposition properties of Li on an anode-free structure (current collector only). The outcome of these studies is expected to address the material and cell level issues of the current state of solid-state batteries.

Chapter 2

Experimental Methods

This chapter offers a broader understanding of the key electrochemical and characterization techniques that are used throughout this work. The customized experimental setups that are used for solid-state battery study are also discussed here. A detailed explanation of material synthesis and processing methods used in this thesis are included in subsequent chapters.

2.1 Battery Testing Setups

2.1.1 2-electrode Setup

All-solid-state batteries were assembled by a combination of pressure and temperature-based processing. A Shiny Li metal surface was attached to a LLZO pellet under stack pressure. For symmetric cells, two identical Li foils were used. A copper foil was used as a current collector. For full cells, only one side was treated with Li foil. Composite cathode foil then was attached to the other side of LLZO by applying a stack pressure. The cell assembly was then inserted into a modified pressure cell setup. The setup consists of a circular chamber where pressure can be applied by using two stainless steel plungers located at the top and the bottom. Two PTFE O-rings and compression nuts are used to tighten the plungers. The setup was then placed inside a compression jig. To maintain uniform pressure throughout the cell cycling period, a spring was attached to the compression jig. A load cell (pressure sensor) (Omega Engineering LCGD-20 KN) was placed under the cell to monitor the pressure change. The output voltage from the load cell was calibrated according to the pressure applied to the cell. To improve the signal-noise ratio, a strain gauge transmitter (Omega Engineering) was connected to the load cell. The setup is powered by a 20V DC power supply. The load cell output was tracked in real time by a data acquisition (DAQ) board. This setup allows the as-fabricated solid-state battery to operate under different stack pressure.

2.1.2 3-electrode Setup

A 3-electrode setup was prepared to isolate the electrode|electrolyte interfacial behaviors under static and dynamic conditions. This setup is different than what was used for typical symmetric and full cell setups, as described in the previous section. The 3-electrode cell configuration consists of a larger diameter of electrolyte (15-16mm) and two Li foils (4 mm dia) at the top and bottom. In addition, a small Li foil (2mm) was attached to a copper rod (2mm) and placed at the edge of the pellet from the top **(Fig.2.1)a**. This small Li foil acts as a reference electrode. The cell chamber is equipped with two stainless steel plungers and a larger cell body (20 mm dia) to house the assembled cell. The diameter of the top and bottom plunger was 7 mm and 19 mm respectively **(Fig.2.1)b**. Stack pressure was applied in the similar way mentioned in the previous section (spring-added compression jig). To monitor the alignment of the plunger and Li electrode, a small slot is made at the corner of the cell body. The pellet was fixed inside the cell body by putting a rubber O-ring around the edges.

2.2 Electrochemical Measurements

2.2.1 Electrochemical Impedance Spectroscopy

Electrochemical impedance spectroscopy (EIS) is a non-destructive technique that is widely used in understanding battery materials and underlying interfacial properties. EIS is extremely helpful in providing insights into battery degradation and failure. In this work, we have heavily used potentiostatic EIS (PEIS) where a small sinusoidal perturbation voltage (20-50 mV) was applied over a frequency range of 100 mHz to 7 MHz. Throughout the frequency range, processes at different timescales can be observed. The high-frequency responses correspond to faster processes like ion migration and low frequencies correspond to slow processes like diffusion. In a solid-state battery, there are several sources of resistance that originates from the crystal structure of the solid electrolyte

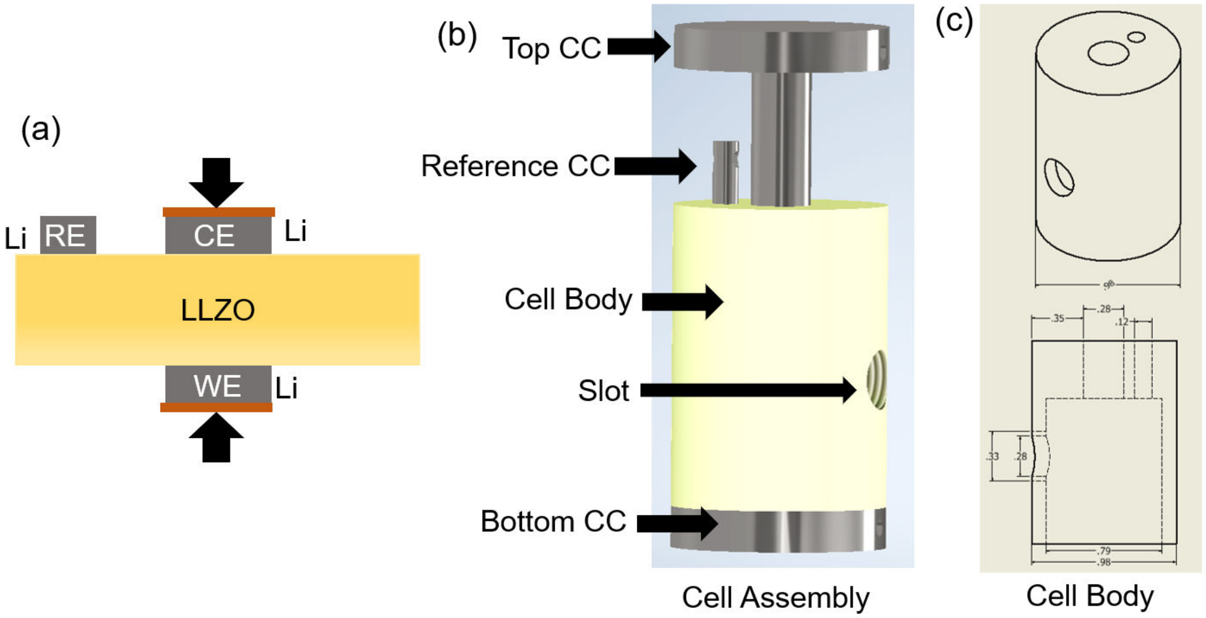

Figure 2.1: (a) Schematic of the 3-electrode setup for a symmetric cell. Li foil was used as a reference electrode. (b) 3D model of the 3-electrode setup assembly and (c) dimensions of the PEEK chamber.

to external interfaces that contributes to charge transfer. EIS is useful for tracking individual phenomena at different time scales and decoupling by measuring the frequency dependence of the resistance.

A PEIS measurement operates by the following equation:

$$V(t) = |V_0| sin(\omega t) \tag{2.1}$$

here V is the potential, V_0 is the perturbation voltage, ω is the frequency, and t is the time. The resulting current response will have the following form:

$$I(t) = |I_0| sin(\omega t + \phi) \tag{2.2}$$

The resulting impedance will be:

$$Z = \frac{V(t)}{I(t)} \tag{2.3}$$

Which is redefined by Euler's formula:

$$Z = |Z| \exp^{j\phi} = Re(Z) + Im(Z) \tag{2.4}$$

The profile of the Nyquist plot depends on the type of cell assembly used. For example, if EIS is performed on garnet LLZO with two ion-blocking electrodes (e.g., Silver, Gold), there are two sources of resistance that can be identified: bulk resistance and grain boundary resistance. These are followed by a low-frequency region, which corresponds to Warburg diffusion **(Fig.2.2a)**. In this work, EIS measurements with ion-blocking electrodes are used to measure the ionic conductivity of the solid electrolytes. With ion-conducting electrodes (e.g., Li metal), a third source of resistance is also observed which corresponds to interfacial resistance. The interfacial resistance (R_{int}) stems from a combination of charge transfer resistance (R_{CT}) and contact resistance ($R_{contact}$) **(Fig.2.2b)**. In a symmetric Li|LLZO|Li cell, a negligible diffusion process was observed at a low frequency, whereas in a full cell (LFP|LLZO|Li), cathodic Warburg diffusion was observed. The experimental spectra were fitted by RelaxIS software package. For equivalent circuits, resistor-capacitor (RC) models were considered for all cases. Instead of an ideal capacitor, a constant phase element (CPE) is used in RC circuits for allowing slight variations of electrochemical processes at different time constants. The calculated capacitance for bulk and grain boundary regions of LLZO are 10^{-11} F.cm^{-2} and 10^{-8} F.cm^{-2} respectively. The interfacial capacitance is a function of the contact area of ion-conducting electrodes and LLZO which varies from 10^{-6}-10^{-7} F.cm^{-2}.

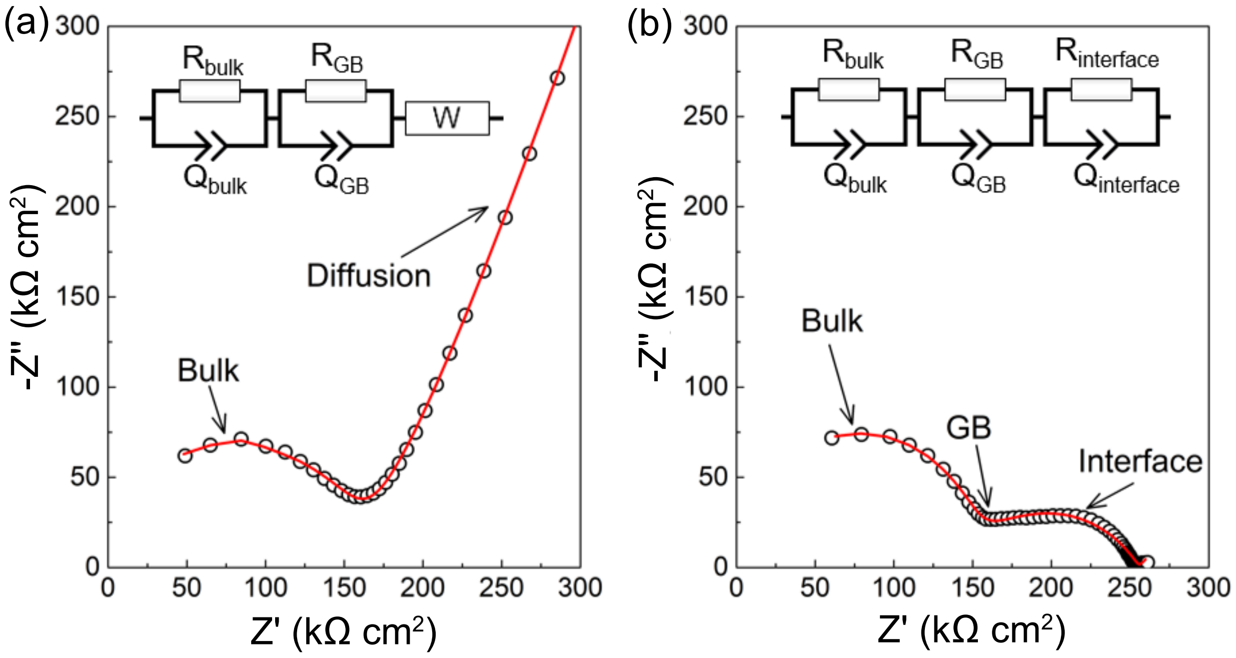

Figure 2.2: (a) A representative Nyquist plot for LLZO solid electrolyte with ion-blocking electrode and (b) ion-conducting electrode (Li metal). Corresponding equivalent circuits were also shown. Black circles represent experimental data and red line represents fitted data.

2.2.2 Measuring Ionic Conductivity

The ionic conductivity of a solid electrolyte, σ is proportional to the concentration of the mobile charge species and their mobility, given as

$$\sigma = \sum n_i q_i u_i \tag{2.5}$$

where q_i is the charge of the ionic species, u_i is the mobility of the ionic species and n_i is the number of the charged species. Ionic conductivity is electrochemically measured by calculating the resistance of the transport of a mobile ion. This is conducted by PEIS method where the high-frequency region (>0.1 KHz) is of interest.

$$\sigma = \frac{1}{R}\frac{L}{A} \tag{2.6}$$

where L is the thickness of the electrolyte and A is the surface contact area of the electrode and electrolyte. The activation energy (E_a) of the ion motion is measured by conducting PEIS over a wide range of temperatures (20-80°C). The ionic conductivity of the solid electrolytes increases as the temperature increases. The activation energy was calculated by using the Arrhenius equation. The role of blocking electrodes is critical in the proper measurement of ionic conductivity. In inorganic LLZO pellets, silver paste was used as ion-blocking electrodes which were painted on the surface of the pellets and dried under vacuum at 80°C. For hybrid electrolytes (PEO-LLZO), the films were placed in between two stainless rods and sealed by a heat tape.

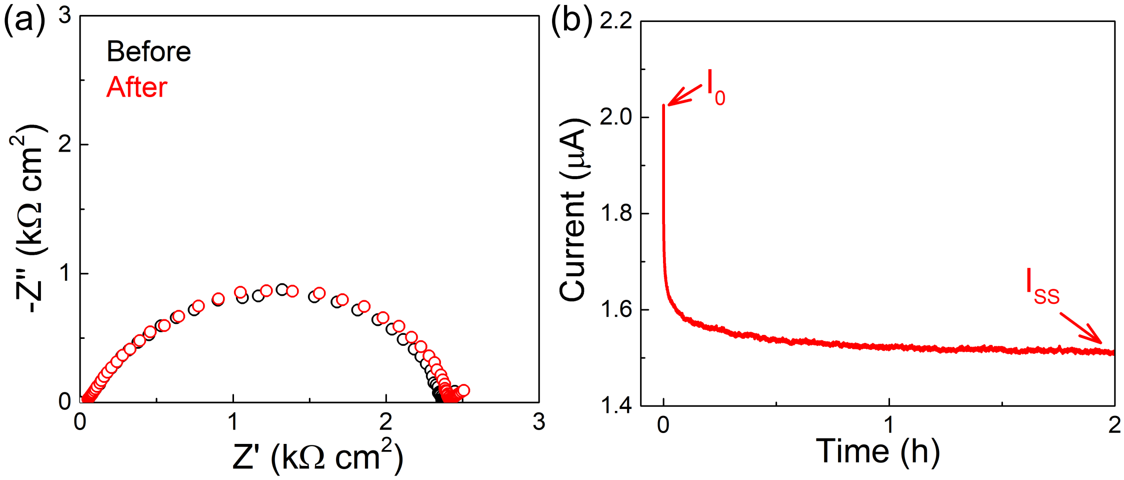

Figure 2.3: (a) Nyquist plots of a symmetric cell Li|PEO-LLZO|Li showing the change in cell resistance, before and after the DC polarization. (B) Current profile of the symmetric cell showing initial current (I_0) and steady-state current (I_{SS}).

2.2.3 Measuring Transference Number

Transference number is defined as the ratio of the electric current derived from the cation to the total electric current or, in another word, the fraction of the total current carried by a Li^+ ion. While ionic conductivity is considered as how fast the electrolyte can conduct ions, transference number signifies the efficiency of the ion transport. Transference number of an ion-conducting systems is usually derived from the Nernst-Einstein equation:

$$t_{Li}^{+} = \frac{\mu_{+}}{(\mu_{+} + \mu_{-})} = \frac{\sigma_{+}}{(\sigma_{+} + \sigma_{-})} = \frac{D_{+}}{(D_{+} + D_{-})} \tag{2.7}$$

Here, μ is the mobility of the charge carrier, σ is the specific ion conductivity, and D is the diffusion coefficient. Electrochemcially, transference t_{Li}^{+} number of Li-ion (cation) is derived from conducting both EIS and chronoamperometry. The latter is a time-dependent technique where a square-wave potential is applied to a symmetric cell and the current in the working electrode was measured. The current-time dependence is a diffusion-controlled process that occurs due to a concentration gradient until a steady state is achieved **(Fig.2.3)**. At steady state, the concentration gradient does not change which means ion motion through migration is compensated by the diffusion process.

The initial current flowing through the system is derived by the following equation

$$I_0 = \frac{\sigma}{k} \Delta V \tag{2.8}$$

Here, k is the cell constant which is defined by the surface area of the electrodes. After applying I_0, the cell reaches a steady state where the concentration gradient does not change with time ($J_{migration}$ = $J_{migration} \approx 0$. As a result, I_{SS} can be derived as

$$I_{SS} = \frac{t_{Li}^{+} \sigma}{k} \tag{2.9}$$

Which shows that

$$t_{Li}^{+} = \frac{I_{SS}}{I_0} \tag{2.10}$$

The technique applies a small amount of voltage to induce a small polarization (10 mV). However, after reaching the steady state, charge transfer resistance and contact resistance experience a slight increase which can be measured by EIS. The initial and steady-state current equations then can be modified to:

$$I_0 = \frac{\Delta V}{k/\sigma + R_0} \tag{2.11}$$

and

$$I_{SS} = \frac{\Delta V}{k/\sigma t_+ + R_{ss}} \tag{2.12}$$

The initial and steady-state current and voltage are then inserted in the Vincent–Evans equation to determine the t^+_{Li} value of a solid electrolyte.

$$t^+_{Li} = \frac{I_{SS}(\Delta V - I_0 R_0)}{I_0(\Delta V - I_0 R_{ss})} \tag{2.13}$$

2.2.4 Cycling of Symmetric and Full Cells

Chronopotentiometry was applied to evaluate the cycling performance of the symmetric and full cells. For symmetric cells, a fixed current was applied over time to record the voltage profile under different operating conditions. The charge/discharge (plating/stripping) cut-off voltages were limited to ±5V. For full cells, the operating voltage range was 2.5-4V for LFP and 2.8-4.2V for NMC.

2.3 Synchrotron X-ray Nanotomography

Failure mechanisms in solid-state batteries mostly occur at the buried interfaces. Using conventional imaging tools (such as optical microscopy or scanning electron microscopy) limits the prospect of extracting topographic information from the buried interfaces. X-ray-based imaging techniques in these case provides significant advantages as the transmission of X-ray over a bulk area of the sample can obtain a high-resolution spatial mapping of interfaces. X-ray interacts with the matter in three ways: attenuation, scattering, and transmission. Preparation of a sample for X-ray imaging thus requires proper optimization to maximize the signal/noise ratio. The spatial resolution generally ranges from 10 microns to 30 nm (Dixit et al. (2021); Shen et al. (2019b); Lewis et al. (2020)). Synchrotron-based X-ray sources differ from conventional sources as they offer a higher energy range and brilliance. As a result, higher spatial resolutions can be obtained in synchrotron sources with smaller samples (small field of view). This is beneficial for probing solid-state battery interfaces and extracting information on mesoscale transformations where two or more dissimilar interfaces can be present. In a typical tomography experiment, X-rays pass through the sample and are partially absorbed and transmitted based on the material density. The transmitted X-rays are optically by a scintillator and then captured by a detector. A two-dimensional projection is created (radiography) with necessary information regarding the adsorption of the material. Upon sample rotating to 360°C, multiple projects are taken along the z-axis. Based on the sample thickness, an attenuation coefficient μ(x,y) can be identified. If the X-ray beam penetrates a sample with an angle of incidence, Θ, the x-ray intensity will decrease by following the Beer-Lambert Law:

$$I_{\Theta}(z) = I_0 e^{-\int_{-\infty}^{\infty} \mu(x,y) ds} \tag{2.14}$$

Here, Z is the Orthogonal direction to beam projection. The resultant projections at each angle of rotation along the beam path can be derived by

$$P_{\Theta}(z) = \int_{\infty}^{\infty} \mu(x(\Theta,s,z),y(\Theta,s,z))ds \tag{2.15}$$

To reconstruct the physical quantity distribution (orthogonal projections), first-order Fourier Transform was performed on a set of projections.

$$\hat{P}_{\Theta}(k_z) = \hat{\mu}(k_x = k_z sin(\Theta), k_y = -k_z cos(\Theta)) \tag{2.16}$$

here, i = x,y,s,z are the Fourier space equivalents of the real-space variables. Then by us-

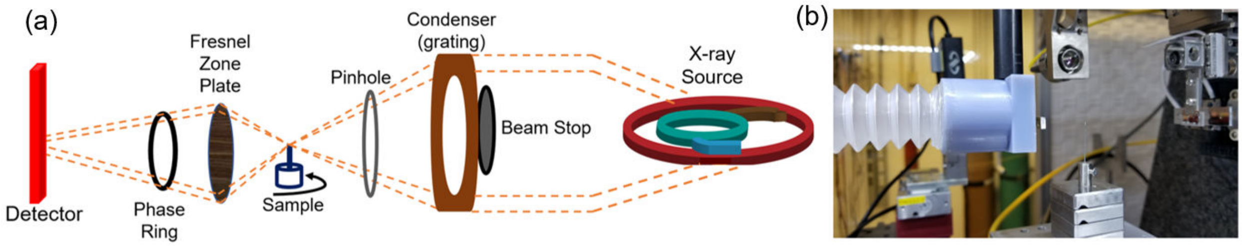

Figure 2.4: (a) Schematic of the X-ray nanotomography source (APS beamline 32ID). (b) Snapshot of the experimental setup.

ing Fourier Slice theorem, an inverse 2D Fourier transform was carried out. This process is carried out in multiple iterations. Solutions of the inverse Fourier transform (reconstruction algorithm) were utilized for reconstructing the 2D projections. To improve the image quality, we followed the following steps: phase retrieval, ring artifact removal, and noise removal. After that, a center of rotation was identified and raw projections are stacked from the beginning to the end along the z-axis. Typical reconstructions for a large area sample pixel can take a few minutes to several hours for reconstruction based on the setup parameters and the computational power accessible. Synchrotron X-rays provide a comparatively higher temporal resolution which lowers the acquisition time at high resolution. Reconstruction yields a stack of images sliced along the vertical direction in the sample (parallel to the projection axis). There are several open-source packages available to carry out the image reconstruction process. In this work, we employed two open source algorithms GRIDREC and SIRT (simultaneous iterative reconstruction technique) to compare and verify image quality (Carlo et al. (2014); Rivers (2012)).

For image analysis, several segmentation methods are widely used in different image analysis applications. Based on the contrast difference between two or more phases, a contrast thresholding can be set for segmenting each phase. This either can be carried out in open source software (imageJ, Dragonfly) or programming packages (MATLAB, Python). This method is applicable if there are strictly two phases within the system with a sharp difference in the respective grayscale values.

In this work, we use a high-resolution transmission X-ray microscopic (TXM) source (stationed in the Advanced Photon Source of Argonne National Lab) for imaging hybrid solid electrolytes. The synchrotron X-ray nanotomography was carried out at beamline 32-ID-C of Advanced Photon Source, Argonne National Laboratory **(Fig.2.4)**. Filtered monochromatic X-rays at 8 keV were used for imaging. This system allows imaging at 50 nm spatial resolution. To achieve such high spatial resolution, the system is equipped with an ultra-stable vertical stage in which the degrees of freedom were reduced to a strict minimum. When mounted, the sample rotation was precisely controlled with low-runout, air-bearing rotary stages.

To fully utilize the advantages provided by the beamline facility, a smaller sample size (<60 μm) was prepared from the tape-cast PEO-LLZO films. Small triangular pieces were cut off from the films and glued on the tip of a metal pin with epoxy. The protruding tip of the sample was imaged. All samples were exposed to X-rays for one hour before imaging to stabilize the polymer and ceramic phases. 2D projections were then acquired by rotating the sample stage 360° with 300 ms of exposure time. The X-ray beam was focused on the sample using a pinhole and condenser upstream of the sample. X-rays transmitted through the sample are focused on the detector through a Fresnel zone plate and phase ring. A 2448x2048 pixel area detector was used that provided a field of view of 73.2 - 61.2 mm and a resolution of 50 nm was obtained after binning. A small triangular piece was cut off from the membrane and glued on the tip of a metal pin with epoxy. The protruding tip of the sample was imaged. All samples were exposed to X-rays for one hour before imaging to stabilize the polymer and ceramic phases. 1201 projections were collected over 360° rotation of the sample with an exposure time of 300 ms. The total run time for a single tomography scan was 26 minutes. Simultaneous Iterative Reconstruction Technique (SIRT) algorithm within the ASTRA toolbox was used for reconstructing the tomography data. 200 iterations of the algorithm were found to produce the best quality images and were used for all reconstructions. Subsequent image processing and segmentation routines were carried out in ImageJ.

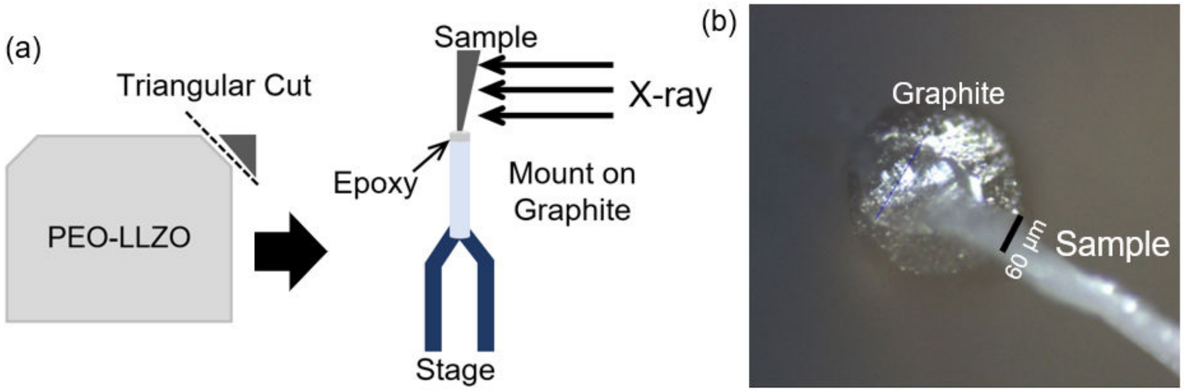

Figure 2.5: Schematic of the sample preparation of hybrid electrolytes. The samples were glued with epoxy on graphite and mounted on the stage.

Chapter 3

Percolation and Ion Transport in Hybrid Solid Electrolytes for Li-metal Batteries

3.1 Introduction

Solid state electrolytes that can suppress lithium dendrite growth are potential candidates for energy dense metallic lithium batteries (Janek & Zeier (2016b); Manthiram et al. (2017b); Shen et al. (2018a)). Currently, there are several solid electrolytes that exist and broadly fall into two material categories: (1) organic and (2) inorganic. Polymer electrolytes are advantageous because they can be manufactured easily into thin films, are mechanically robust, and flexibleMacFarlane et al. (1999); Kamaya et al. (2011). However, polymer electrolytes have lower ionic conductivity when compared with their ceramic counterpart. Ceramic conductors boast outstanding ionic conductivity ($\geq$10 mS/cm) but processing the electrolyte into thin films (50-100μm) for efficient device integration still remains a challenge because of the brittle nature of the ceramic (Li et al. (2015)). A hybrid approach which combines a polymer and ceramic into a composite electrolyte is one potential route toward achieving both efficient transport and processability in all solid state batteries(Croce et al. (1998); Zheng & Hu (2018); Zheng et al. (2016a); Chen et al. (2019)).

A hybrid or composite solid electrolyte is composed of an ion conducting organic polymer and an inorganic material (i.e. SiO_2, Al_2O_3, etc.). The addition of an 'inactive' inorganic (composite) (Scrosati (2001); Croce et al. (1998)) or ion conducting glass/ceramic (hybrid) (Zhang et al. (2018b)) increases the electrolyte's elastic modulus and critical current density (Gurevitch et al. (2013); Devaux et al. (2015); Villaluenga et al. (2016)). The role of the inorganic constituent on ionic transport is unresolved in hybrid electrolytes. Some reports suggest that the addition of an 'inactive' ceramic can increase the ionic conductivity of the electrolyte by four orders of magnitude (Croce et al. (1998); Scrosati (2001)). However, in water-free environments, and with different inorganic materials, this improvement is less obvious (Krawiec et al. (1995)) and can even decrease (Lu et al. (2012); Schaefer et al. (2011); Pandian et al. (2018)) with increasing inorganic loading.

Prior reports suggest that the the nature of lithium transport in composite systems is fundamentally related to constituent interactions (i.e. polymer|ceramic) (Chen et al. (2019); Croce et al. (1998); Stephan & Nahm (2006); Zheng & Hu (2018)). In composite electrolytes with inert fillers, the nature of surface interactions and confinement can dictate transport (Moreno et al. (2018); Dixit et al. (2018b)). Inorganic compounds that are acidic or neutral are more likely to form hydrogen bonding with the salt anions and the oxygen in the polyethylene oxide. This bonding, can potentially promote efficient salt dissociation and faster Li^+ ion transport (Croce et al. (1998)). Furthermore, the addition of an inert filler can control the crystallization kinetics of polyethylene oxide and enable a greater concentrations of highly conducting amorphous domains (Stephan & Nahm (2006)). However, if the polymer (ion conducting phase) is diluted too much with fillers (non ion conducting phase), these positive impacts are negated. At high filler content the dilution effect predominates and the ionic conductivity decreases. Thus, in composite electrolytes, optimal filler concentration between 8-20 vol% are reported (Croce et al. (1998); Stephan & Nahm (2006)).

While dilution theory explains the decrease in ionic conductivity at high filler loadings in composite electrolytes, it cannot completely explain the same trend observed in hybrid electrolytes. The fillers in hybrid electrolytes are active (i.e. ion conducting) and thus there should not be a decrease in ionic conductivity at high loadings. Furthermore, the inorganic ion conductor typically has a higher ionic conductivity than the polymer electrolyte (especially at low temperatures) and thus it is counterintuitive that more inorganic ion conductors would lead to decreased transport properties. The decrease in ionic conductivity at high inorganic content loading ($>$30 vol%) is often attributed to a formed interfacial resistance (R_{int}) at the polymer|ceramic interface which prevents transport between the two materials (Pandian et al. (2018); Chen et al. (2019); Tenhaeff et al. (2011)). Many reports suggest that this interfacial region is the dominant path for ion transport in a hybrid electrolyte due to the formation of a space charge layer (Li et al. (2019b)). Prior reports have used indirect techniques such as NMR, modeling, and electrochemical techniques to probe the origin of this surface-driven transport mechanism (Zheng et al. (2019); Wang et al. (2017)). Herein, we intend to directly evaluate this hypothesis via a detailed nano-structural analysis of hybrid solid electrolytes. Ultimately, the underlying structure of the inorganic phase within the polymer matrix is shown to be a significant descriptor for transport properties.

3.2 Materials Synthesis and Processing

3.2.1 Synthesis of LLZO

Lithium lanthanum zirconium oxide ($Li_{7.5}La_3Zr_2Al_{0.25}O_{12}$) or Al-LLZO was synthesized using a conventional solid-state approach. Stoichiometric ratio of LiOH (pre-dried at 200°C under vacuum for 6 hours), La_2O_3 (pre-dried at 1200°C for 12 hours), ZrO_2, and Al_2O_3 was dispersed in isopropanol and ball milled in a planetary ball mill (Fritsch, Pulverisette 7 premium line) at 500 RPM (4 hours). Milling cycles included 5 minutes of milling and 15 minutes of rest. Powders were calcined in alumina boat at 900°C for 10 hours. A second ball mill step (500 RPM) for 2 hours was carried out for size reduction.

3.2.2 Processing of Hybrid Electrolytes

A series hybrid electrolytes were prepared via adding Al-LLZO (5-50 vol%) to a solution of polyethylene oxide (PEO) and lithium perchlorate ($LiClO_4$) in acetonitrile. $LiClO_4$ was pre-dried at 80°C under vacuum. The molar ratio of ethylene oxide (EO) and Li^+ was 18:1. The composite ink was ball milled for an hour to ensure effective mixing. and further processed via tape-casting to produce free-standing films. The suspension was then tape casted on a Teflon substrate with specified film thickness and then dried in an argon filled glove box for 12 hours to remove the solvent. Free-standing PEO-LLZO films were then carefully peeled off from the substrate and stored inside a vacuum chamber. Films had an average thickness around 60-70 μm. Electrolytes contained 5 vol% (16.6 wt%), 10 vol% (29.6 wt%), 15 vol% (40.1 wt%), 25 vol% (55.9 wt%), or 50 vol% (79.1 wt%) of Al-LLZO. The LLZO:PEO-$LiClO_4$ composition was calculated assuming the density of PEO, $LiClO_4$ and LLZO were 1.21 gcm^{-3}, 2.42 gcm^{-3} and 5.2 gcm^{-3}, respectively.

3.3 Material Characterization

X-ray Diffraction: X-ray diffraction (XRD) on neat LLZO and PEO-LLZO electrolytes was carried on by using Rigaku Smart Lab (Cu Kα X-ray).The diffraction patterns were taken from 10°-60° with a step size of 0.01° (**Figure 1.1a**).

TGA:Thermal stability of the electrolytes was analyzed by thermogravitimetric analysis on Instrument Specialist's TGA-1000. Thermal degradation of the materials was carried out from 25° to 900°C at 20°C heating rate (**Figure 1.1b**).

Imaging: Scanning electron microscopy of LLZO was carried out in Zeiss Merilin SEM instrument. Optical images of the hybrid electrolytes were taken by using a confocal Raman microscope (Thermo Scientific DXR).

3.4 Synchrotron Nanotomography

The Synchrotron X-ray Nanotomography was carried out at beamline 32-ID-C of Advanced Photon Source, Argonne National Laboratory. Filtered monochromatic X-rays at 8 keV were used for imaging. The X-ray beam was focused on the sample using a pinhole and condenser upstream of the sample. X-rays transmitted through the sample are focused on the detector through a Fresnel zone plate and phase ring. A 2448 × 2048 pixel area detector was used that provided a field of view of 73.2 x 61.2 μm and a resolution of 50 nm was obtained after binning. A small triangular piece was cut off from the membrane and glued on the tip of a metal pin with epoxy. The protruding tip of the sample was imaged. All samples were exposed to X-rays for one hour prior to imaging to stabilize the polymer and ceramic phases. 1201 projections were collected over 180° rotation of the sample with an exposure time of 300 ms. The total run time for a single tomography scan was ≈6 minutes. Simultaneous Iterative Reconstruction Technique (SIRT) algorithm within the ASTRA toolbox was used for reconstructing the tomography data (Palenstijn et al. (2011); van Aarle et al. (2015); Gürsoy et al. (2014)). 200 iterations of the algorithm was found to produce the best quality images and was used for all reconstructions. Subsequent image processing and segmentation routines were carried out in ImageJ (Schneider et al. (2012)).

3.5 Measurements of Transport Properties

Total Li^+ ion transference number of PEO-LLZO membranes was carried out by using AC impedance and DC polarization method. After assembling the membranes in symmetric Li|PEO-LLZO|Li cells, a stepped voltage of 10mV was applied and the current was recorded as a function of time. The cells were thermally treated from 20°C to 90°C three times for a time period of 45 minutes before proceeding with the electrochemical analysis. Transference number t_{Li^+} was calculated by using Bruce-Evans equation.

$$t_{Li^+} = \frac{I_s(V - I_o R_o)}{I_o(V - I_s R_s)}, \tag{3.1}$$

where V is the applied voltage, I_0 is the initial current at the beginning of the chronoamperometry step and I_S is the steady state current. R_0 and R_s are the initial and steady state resistances extracted from electrochemical impedance spectroscopy.

Ionic conductivity was measured via directly casting the electrolyte on to copper foil blocking electrodes. All samples were hot pressed at 50°C for an hour prior to the measurement. Electrochemical impedance spectroscopy (1 MHZ and 100 mHz) was run on the samples for operating temperatures between 25°C to 70°C. Activation energy were estimated using the Arrhenius equation.

3.6 Continuum Percolation Model

A continuum percolation model was built to predict structure driven properties in hybrid solid electrolytes (Roman (1990); Bae et al. (2018)). This model is based on the heterogeneous distribution of inert fillers dispersed within a matrix where three components are present with different conductivity; insulating fillers, normally conducting dispersing medium and a highly conducting interface region. Al-LLZO has an order of magnitude higher ionic conductivity compared to the polymer matrix. However, the hybrid electrolytes do not exhibit conductivities similar to that of the ceramic particles even at very high loadings. Furthermore, the optimum value of solid loading is found at 15 vol.% which is relatively very small mass fraction of the system. Thus, an assumption of non-conducting filler particles has been made for the purpose of model development. The interfacial layer thickness and conductivity depends on particle size and volumetric loading (Dudney (1985)). The conductivity calculation is based on effective medium approximation (EMA), which gives a better accuracy in 3-dimensional cases like this. Here, a spherical random void model of dispersion is considered. The domain is a polymer matrix surrounding ion conducting particles with radius R. The three well-defined regions are: (1) the ceramic particle σ_{np}, (2) the bulk polymer σ_p, and (3) the interfacial layer σ_i. The interfacial layers is typically 2-3× the diameter of the particle and is represented by a thickness of λ (nm) in the proposed model. Considering an insulator-interphase model, we assume the grain boundary resistances are large, and thus ion conduction does not occur through the inorganic particle (i.e. σ_{np}=0) and that the interphase region is comparable to the size of the inorganic particles (i.e. 200 nm). The ratio between the inorganic particle and interfacial layer to the the inorganic layer is:

$$\eta = \frac{R + \lambda}{R}$$

and the the volume of the inorganic particles in a hybrid electrolyte is p:

$$V_{np} = p \tag{3.2}$$

The volumetric distribution of the polymer (V$_p$) and interphase region (V$_i$) can calculated by:

$$V_p = (1-p)^{\eta^d} \tag{3.3}$$

$$V_i = 1 - p - (1-p)^{\eta^d} \tag{3.4}$$

where d represents the model dimensions (d=3). The overall ionic conductivity for the hybrid electrolyte can be calculated:

$$\sigma = \frac{\sigma_p\left[-A + \sqrt{A^2 + 2\tau(z-2-zV_{np})}\right]}{z-2} \tag{3.5}$$

where,

$$A = \left[1 - \frac{zV_p}{2}\right] + \tau\left[1 - \frac{zV_i}{2}\right] \tag{3.6}$$

and

$$\tau = \frac{\sigma_i}{\sigma_p}$$

Where σ_p is the ionic conductivity of the organic phase taken as 2x10^{-6} S cm^{-1} and σ_i is the ionic conductivity of the interphase region taken as 1.5x10^{-5} S cm^{-1}. Here, z is the coordination number (55) which is approximated from the percolation threshold $p_c = (z-2)/z$ which is assumed to be 0.96 for nano Al-LLZO.

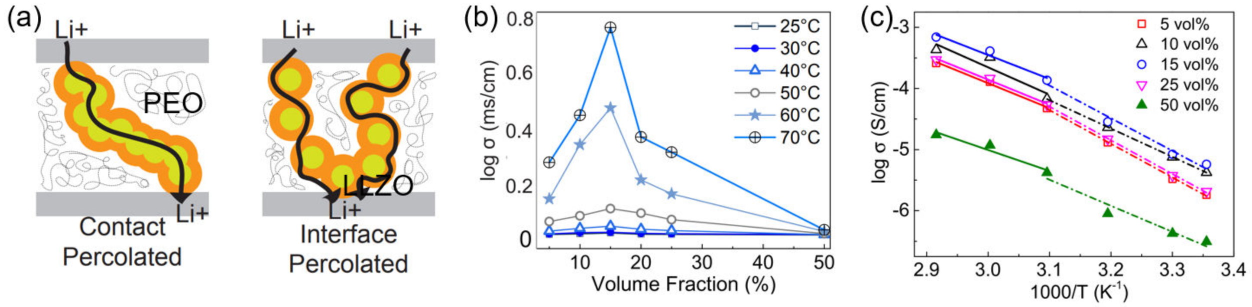

Figure 3.1: Schematic of percolation regimes that exist in hybrid electrolytes (a) and ionic conductivity measurements for hybrid electrolytes with varying concentrations of inorganic (LLZO) fillers (b). Ionic conductivity represented as a function of volume fraction to highlight temperature dependent optimum (c).

3.7 Results and Discussion

3.7.1 Transport Properties of hybrid electrolytes

There are two percolation thresholds that exist in hybrid solid electrolytes: (1) long-range connectivity of inorganic particles (contact mode) , and long-range connectivity of an interfacial layer (**Figure 3.1**) . The interfacial region describes the material properties of the polymer in direct contact with the inorganic particle (Al-LLZO). At the interface, a range of properties can be observed depending on chain orientation and confinement effects(Hamming et al. (2009); Sebastian & Jantunen (2010)). Thus, this layer displays properties that are neither characteristic of the bulk polymer nor the bulk inorganic particle. This region is estimated to extend 2-3× beyond the diameter of the inorganic particle (Qiao et al. (2011a); Tzika et al. (2000)). Contact percolation occurs at high loading of 33 vol% (ceramic:polymer) and the interfacial percolation can occur at ≈ 4 vol% (ceramic:polymer). However, these loadings are under the assumption that the particles are uniformly distributed with little or no agglomeration in the polymer matrix (i.e. electrolyte). Theoretically, if the highly conducting LLZO phase was fully percolated, lithium would transport through the inorganic material. However, in practice this does not occur and an order of magnitude decrease in ionic conductivity is observed when the inorganic content increases from 25 vol% (around percolation) to 50 vol% (above percolation) across all temperatures (25-70°C) (**Figure 3.1b**). Hybrid electrolytes that contain Al-LLZO concentrations around 5 and 25 vol% demonstrate similar behaviors in terms of ionic conductivity. Both electrolytes exhibit a conductivity around 2.0×10^{-6} Scm^{-1} at room temperature and about 3.0×10^{-4} Scm^{-1} at 70°C. The temperature dependent ionic conductivity (Arrhenius plot) is non-linear around the melting temperature for polyethylene oxide (60°C). This is due to the crystallization of polyethylene oxide below this point. The Arrhenius equation is employed to estimate the activation energy for each electrolyte.

$$\sigma = \sigma_0.e^{(-E_a/kT)} \tag{3.7}$$

where σ_0 is the pre-exponential factor, E_a is the activation energy, k is the Boltzmann constant (8.617×10^{-5} ev K^{-1}) and T is the temperature. Below 60°C the activation energy is $\geq$ 0.40 eV for all samples except the 50 vol% which is $\approx$ 0.37 eV. All hybrid electrolytes experience a decrease in the activation energy above the melting temperature of polyethylene oxide (Table 3.1).

Table 3.1: Activation energy and transference number for hybrid electrolytes

Ceramic vol%	$E_a(eV)(< T_g)$	$E_a(eV)(>T_g)$	TN
5	0.47	0.35	0.13±0.02
10	0.40	0.39	0.22±0.03
15	0.46	0.34	0.24±0.02
25	0.47	0.35	0.28±0.04
50	0.37	0.30	0.38±0.03

The Al-LLZO content significantly affects the transport properties in a hybrid electrolyte (**Figure 3.1c**). The polyethylene oxide region of the hybrid electrolyte contains both anions (ClO_4^-) and cations (Li^+) whereas the Al-LLZO region only carries charge via a lithium cation (i.e. single ion conductor)(Tominaga & Yamazaki (2014); Armand (1983b); Tominaga et al. (2015)). Thus, as the Al-LLZO concentration increases from 5 vol% to 50 vol% there is a subsequent increase in the transference number from 0.13 to 0.38 (Table 3.1). Addition of inorganic particles increases the Lewis acid type interactions as well as decreases the crystallinity of the polymer matrix. Lewis acid interactions between the chemical moieties on the inorganic particle surface and the anion and/or the polyethylene oxide restrict anion mobility as well as decrease Li^+ interactions with O in the PEO matrix (Croce et al. (1998)). Polymer matrix crystallinity also reduces as the solid loading is increased leading to an enhancement of the ion transport properties and effective salt dissociation (Aziz et al. (2018)). These factors lead to the increase in transference number of the hybrid electrolytes. The presence of LLZO in the PEO matrix is clearly distinguishable from XRD patterns (**Appendix A, Figure 1a**). As the ceramic loading gradually increases, intensity of the highly crystalline LLZO peaks susbtantially grows, suppressing the influence of polymer in the matrix.

The Al-LLZO content also influences the ionic conductivity. As the Al-LLZO is increased from 5 to 15 vol% there is an increase in ionic conductivity and then above 15 vol% the ionic conductivity decreases. This trend is more pronounced at high temperatures (70°C). Prior work suggests that the improved transport is related to a decrease in polymer crystallinity with the addition of a filler material (Aziz et al. (2018); Zheng & Hu (2018); Chen et al. (2019)). At high temperatures, above and around the melting point (T_m=60°C), the polymer will naturally reside in an amorphous form and thus the improved transport cannot completely be described by polymer structure. Thus, the results suggest that either the interfacial and the bulk properties of PEO matrix are responsible for the improved transport properties of the hybrid electrolytes.

It is challenging to probe the surface and bulk properties of the Al-LLZO particles because they are sub-surface and encapsulated in a polymer matrix. Typically, hybrid solid electrolytes are processed via the formation of a colloidal ink following by tape casting method (**Figure 3.2a**). Thus, electrolytes can be coated into thin films and are free standing for use (**Figure 3.2b,c**). During the preparation and processing of the colloidal ink, particles can aggregate and form a variety of structures (Hatzell et al. (2017); Dixit et al.

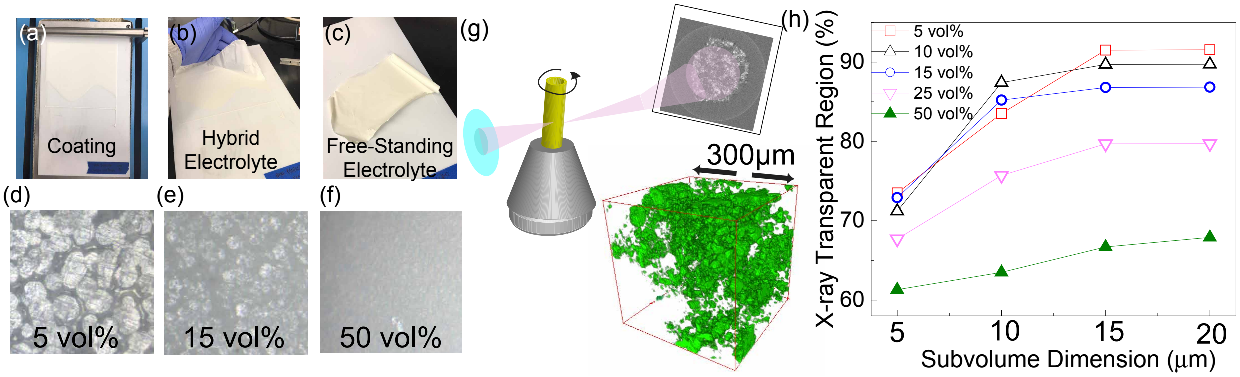

Figure 3.2: Hybrid electrolytes are typical solution processed (a) into free standing films of varying thickness (b,c). Optical images demonstrating the surface morphology of a hybrid electrolyte composed of (d) 5 vol%, (e) 15 vol% (f) 50 vol%. (g) A schematic of a how the inorganic microstructure can be extracted using synchrotron nano tomography. (h) A geometric analysis on 3-D reconstructions to determine best volume ($15\times15\times15$ μm^3) for quantitative analysis of reconstructed samples.

(2018a)). The abnormality in aggregation due to higher loading can affect the properties of PEO-LLZO as a composite. Morphological differences in PEO-LLZO surface can be seen clearly with optical microscopy. The electrolyte surface morphology differs depending on the composition. At low concentration (5 vol %) the morphology demonstrates some indication of phase separation and aggregation of the particles (**Figure 3.2d**). As the sample loading is increased from 15 vol% and 50 vol%, the electrolyte becomes opaque taking on the coloring of the Al-LLZO nanoparticles (**Figure 3.2e,f**). At these vol% loading, little to no insight into structural properties can be discerned with standard imaging techniques . It is challenging to discern the underlying microstructure using standard surface visualization techniques. Rigorous structural analysis of the hybrid electrolytes with varying inorganic content is necessary to discern whether the improved transport is related to the bulk or surface properties of the Al-LLZO nanoparticles.

3.7.2 Quantitative 3D mophological analysis using nano-tomography

Micro- and nano- X-ray computed tomography (XCT) is widely used to build a three dimensional understanding of a material's micro- and nano-structure. Technique resolution and quality is dependent on the specific optical set-up, but micro- computed tomography can achieve resolutions around 1μm and nano-computed tomography can achieve resolutions around 60-100 nm (at synchrotrons). The trade-off between the techniques is field of view and resolution. The synthesized inorganic Al-LLZO has an average particle size of 200-300 nm (**Figure 3.2e,f**) and thus falls outside the resolution limit of micro-tomography but is within the resolution limit of nano-computed tomography. The principle of nano-CT is demonstrated in Chapter 2. A series of 2D images are taken while the sample holder rotates from 0° to 360° (**Figure 3.2g**). The 2D images of the hybrid electrolytes demonstrate large attenuation contrast between the polymer and inorganic region (Al-LLZO). The polymer does not attenuate the x-rays and thus is transparent, leaving behind direct visualization of the Al-LLZO percolating networks (**Figure 3.2g**). These images are subsequently binarized for quantitative analysis. The fraction of X-ray transparent region in the sample is computed using the pore size distribution package of ImageJ. Spheres of different radii are fit in the binarized domain for the X-ray transparent phase (dark region of binarized image, (**Figure 3.3a**). The volume of the total spheres fit in the domain gives us the fraction of that phase while the size distribution of sphere radii give the dimensions of the X-ray transparent phase. This geometric analysis was completed on various sub-volumes from 5 to 20 μm^3 to identify a representative sub-volume for quantitative analysis (**Figure 3.2h**). Identification of a representative volume is essential for reliable quantification of results from tomography measurements (Dixit et al. (2018b)). Smaller sub-volumes can demonstrate anomalous local behavior that is not representative of the whole sample (**Appendix A, Figure 2a**). On the other hand, larger sub-volumes visually provide more perspectives. But this comes along with X-ray influenced artifact containing regions, which is also not suitable for analyzing the heterogeneity of the system (Vaselabadi et al. (2016)). Moreover, it is computationally intense to do analysis on large sub-volumes. X-Ray transparent region fraction reaches a plateau value for all the loadings imaged at 15 μm^3 sub-volume dimension. This dimension was used for all subsequent quantitative analysis (**Appendix A, Figure 2b**).

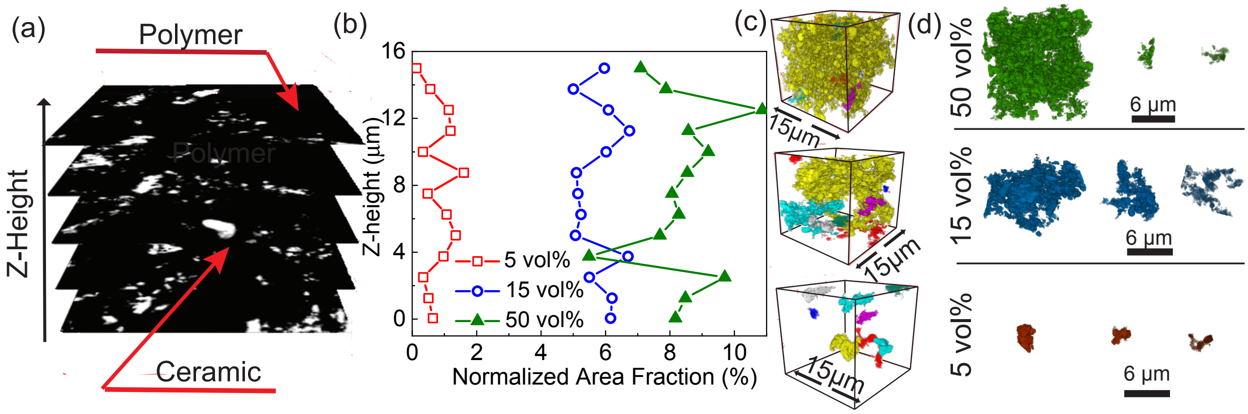

Figure 3.3: (a) Stack of binarized images demonstrate polymer and ceramic region in a hybrid electrolyte. (b) The normalized ceramic area at different cross-sections in hybrid electrolytes containing 5, 15, and 50 vol% Al-LLZO. (c) 10 largest percolated (aggregated) structures in a sub-volume for 5, 15, and 50 vol% Al-LLZO and (d) exploded view of top three aggregated structures in each electrolyte.

In order to discern whether the Al-LLZO nanoparticles's surface or bulk properties are responsible for the improved transport properties, we set out to quantify the accessible surface area of the inorganic materials within the polymer matrix. In theory, the accessible surface area should increase as the Al-LLZO nanoparticles decrease in size and increase in concentration in a hybrid electrolyte. However, if any aggregation occurs this surface area will become inaccessible. Aggregation can be clearly observed when looking at a stack of binarized 2D images of the 5 vol% electrolyte at different z-heights (Fig. (**Figure 3.3a**). In the binarized images, the black region signifies the polymer region and the white region is representative of LLZO. We observe significant structural (surface area) heterogeneity in the electrolyte as we work our way up the z-axis (**Figure 3.3b**). This figure demonstrates the ratio of the white area to black (i.e. ceramic to polymer) for each z-height in the sub-volume. As the Al-LLZO content increases from 5 vol% to 50 vol% there is a $\approx$ 3-10$\times$ increase in accessible interfacial area. However, it should be noted that within 15 to 50 vol% the area increases by $\approx$ 2% only. This contradicts the theoretical surface area estimation of this hybrid systems which show that surface area for mono-dispersed particles should increase by $\sim 3\times$ on increasing the loading from 15 % to 50 %. This clearly signifies that there is severe particle agglomeration at higher loading forming continuous clusters within the hybrid electrolytes. To assess the degree of aggregation, we sorted out 10 largest connected clusters for 5, 15 and 50 vol% (**Figure 3.3c**). These are identified by tracking individual voxel neighbours in a sub-volume. Voxels with 26 neighbouring voxels in identical phase are considered as a part of a single cluster. Agglomeration effects are evident in these images where the largest cluster (yellow) is seen to almost take up the entire domain for 50 % sample. To aid visualization, three largest clusters for these loading are imaged separately (**Figure 3.3d**). 5 vol% sample shows a uniform distribution of similar sized clusters. 15 vol% sample shows some degree of agglomeration as the cluster size is larger than those seen for 5 vol%. The three largest clusters are of similar size within the sample. However, for 50 vol% the largest cluster occupies the largest of the particle volume (324 μm^3), followed by clusters even smaller than what is for 5 vol% (Fig S3b). This is a direct evidence of agglomeration within the system which leads to a significant loss in accessible surface area of the particles. A complete reconstruction of the structural arrangement for different hybrid electrolytes from 5 to 50 vol% is shown in **Figure 3.4**.

Accessible particle surface area was quantified by calculating the particle surface area to volume ratio of all samples (**Figure 3.5b**). Surface area of the particles is estimated from the binarized images and normalized to the volume of particles in each sample. At low loading, the particle clusters are dispersed allowing complete access to the surface area. A large portion of the total particle surface area is lost as the Al-LLZO content is increased do the aggregation of the particles. The maximum normalized surface area is observed at 15 vol.% which is correlated to the highest ionic conductivity. This surface area relationships corroborates the proposed surface-driven transport hypothesis.

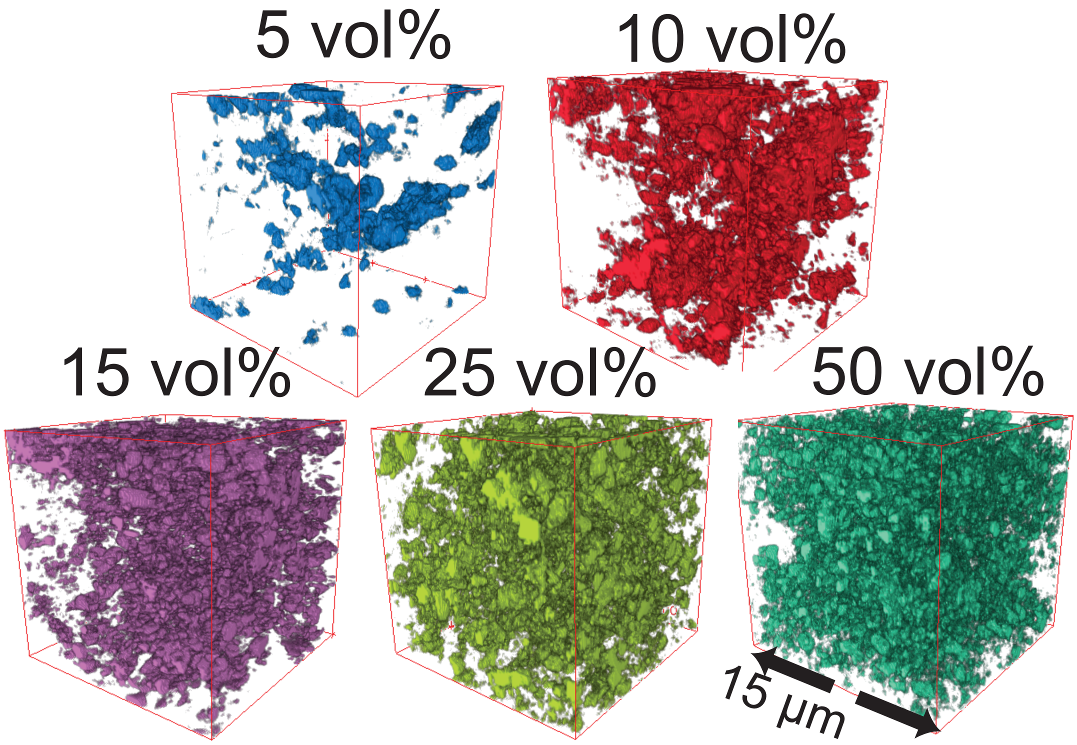

Figure 3.4: Reconstructed images for hybrid solid electrolytes of 5, 10, 15, 25 and 50 vol% loading of LLZO.

3.7.3 Percolation Model

The proposed surface-driven transport hypothesis is further corroborated via analysis of continuum percolation model. This model provides a simple yet reliable estimation of static interfacial properties that emerges from the interactions of nanoscale particles dispersed in polymer matrix. The formation of interphase due to particle-polymer interactions is expected to lead to a region with higher ionic conductivity than neat PEO (σ_p = 2x10^{-6} S.cm^{-1}). Although the interphase thickness λ is influenced by particle loading, especially at higher volume fraction where overlapping interfaces are likely, it is appropriate to assume the thickness to be 2-3 times larger than the particle size (Qiao et al. (2011b)).

Figure 3.5 shows the relationship between Al-LLZO volume fraction (p) and ionic conductivity and accessible surface area. The model (dashed line) matches the experimentally (squares) measured surface areas at low volume fractions fairly well but deviates significantly above 20 vol% (**Figure 3.5b**). The percolation theory assumes a uniform distribution of particles, where in reality agglomeration sets in at even low vol%. Thus, due to agglomeration, the degree of percolation is reduced as well as the accessible surface area.

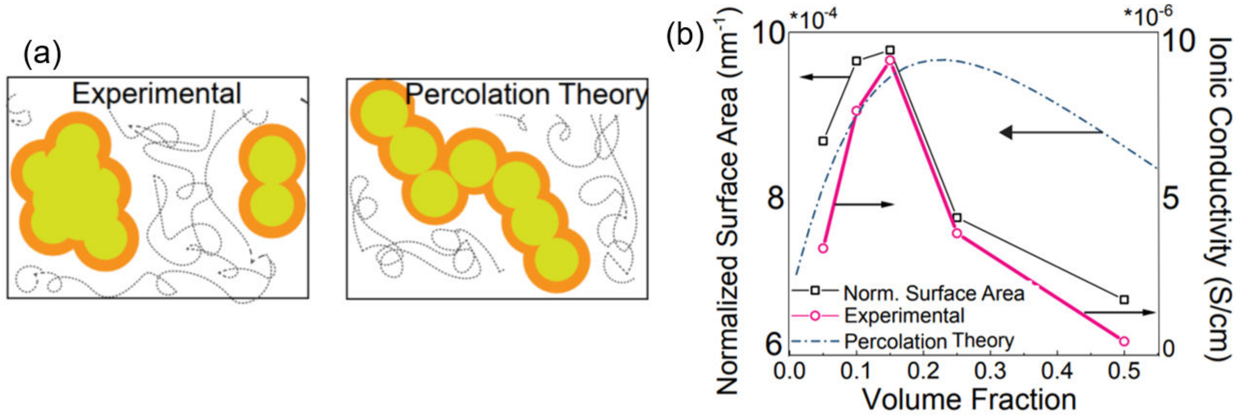

Figure 3.5: (a) Schematic of the difference between theoretical (percolation theory) and experimentally observed percolation of particles. (b) Ionic conductivity of hybrid electrolytes (measured both experimentally and theoretically) and normalized surface area (measured from nano-CT image analysis) of hybrid electrolytes.

3.8 Conclusions

Hybrid solid electrolytes combine a polymer ion conductor with an inorganic ion conductor in order to produce thin, flexible, and mechanically strong electrolytes for all solid state batteries. The addition of the secondary ion conducting phase (inorganic Al-LLZO) leads to enhanced transport performance at a composition of 15 vol% Al-LLZO. While there is a significant body of literature that ascribes this improvement to a decrease in the crystallinty in the polymer phase, this does not account for the enhanced performance seen above the melting temperature (T_m=65°C). Herein, we show that this enhancement is not a result of the bulk properties of the Al-LLZO, but instead is attributed to the polymer|particle interaction. Nano-computed tomography is a effective tool for probing structural properties in hybrid electrolytes and reveals a direct relationship between inorganic accessible surface area and ionic conductivity. Furthermore, the increase in transference number at high Al-LLZO content (and low ion conductivity) suggests that the Al-LLZO may form hydrogen bonding with the mobile anion, thereby limiting its charge-carrying ability. Future electrolyte designs and processing techniques that enable uniform particle distribution could enable highly conducting hybrid electrolytes.

The chapter sections are published in modified forms as:

W. Zaman, N. Hortance, M. Dixit, V. De Andrade, K.B. Hatzell, "Visualizing percolation and ion transport in hybrid solid electrolytes for Li–metal batteries", Journal of Materials Chemistry A, 2019, 7, 23914.

Chapter 4

Creep Effect and Interfacial Dynamics in Garnet-based Solid-state Li Metal Batteries

4.1 Introduction

Li-ion batteries hold great promise to enable high energy density energy storage systems for the electrification of transportation. Current LIB technologies employ graphite (360 mAh/g) as the anode. Replacing graphite with a Lithium metal (3860 mAh.g^{-1}) is recently of high interest for boosting the gravimetric and volumetric energy densities (Randau et al. (2020)). Li metal has the lowest reduction potential (-3.04 V vs SHE) and therefore, is prone to severe side reactions in conventional batteries, which is filled with liquid electrolyte (Cheng et al. (2017); Wood et al. (2017); Hatzell et al. (2020)). This leads to the formation of unstable solid electrolyte interphase (SEI) regions, uncontrolled Li electrodeposition, 'dead' Li accumulation and dendrite formations (Zou et al. (2021); Bai et al. (2016); Chen et al. (2017b)).

All-solid-state batteries (SSBs) are the most promising alternatives which employ robust solid ion conductors with a wide electrochemical window that can potentially mitigate these chemomechanical challenges associated with Li metal (Janek & Zeier (2016a)). Although the high elastic modulus of a solid electrolyte (SE) is expected to suppress Li dendrites, various experimental works have shown that Li filament propagates through the electrolytes, followed by crack formation (Kazyak et al. (2020a); Dixit et al. (2020a); Schlenker et al. (2020)). These unwanted phenomena are mostly attributed to poor interfacial properties of Li|SE, which severely affect the charge transfer kinetics and limit the practical implementation of solid-state batteries (Lewis et al. (2022)). In general, two types of interfacial limitations exist at this anodic interface. The first one attributes to the chemical instability of various solid electrolytes (e.g.; sulfides) against Li metal. The growth of interfacial reaction zones with several decomposition products can originate on the SE surface from contacting with Li metal (Wenzel et al. (2015a, 2016)). The second limitation attributes to the dynamic loss of interfacial contact points between Li and SE during the stripping (discharging) process (Kasemchainan et al. (2019); Wang et al. (2019c)). The dynamic morphological instability of Li metal generally stems from vacancy infusions during anodic dissolution. As a result, a large volume change takes place within Li during stripping. This triggers interfacial void formations and drastically increases the local current densities by 10-100 times (Dixit et al. (2020b)). These voids act as a barrier to fast Li diffusion during plating and can prompt cell failure by expanding over time (Seitzman et al. (2018); Lewis et al. (2021)). Strain-dependent deformation and diffusional properties of Li metal, both at bulk scale and nanoscale, have a significant influence on void growth against a rigid solid surface. In addition, solid electrolytes are often filled with numerous nano/micron-scale surface defect points, which causes non-conformal contact distributions with Li metal (Porz et al. (2017)). During plating, Li deposits on the confined defect zones which leads to higher local stress points that initiate cracks (LePage et al. (2019)). The stress accumulation is further exacerbated with increasing current density which causes dendrite-induced shorting and subsequent mechanical fracture of solid electrolytes (Shen et al. (2018b); Dixit et al. (2020a); Hao et al. (2021)). Therefore, voidless stripping and controlled plating of Li metal are two essential conditions for stable solid-state Li-metal battery operation.

Increasing the stack pressure on a solid-state battery can increase the electrode-electrolyte contact area, decrease interfacial resistance and ensure void mitigation over cycling (Hänsel & Kundu (2021); Zhang et al. (2020)). Both computational and experimental works have recently shown that there is a critical stack pressure required for maintaining conformal contacts between Li|SE interfaces (Doux et al. (2020a); Wang et al. (2019c)). This also holds true for aqueous Li-ion batteries (<500 KPa), but solid-state batteries generally require higher stack pressure (1-100 MPa) (Tan et al. (2020b)). The optimum stack pressure depends on the type of solid electrolytes used. For example, garnet oxide electrolytes like $Li_7La_3Zr_2O_{12}$ (LLZO) require a critical stack pressure of 3.4 MPa but are prone to mechanical fracture over 50 MPa. Sulfide electrolytes are softer and can withstand higher pressure (>100 MPa), but Li metal is prone to extrude through the electrolyte (Doux et al. (2020a,b)). Within the optimum range, the creep behavior of Li metal is the most dominant factor in maintaining interfacial contact properties (Zhang et al. (2020)). Li metal is viscoelastic with high volumetric strain and hence, stack pressure can enable Li to creep fast under dynamic conditions (LePage et al. (2019)). This can effectively suppress voids, regulate Li dissolution kinetics and prevent plating-induced dendrites. But at higher current densities, the electro-chemomechanical behavior of Li metal significantly changes to form large vacancy accumulated regions. Hence, stress-assisted creep has to compete to annihilate the pores and prevent contact loss. The dynamic property of creep against current density significantly impacts Li stripping morphologies and subsequent cell shorting. It is highly important to consider the consequence of such phenomena under practically relevant operating conditions where a higher amount of charge (>4 mAh/cm^2) is transferred at each cycle (Lewis et al. (2022)).

In this work, we studied the creep-induced interfacial aspects of Lithium metal and garnet LLZO solid electrolytes that impact the high-capacity stripping/plating (5 mAh/cm^2) of Li. Due to its intrinsic chemical stability against Li metal, LLZO is an excellent model system to evaluate the chemomechanics of Li metal. Prior reports showed that LLZO forms insulating surface carbonates (Li_2CO_3) in the air which decreases its lithiophilicity. In this work, an O_2-assisted processing approach was employed to prepare carbonate-free LLZO which is readily wetted by Li metal upon contact Krauskopf et al. (2019c). After applying stack pressure and subsequent melting of Li, a conformal contact of <5 Ωcm^2 can be achieved. We showed that the interfacial surface roughness (Li and LLZO), capacity, and current density significantly affect the morphological stability of Li during stripping, which indicates an enhanced void growth due to vacancy accumulation. We demonstrated that stack pressure is an effective method to enable stripping at high current densities due to the high creep rate. Combining pressure and temperature can significantly improve the chemo-mechanics of Li to enable stable and long-term cycling. This was further demonstrated on full cell configurations.

4.2 Materials Synthesis and Processing

4.2.1 LLZO Solid Electrolyte

Ta-doped $Li_7La_3Zr_2O_{12}$ solid electrolyte was prepared by ball milling the precursors LiOH (pre-dried at 200°C for 6 hours), La_2O_3 (pre-dried at 900°C for 10 hours), ZrO_2 and Ta_2O_5 in stoichiometric ratio. Anhydrous isopropanol was used as a milling solvent. The ball milling was carried out in Pulverisette premium for 4 hours at a rotation speed of 500 rpm. The mixer was then dried under air for solvent evaporation and collected via sieving. The precursor powder was annealed at 900°C for 8 hours under air. Another round ball milling was carried out to reduce the particle size (350 rpm, for 2 hours). The powder was then pelletized by using a pellet die under 300 MPa for 15 minutes. For the symmetric and full cell studies, a pellet die of 10 mm dia was used. For the 3-electrode setup, a pellet die of 20 mm dia was used. The pellets were then covered with additional LLZO (mother powder) and sintered under O_2 flow at 1235°C for 8 hours. After sintering, the pellets were cleaned and wet-polished with sandpapers to ensure a smooth surface. The final pellets have a relative density of 95-96% and thickness of around 1.5 μm. After polishing, the pellets were immediately transferred to an Ar-filled glove box to avoid Li_2CO_3 growth on the surface.

4.2.2 Cell Assembly

To assemble Li on LLZO, thin Li foil of 4 mm dia was punched and attached to the LLZO surface at 2 MPa. The copper foil was pressed on the top of Li foil as the current collector. To ensure negligible interfacial contact, the Li-LLZO assembly was heated up to 250°C for 30 minutes. The symmetric cells are cycled in a modified pressure cell setup. In addition, a 3-electrode setup was built to isolate the anodic (stripping) and cathodic (plating) interfaces of symmetric cells. Full cells were prepared by employing composite $LiFePO_4$ (LFP) cathode on Li-LLZO half cell. The composite cathode was prepared from a slurry comprised of LFP, conducting carbon (super P), PVDF binder, and LiTFSi salt with a weight ratio of 55:10:10:25. N-Methyl-2-pyrrolidone (NMP) was used as the solvent. The wet slurry was cast on a Carbon coated Aluminum foil and dried at 100°C for 24 hours to remove the solvent. Cathode discs (4 mm dia) were punched from the dry film and attached to LLZO by applying 10 MPa of pressure. Both symmetric and full cell assemblies were then placed inside a modified pressure cell setup where stack pressure was implied with the aid of a compressing jig. The setup consists of a cell chamber (material: PEEK) and two stainless steel plungers. A compression load cell (Omega Engineering) was used to monitor the stack pressure. To avoid cell relaxation over time, a stainless-steel spring was attached to the compression jig. For the 3-electrode cell, a small Li metal disc (2 mm dia) was used as the reference electrode. The Li disc was attached to a copper rod and inserted into the PEEK chamber. The reference electrode Li foil was manually attached to LLZO.

4.3 Electrochemical Measurements

Potentiostatic electrochemical impedance spectroscopy (PEIS) was carried out using Biologic SP300 (maximum frequency 7 MHz) and VMP3 (maximum frequency 1 MHz) potentiostats. The lowest frequencies for symmetric and full cells were 1 Hz and 100 mHz respectively, with an amplitude of 50 mV. EIS was also carried out to measure the ionic conductivity of sintered LLZO pellets. The acquired impedance spectra were fitted using RelaxIS software. Cycling profiles of symmetric and full cells were conducted under a galvanostatic current. Full cells with LFP cathode were cycled between 2.5 - 4V. Cyclic voltammetry (CV) measurements were carried out on full cells with a scan rate of 0.1 mV/s.

4.4 Characterization

X-ray diffraction: X-ray diffraction (XRD) was carried out on LLZO powders and pellets in Rigaku Smart Lab (Cu Kα X-ray).The diffraction patterns were taken from 10°-50° with 0.01° step size.

Surface Profiling of LLZO: Surface mapping of LLZO was carried out on a laser scanning confocal microscope (Olympus OLS5000) with a 50x objective lens. The resulting resolution is 0.25 μm in the x and y directions and 0.0008 μm in the z direction. Two images were taken of each sample surface. To obtain comprehensive images, data from 9 scans were stitched together to construct each image. This process resulted in a total measurement area of 715 by 715 μm per image. The data from the surface mapping was saved and analyzed in two ways. First, line profiles of surface roughness were examined with the instrument's software package to get an initial understanding of the surface topography. This data was exported as a report file. Second, the height data from the image was saved as .csv files. This allows for a more detailed topography analysis.

4.5 Computational Modeling

A three-dimensional (3D) contact model is generated here to simulate the interface evolution of the Li-LLZO due to the pressurized creep using an experiment-simulation interactive method, considering the LLZO rough surface, Li deformation, and Li creep (Zhang et al. (2020, 2019); Zhao et al. (2022)). A representative computational domain of 400μm×400μm is selected for contact analysis.

The contact conditions are:

$$\int_{\Gamma} p(x,y)d\Gamma = P.A_{geo\_Li} \tag{4.1}$$

$$p(x,y) > 0,\ gap(x,y) > 0; (x,y)\ \epsilon\ \Gamma$$

$$p(x,y) > 0,\ gap(x,y) > 0; (x,y)\ \epsilon\ \Gamma \tag{4.2}$$

$$gap(x,y) = -u_z(x,y,0) + h_{LLZO}(x,y) - h_{Li-creep}(x,y) - \delta_r \tag{4.3}$$

Where p(x,y) = normal pressure distribution on the Li surface, Γ = contact region, P = average stack pressure, A_{geo_Li} = geometric area of the Li surface, gap (x,y) = interfacial gap between Li and LLZO, u_z = normal elastoplastic deformation of Li, h_{LLZO} = rough surface height of LLZO, $h_{Li-creep}$ (x,y) = height reduction due to Li creep and δ_r is the rigid-body approach. The conjugate gradient method (CGM) and the continuous convolution-fast Fourier transform CC-FFT algorithm are used to solve the contact problem in Equation (1-3) (Liu et al. (2000); Liu & Wang (2002)).

4.5.0.1 Area-specific Resistance Calculation

$$R_{int} = \frac{ASR}{A_c} \tag{4.4}$$

where ASR is the area-specific resistance of the interface between SE and the Li, which is related to the property of a specified interface. For a clean LLZO-Li interface prepared by melting Li on LLZO, ASR may be very small. Two issues may affect ASR, surface contamination and roughness influence the full coverage of Li on LLZO. For the problem considered here, the roughness effect is a major concern. A_c is the projected contact area considering that the LLZO surface is relatively smooth (Han et al. (2017)). The ASR can be determined based on the evolution of interfacial resistance and contact area during creep. The surface roughness of LLZO in this study is about R_q=0.8 μm **(Appendix B, Figure 15)**. while the roughness of Li is ignored. Based on the material parameters (elastic modulus, Poisson's ratio, yield strength) (Table 1) and the experimental data, the ASR value for the present interface can be obtained as 15 ± 0.5 Ωcm^2. The contact area maps are shown in **(Appendix B, Figure 16)**.

4.5.0.2 Li creep

The indentation rate, $\dot{\epsilon}_{i\_creep}$ for Li creep law can be expressed as follows

$$\dot{\epsilon}_{i\_creep}(x,y) = \frac{\dot{h}_{i\_creep}(x,y)}{u_{Li}(x,y)} \tag{4.5}$$

where u$_{Li}$ (x,y) is the Li displacement. $\dot{\epsilon}_{i\_creep}$ is zero in the non-contact regions. $\dot{h}_{i\_creep}$ is the height-reduction rate due to Li creep, which can be determined based on the experimental data on pressure loading and prior works (Zhang et al. (2020); LePage et al. (2019); Masias et al. (2019)),

$$\dot{h}_{i\_creep}(x,y) = 0.128\ C_r \left[\frac{0.7982\ p(x,y)}{\sigma_Y}\right]^{6.6} exp\left(\frac{-Q_c}{RT}\right) .u_{Li}(x,y) \tag{4.6}$$

where C$_r$ is a material constant, Q$_c$ is the creep activation energy, R is the gas constant, and m is the stress exponent at T = 298K. Note that the values of m and C$_r$exp(-Q$_c$/RT) are influenced by the thickness of the Li metal used in the test (Haslam et al. (2022); Dienemann et al. (2021)). The experimental data in the present work resulted in m = 12 and C$_r$exp(-Q$_c$/RT) = 4.5 × 10^{-8} MPa^{-12}s^{-1}.

4.6 Results and Discussion

4.6.0.1 Adhesion of Li metal on LLZO

Interfacial resistance (R$_{int}$) is a common descriptor for the contact area estimation of Li and LLZO. There is a wide range of factors that dictate the interfacial resistance of Li|LLZO. Synthesis and processing of LLZO are typically conducted in an open environment which results in the formation of an insulating Li_2CO_3 and LiOH layer on the LLZO surface. Hence, we adopted an O_2-assisted sintering approach for producing carbonate-free LLZO pellets which shows an increased lithiophilicity and does not require any additional interlayers to get low contact resistance (Krauskopf et al. (2019c)). Surface contamination of Li also affects its interfacial compatibility with solid electrolyte Zheng et al. (2020). Introducing a thin metallic (Au, In) or metal oxide (Al_2O_3, ZnO) interlayer is a common approach to increase the Li wettability on LLZO and provides conformal contact (Sharafi et al. (2016); Han et al. (2017)). However, these alloys or interlayer-based approaches are not ideal for probing on pure interfaces. Li|LLZO interface exhibits a significantly low charge-transfer resistance (0.1 Ωcm^2) at room temperature and is chemically stable (Krauskopf et al. (2020a)). Therefore, charge transfer is not the rate-limiting step and the high interfacial resistance can be directly attributed to the true interfacial contact area (A_T). Here we observed that "lithiophilic" LLZO exhibits improved adhesion properties for Li metal. Upon contact, a lower value of A_T can be achieved by simply adding 10 MPa of stack pressure. However, surface inhomogeneities can also prevent LLZO from achieving proper interfacial contact with Li metal. The inhomogeneities stem from the non-uniform growth of LLZO grains. These lead to the formation of surface defects that are preferred hotspots for Li nucleation (plating) or void formation (stripping) **(Appendix B, Figure 2)** (Sharafi et al. (2017b)). Even after smooth polishing, the surface roughness of 2-7 μm is observed with multiple asperities **(Appendix B Figure 5)**. Such defect points also contribute to generating nano/micro-scale interfacial gaps.

Here, we investigated the adhesion of Li-LLZO with respect to stack pressure (1-70 MPa) at room temperature. Stepwise EIS measurements **(Appendix B, Figure 3a)** showed that the interfacial resistance decreases from 610 Ωcm^2 to 90 Ωcm^2 **(Appendix B, Figure 3b)**. The interfacial resistance was calculated by fitting the EIS spectra with an equivalent circuit of 1 resistive element (R_{bulk}) and 2 resistive-capacitive (RC) elements for grain boundaries (R_{GB}) and interfaces (R_{int}) **(Appendix B, Figure 3c)**. Stack pressure enables Li to creep and allows Li to deform on LLZO due to its high viscoelasticity. From a mechanistic perspective, Li creep drastically reduces the dislocation density and diffusion barriers between Li vacancies and adatoms (Yan et al. (2022)). At high stack pressure, larger dislocations result in a higher flux of adatoms towards the interfacial regions which fills up the meso/microscale voids. Stack pressure thus is an effective means to improve the overall contact resistance of Li and LLZO. However, we also observed that the aspect ratio of Li foil (especially at high stack pressure) changed significantly, displayed by the leftward shift of high-frequency EIS data points **(Appendix B, Figure 3b)**. This indicates shear deformation of Li which increases at higher compressive stress (Hänsel & Kundu (2021)). This can potentially lead to misinterpreting the actual interfacial resistance in Ωcm^2 as the electrode|electrolyte contact area increases. A minor improvement of interfacial contact was observed at high stack pressure (>70 MPa). Previous studies highlighted the need for an extremely high pressure (300 MPa) to achieve ≈ 0 Ωcm^2 of R_{int} (Krauskopf et al. (2019c)). However, LLZO is found to be broken above 80 MPa, which indicates that there is an optimum stack pressure required for LLZO to enable safe operation. Instead, we adopted a heat-treatment approach for ultra-low contact resistance ($\approx 2-3\Omega cm^2$) **(Appendix B, Figure 4)**. Melting of Li improved the local contact points due to a higher degree of Li diffusion. Compared to the values reported in various reports where interlayers were added for contact improvement, this approach demonstrated a simple, yet effective way to increase the surface adhesion of Li (Luo et al. (2016); Shao et al. (2018); Huo et al. (2020); Han et al. (2017)). We employed this adhesion strategy to generate different Li|LLZO interfaces to understand their dynamic nature under non-equilibrium conditions.

4.6.1 Effect of Initial Contact Resistance

The initial interfacial resistance R_{int} (or contact resistance) of Li|LLZO generally depends on two critical parameters: surface contamination of Li and LLZO and the presence of Kirkendall voids (Wang et al. (2019c)). As the LLZO pellets were prepared under O_2, we can assume that the R_{int} of the as-assembled cells originates from the presence of voids at local interfacial regions. Due to its low melting point (180°C) and high homologous temperature (T_H=66), Li metal exhibits creep-induced deformation under stack pressure

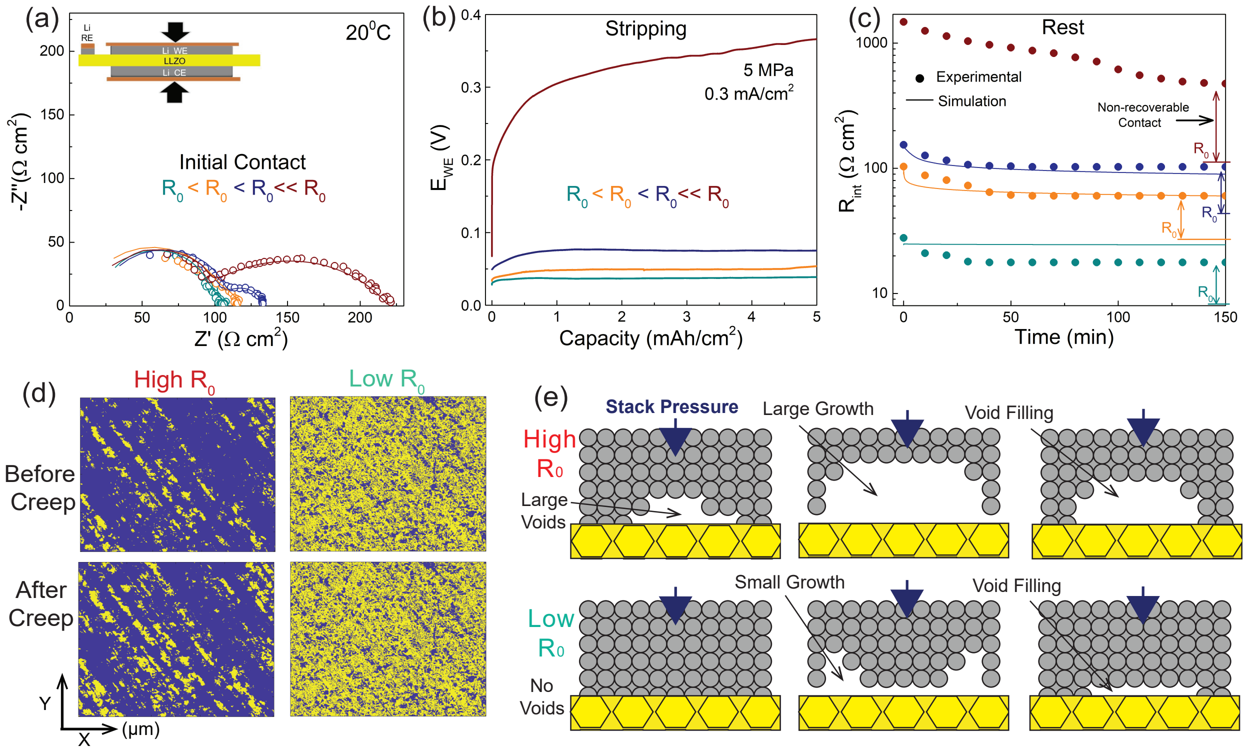

Figure 4.1: In a 3-electrode setup, (a) Nyquist plots showing the interfacial resistance of the working electrode (stripping) for four different symmetric cells. (b) Stripping profiles of the symmetric cells and (c) change in interfacial resistances due to Li creep. (d) Contact area (Li coverage on LLZO) evolution due to Li creep after stripping. (e) Schematic of void formation and creep-induced recovery of Li|LLZO interface.

and can potentially eliminate the voids. The deformation is considered purely plastic and driven by the dislocation glide of Li from the bulk region to the interface. To avoid high creep-induced strain, we employed Li foils of only ≈80-100 μm of thickness which undergo only <3% of strain at 15 MPa (Haslam et al. (2022)). Due to its highly adhesive nature, Li forms permanent contact with LLZO which remains intact even after removing the pressure. However, under anodic load (stripping), continuous depletion of Li causes an increase in surface roughness and loss of contact points which generates voids at the interfacial regions (Kasemchainan et al. (2019)). The bulk Li also experiences morphological changes due to the increased number of vacancies (Dixit et al. (2020b)). These phenomena exacerbate at higher current densities which leaves numerous hotspots for dendrite formations. Both theoretical and experimental studies suggested that Li creep is the most dominant mechanism for the void annihilation and re-stabilization of the interfaces (Krauskopf et al. (2020b); Zhang et al. (2020)). We observed a correlation between initial R_{int} and creep (**Figure 4.1a**) and creep (**Figure 4.1c**). By employing a 3-electrode setup, four different interfaces (R_0 = 2, 13, 30 and 120 Ωcm^2) were investigated to observe the stripping profile at 0.3 mA/cm^2. The stack pressure was kept at 5 MPa and 5 mAh/cm^2 of Li (thickness $\approx 25\mu$m) was stripped. The cell with R_0 of 120 Ωcm2 displayed a high degree of polarization (>300mV) after the Li dissolution process, whereas cell with R_0 of 2 Ωcm^2 showed only 10 mV of increment (**Figure 4.1b**). The cells were then rested for over 2 hours, during which EIS was conducted intermittently. A stronger creep effect was visible for cells with high R_0. During the resting period, pure Li creep improved the interfacial contact by filling up the voids (from 1600 to 500 Ωcm^2). Creep effect was minimal for cells with cell with smaller R_0 and almost negligible for R_0 of 2 Ωcm^2 (**Figure 4.1c**).

This result demonstrated the effect of pre-existing interfacial voids which dictates further void growth during the stripping process. In general, when the Li flux due to migration ($\mathbf{J}_{migration}$) is taken away from the interface to the solid electrolyte, the diffusion-controlled Li flux ($\mathbf{J}_{diffusion}$) fills up the vacancies and keeps the interface morphologically stable. This is mostly observed during low current density stripping (<0.05 mA/cm^2). However, at a high current density (>0.1 mA/cm^2), diffusion can not completely impede void growth. Applying stack pressure allows creep-induced flux enhancement at the interface ($\mathbf{J}_{creep}$), which can effectively annihilate the pore formations. When R_0 is negligible, the Li|LLZO interface can be considered as flat (ideal) (**Figure 4.1e**). Here, $\mathbf{J}_{diffusion}$ can successfully restrict larger void growth with minimal help from $\mathbf{J}_{creep}$ during stripping. When R_0 is significantly higher, Li|LLZO interface is not flat due to the presence of many pre-existing voids. In this case, the self-diffusion property of Li is impeded due to the voids, and $\mathbf{J}_{creep}$ plays a more prominent role in reducing the vacancies(LePage et al. (2019)). However, the pre-existing voids continuously expand and overlap with each other upon

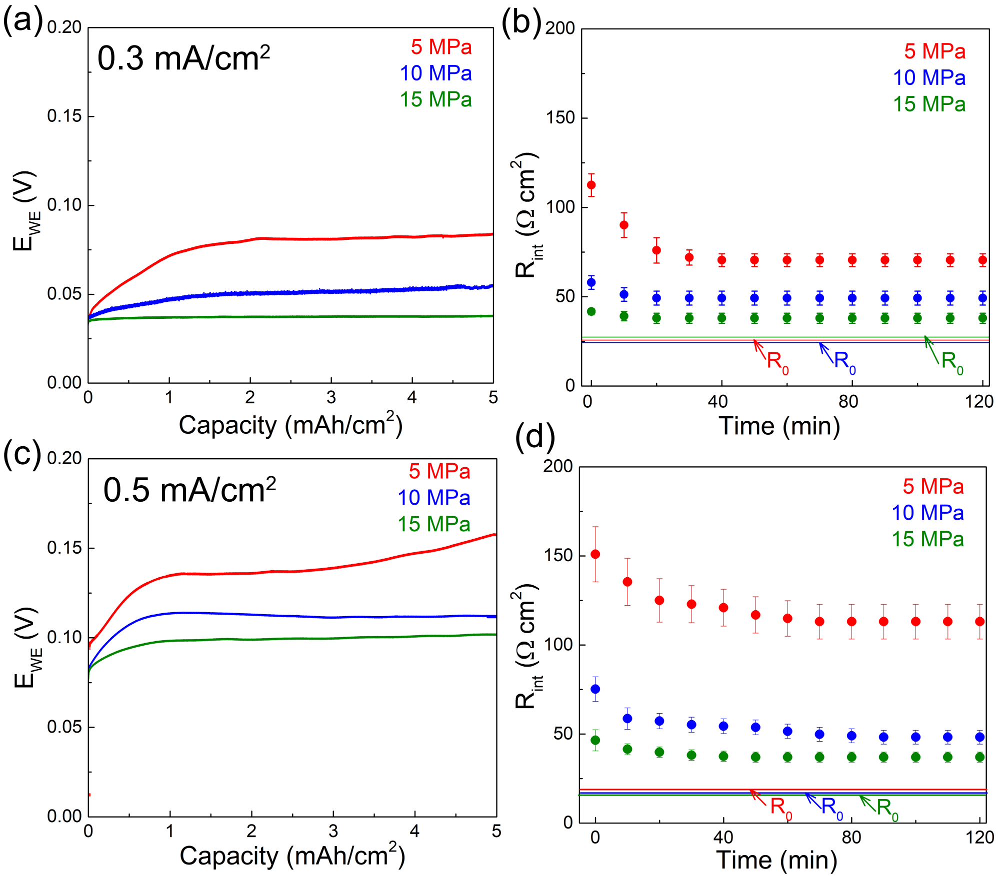

Figure 4.2: In 3-electrode system, (a,c) voltage profiles of the working electrode at current density of 0.3 and 0.5 mA/cm^2. (b,d) Corresponding change in interfacial resistances over time due to Li creep after stripping.

expansion which gives a significant rise in polarization.

4.6.2 Effect of Stack Pressure during Li Cycling and Subsequent Creep

To investigate the dynamics of Li dissolution and evolution of the interface, we carried out long-term Li stripping at 3 different stack pressures (5, 10 and 15 MPa) (**Figure 4.2**). We employed the 3-electrode system for this experiment where a total of 5 mAh/cm^2 of Li was stripped in each case to allow more void growth over time. Here, we observed a strong stack pressure dependence on void growth and the long-term stripping behavior of Li. Voiding is significant when stripping high capacities of lithium. At 5 MPa, we observed a higher overpotential with stripping capacity while at high pressures (e.g.; 15

MPa) the overpotential shows little change (**Figure 4.2a**). When the current density was increased to 0.3 to 0.5 mA/cm^2, a higher degree of polarization was observed as the rate of void formation increased (**Figure 4.2c**). The voiding was highly suppressed in both cases when the stack pressure was 15 MPa. The voltage profiles show an almost linear profile for 5 mAh/cm^2 of Li stripping, which indicates that higher stack pressure can successfully impede the void growth and enable a balanced stripping process. However, a common trend for higher polarization at the initial stage of stripping (<1 mA/cm^2 of Li capacity) was observed for all cases. This suggests that Li undergoes a drastic volume change at the beginning phase of the stripping process, followed by a steady/slow volume change. The initial voiding is more visible at 5 MPa where low stack pressure initiates low creep and allows higher dynamic volume change of Li. As the migration flux of Li increases with current density, high stack pressure is required to enable more Li to creep to fill the voids.

After the completion of stripping, EIS during the resting period showed a gradual decrease in R$_{int}$ due to pure Li creep. Creep-induced R$_{int}$ improvement was more prominent at low stack pressure (5 MPa) measurements. The role of creep was faster at the initial stage and the contact improvement was stabilized within 30-60 minutes (**Figure 4.2b**). Similar effect was also seen for cells stripped at 0.5 mA/cm^2 (**Figure 4.2d**). It should be noted that the stack pressure and subsequent creep after stripping could not entirely recover the overall contact loss (**Figure 4.2b,d**). This signifies that a region of non-recoverable void exists which cannot be replenished by Li creep only. Several possible mechanisms can drive the formation of this "non-recoverable" zone. First, LLZO is relatively a stiffer solid electrolyte than sulfides or polymers, which exhibits a significantly higher shear (60 GPa) and elastic modulus (150 GPa) (Yu et al. (2016); Garcia-Mendez et al. (2020)). Therefore, any dynamic volume change in Li metal at the interface can result in permanent Li deformation as LLZO is not adaptable to the drastic volume change. Moreover, the surface roughness of LLZO plays a critical role. Our surface mapping results showed that even a dense and smooth polished LLZO has numerous pores and surface defects (**Appendix B, Figure 2**). As a result, Li-LLZO interfaces are not flat and can have numerous nano/micron-scale asperities (**Appendix B, Figure 5**). This also can be realized from the substantial improvement in R_{int} when Li is melted on LLZO. At a molten state, Li can easily diffuse through these interfacial asperities which do not take place at room temperature, even when the stack pressure increases to 15 MPa. In this case, stack pressure might not be good enough to fill up the small-scale voids which are generated during the Li stripping process (**?**). The substantial difference in Li yield stress at nano/micron scales plays a critical role in stabilizing the interface. The subsequent impact of the non-recoverable voids can be seen during the plating process. In a typical symmetric cell setup, a similar long-term stripping process was carried out at 0.3 mA/cm^2 under 5, 10 and 15 MPa **(Appendix B, Figure 7a)**. The formation of non-recoverable regions was also observed from post-stripping EIS. Upon plating at the same current density, all the cells shorted in less than an hour. This demonstrates that the non-recoverable regions act as primary hotpots for unstable Li deposition during Li plating which initiates the dendrite formation. The influence of stack pressure, in this case, can be minimal as the yield stress of electrodeposited thin Li can be substantially higher than bulk Li. We carried out similar experiments at elevated temperatures (35°C, 50°C) and observed a noticeable improvement in the plating process due to the improved kinetics and Li creep **(Appendix B, Figure 7b,c)**. However, a negligible post-stripping creep effect was observed in both cases. which indicates negligible void growth **(Appendix B, Figure 7e,f)**.

4.6.3 Effect of Li Creep with respect to Capacity

To properly understand the time-dependence of Li creep-induced stabilization at different stages of stripping capacity, we prepared a modified symmetric cell with two different interfaces to enable stripping at high current density (0.8 mA/cm^2) stripping. To prevent

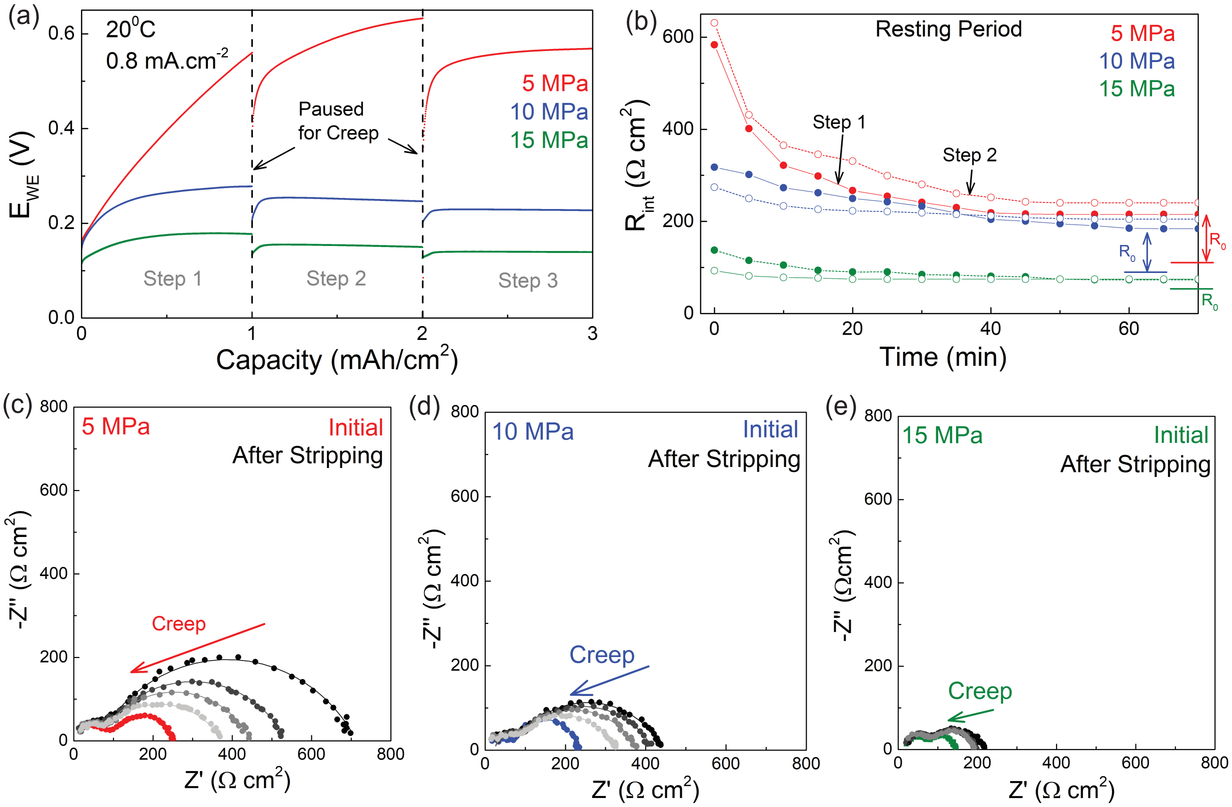

Figure 4.3: In a 3 electrode setup, step-wise stripping test (1 mAh/cm^2 per step) at 0.8 mA/cm^2, followed by resting for 2 hours. (a) Voltage profiles of Li stripping at 5, 10, and 15 MPa stack pressure and (b) creep-induced change in interfacial resistances during the resting period. EIS plots showing improvement of interfacial resistance due to Li creep during the resting period at (c) 5 MPa, (d) 10 MPa, and (e) 15 MPa.

cell shorting, Li foil was attached and heat-treated at only one side of LLZO, which is the plating side. Li at the stripping side was attached manually with no heat treatment. The process results in $R_{0,stripping}$ »$R_{0,plating}$ which allows a higher degree of void formation and a subsequent stronger creep effect. 1 mAh/cm^2 of Li was stripped at each step, followed by a brief hold (resting period) for allowing Li to creep. This step-wise stripping process was carried out for 3 cycles (**Figure 4.3a**). At 5 MPa, the 1st and 2nd steps of stripping showed a significantly high polarization (>500 mV). This is followed by a voltage drop at the 3rd step as Li creep is initiated to recover the loss of contact. When the stack pressure was increased to 10 and 15 MPa, the initial polarization was significantly suppressed due to the presence of the dynamic creep effect. The surface roughness of Li can experience a drastic increase due to the combined effect of a high rate of stripping and dynamic creep. During the resting periods, intermittent EIS measurements showed that pure Li creep enables a gradual contact improvement (**Figure 4.3c,d,e**). This demonstrates a time-dependent behavior of creep, as predicted by computational modeling. At 5 MPa, creep-induced deformation shows a continuous contact improvement for over 45 minutes before reaching a steady state (**Figure 4.3b**). At high pressure (15 MPa), the process stabilized the interface within 20 minutes. Although this transient process slows down over time, our experiments have shown no noticeable difference in R_{int}. We observed a similar phenomenon under static conditions where no electrochemistry (stripping/plating) was conducted **(Appendix B, Figure 6)**. By increasing the stack pressure, a better interfacial contact was established which showed slow improvement upon holding at the same pressure for over 2 hours. This further demonstrates that pure Li creep allows a faster rate of deformation at the initial period, which eventually reaches a steady state over time. The transient/dynamic creep effect of Li during the stripping process is staunchly different than pure creep as the interfacial contact loss and recovery occur simultaneously. This can significantly alter the local interfacial morphologies of Li and the overall contact area. The presence of non-recoverable voids after 1 mAh/cm^2 of Li stripping was observed as well, even at 15 MPa. This further confirms that the initial period of stripping causes an irreversible voiding and damage to the interface due to Li depletion at the local asperities which might need a significantly higher stack pressure (>40 MPa) to recover. We also showed that the extent of void growth can be highly suppressed by increasing stack pressure from 5 to 15 MPa.

4.6.4 Effect of Li Creep on Plating and Dendrite-induced Shorting

Li deposition at the plating side is considered to be the malefactor for filament formation and subsequent shorting in solid-state batteries. The underpotential during the plating process is directly related to the initiation of Li nuclei ($Li^+ + e^- \rightarrow Li$) on the Li metal

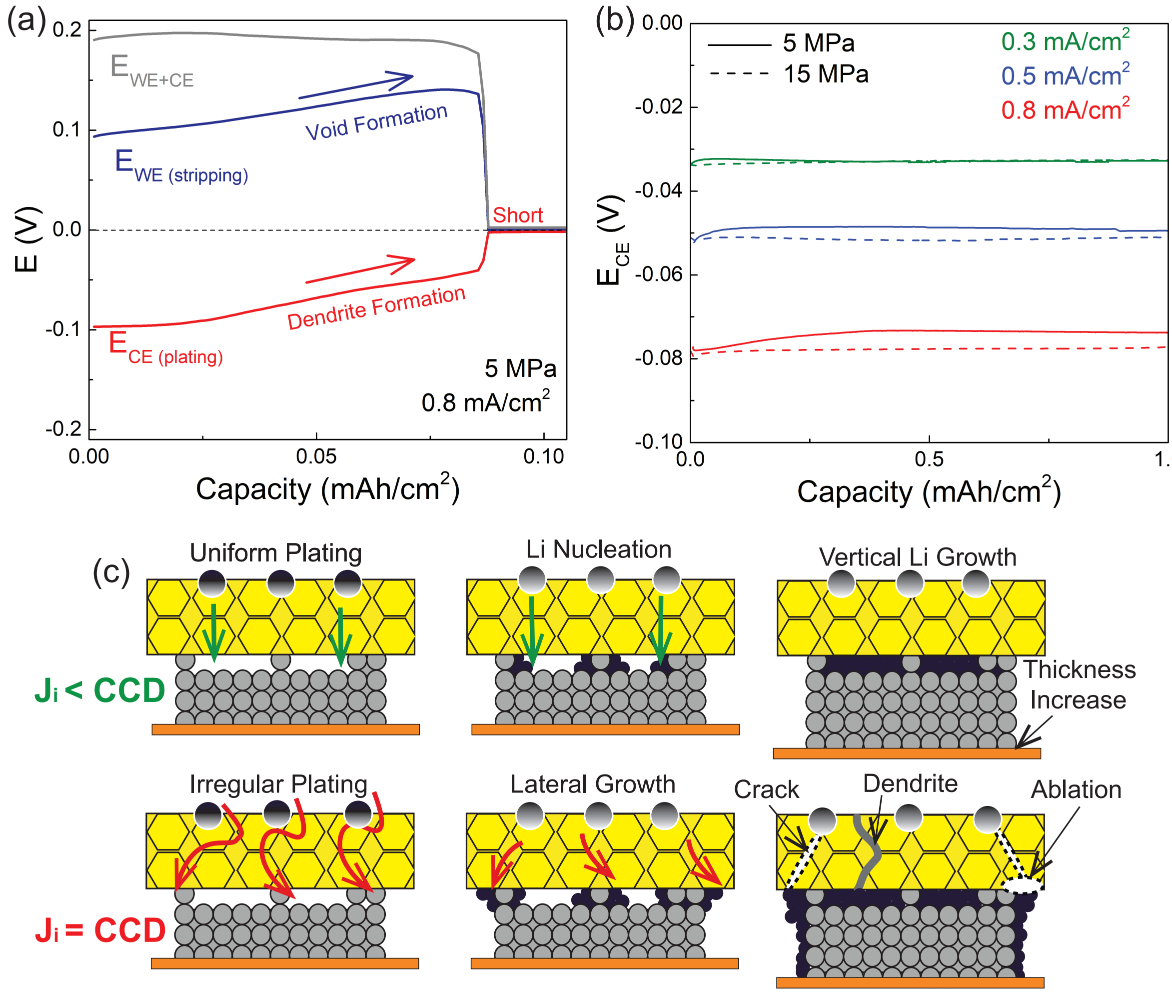

Figure 4.4: (a) Stripping and plating profiles of a symmetric cell in the 3-electrode setup, showing the plating induced shorting at 0.8 mA/cm^2. The stripping side has a negligible impact on cell shorting. (b) Plating profiles of a symmetric cell at 0.3, 0.5 and 0.8 mA/cm^2. (c) Schematic of Li plating mechanism at low and high current density, displaying the effects of irregular and isolated Li deposition on LLZO.

anode. Previous reports have shown that Li has preferred nucleation sites which are generally along the surface irregularities of LLZO (Porz et al. (2017); Swamy et al. (2019)). The electrodeposition instability is correlated to the molar volume difference between Li nuclei (Li$^+$) and bulk Li metal (**?**). The size, shape, and density of Li nuclei (or Li particles) highly depend on the current density and temperature. Computationally, nuclei growth is generally modeled as columnar growth of Li. As electrodeposition continues, the thickness of the bulk Li (plated side) gradually increases due to further columnar growth. Depending on the contact area, Li deposition kinetics at the interface generate high stress (hydrostatic) points which lead to abnormal growth of Li. This instability initiates the formation of dendrites which prompts cell shorting. In a galvanostatic measurement, this can clearly be distinguished in a 3-electrode setup where the stripping and plating voltage can be separately observed. At low current density, slower growth of Li nuclei facilitates uniform deposition along the interfacial area which results in a steady (vertical) increase in Li thickness (**Figure 4.4c**). In this case, hydrostatic stress at the interface is uniformly distributed. As the current approaches the critical limit, electrodeposition becomes highly irregular which severely affects the interfacial morphologies on the plating side. This further exacerbates if $R_0^{plating}$ >10 Ωcm^2. Irregular Li plating at the pre-existing voids rapidly initiates the flux imbalance as more Li particles are nucleated at the interface. This gives a significant rise in the local electronic structure of LLZO which initiates dendrite formations, followed by further elongation along the grain boundaries and eventually shorts the cell (**Figure 4.4a**) (Liu et al. (2021); Tian et al. (2019)). The quick drop of plating voltage is a common indicator for dendrite formation and subsequent cell death. It is also clear that the stripping process has no noticeable influence on this mechanism. We also observed that, if the current is reversed before the voltage drops down to $\approx$0V, the dendrites can be pushed back and the cell shorting scenario can be prevented. The stack pressure-induced Li creep due to plating is rather minimal. However, we observed that higher pressure leads to a more uniform plating profile. The effect is more visible when the current density is increased to 0.5 and 0.8 mA/cm^2 (**Figure 4.4b**). Post-stripping pellet observation showed a clear expansion of the Li electrode area on the plating side. This expansion was visually more apparent after depositing a large volume of Li (15 mAh/cm^2) and can be attributed to the lateral growth of Li which occurs at high current density **(Appendix B, Figure 9)**. After removing the Li and cleaning the surface, a clear ablated zone of LLZO was noticed at the edge of contact which was filled with Li metal. This spallation can be correlated with the irregular deposition morphology of Li

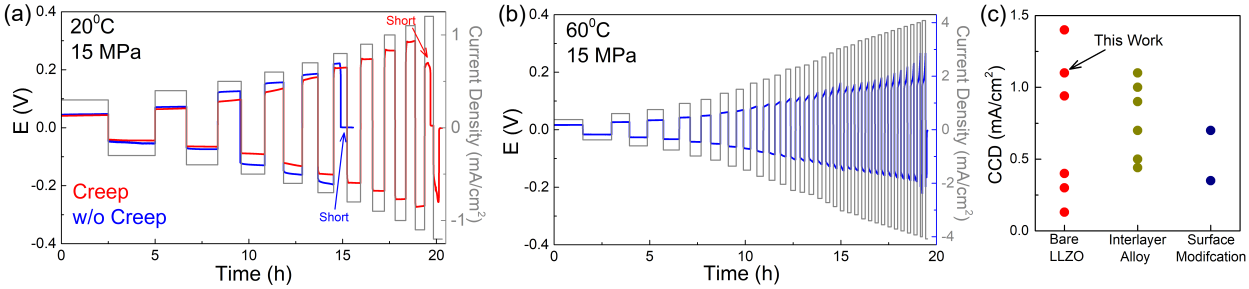

Figure 4.5: (a) Comparison of critical current density (CCD) of LLZO at 20°C, with and without creep protocol. (b) CCD of LLZO at 60°C. (c) Comparison of room-temperature (20-25°C) critical current densities reported for Li metal and LLZO. "Bare LLZO" represents the CCD of Li|LLZO without any interlayer or surface alterations Sharafi et al. (2016); Wang et al. (2019b); Chang et al. (2021); Yang et al. (2021a); Cheng et al. (2015). "Interlayer/Alloy" represents the CCD where a thin interlayer or alloying mechanism was used to increase the wettability Dussart et al. (2021); Ma & Xu (2022); Huang et al. (2018); Su et al. (2019); Lu et al. (2018); Chen et al. (2022); Mu et al. (2022). "Surface modification" represents the CCD where surface structure of LLZO was modified by patterning Xu et al. (2021c); Fu et al. (2020).

at a high current density where additional but isolated Li filament can grow and reside at the sub-surface of the plated regions (Kazyak et al. (2020a)). Such phenomena at the edges on the plating side were also microscopically observed in sulfide electrolytes where the local electric fields are higher (Ning et al. (2021)). Thus, the detrimental outcomes for plating at high current density are (i) uncontrolled and irregular Li growth (vertical and lateral), (ii) mechanical failure of electrolyte (ablations and cracks), and (iii) increase in interfacial electronic properties (**Figure 4.5c**). We did not find any such features on the stripping side, even after the complete depletion of Li. Instead, a dark red shade of a few microns was observed. The origin of this dark red region is unclear but can be originated from an electrochemically induced surface corrosion of copper foil and Li **(Appendix B, Figure 9)**.

4.6.5 Effect of Creep on Critical Current Density

Here, we utilized the pure creep to re-stabilize the interface after stripping by introducing a simple 15 minutes of resting period after each cycling. The initial contact resistance for the symmetric cell was 3 Ωcm^2 and 15 MPa of stack pressure was applied at 20°C. This approach yields a CCD of 1.1 mA/cm^2 which is noticeably higher than what frequently has been reported in the literature (**Figure 4.5a**). The effect of high stack pressure and subsequent creep (due to resting) is evident from the EIS measurements as they showed almost no increase in interfacial resistances. Demonstration of high room temperature CCD for LLZO was mostly achieved by a lithiophilic interlayer (Au, In, ZnO) to increase the Li wettability (**Figure 4.5c**). In this work, we showed that by applying a stack pressure on perfectly wetted LLZO and subsequent creep, the room temperature CCD value of LLZO can be significantly increased. The effect of improved kinetics was further understood from measurements taken at 60°C. A higher value of CCD was obtained (4 mA/cm^2) due to a substantially higher creep rate of Li and low charge transfer resistance of LLZO at 60°C (**Figure 4.5b**). We also looked at the stripping limit of LLZO where Li can be stripped up to 2.4 mA/cm^2 at 20°C without shorting, which can be denoted as critical stripping current density ($CCD_{stripping}$) **(Appendix B, Figure 8)**. This further illustrates that by allowing stack pressure-induced deformation (static and dynamic), stable dissolution of Li at high current densities can take place. However, the subsequent deposition is restricted by the extent of void growth which can initiate dendrite formation and short the cell.

4.6.6 Effect of Stack Pressure on Full Cell Performance

The influence of stack pressure on the solid-state cathodes is widely explored as a means to improve the areal capacity and cyclability. In this work, we also evaluated the effect of stack pressure on LLZO-based full cells at different operating conditions. Similar studies on sulfide and halide electrolytes were carried out where small or negligible improvement was observed in cycling performances (Doux et al. (2020b); Gao et al. (2022)). The ionic conductivity of these electrolytes is, however, pressure-dependent which is not the case for LLZO. Here, we chose $LiFePO_4$ (LFP) for composite cathode formulation.

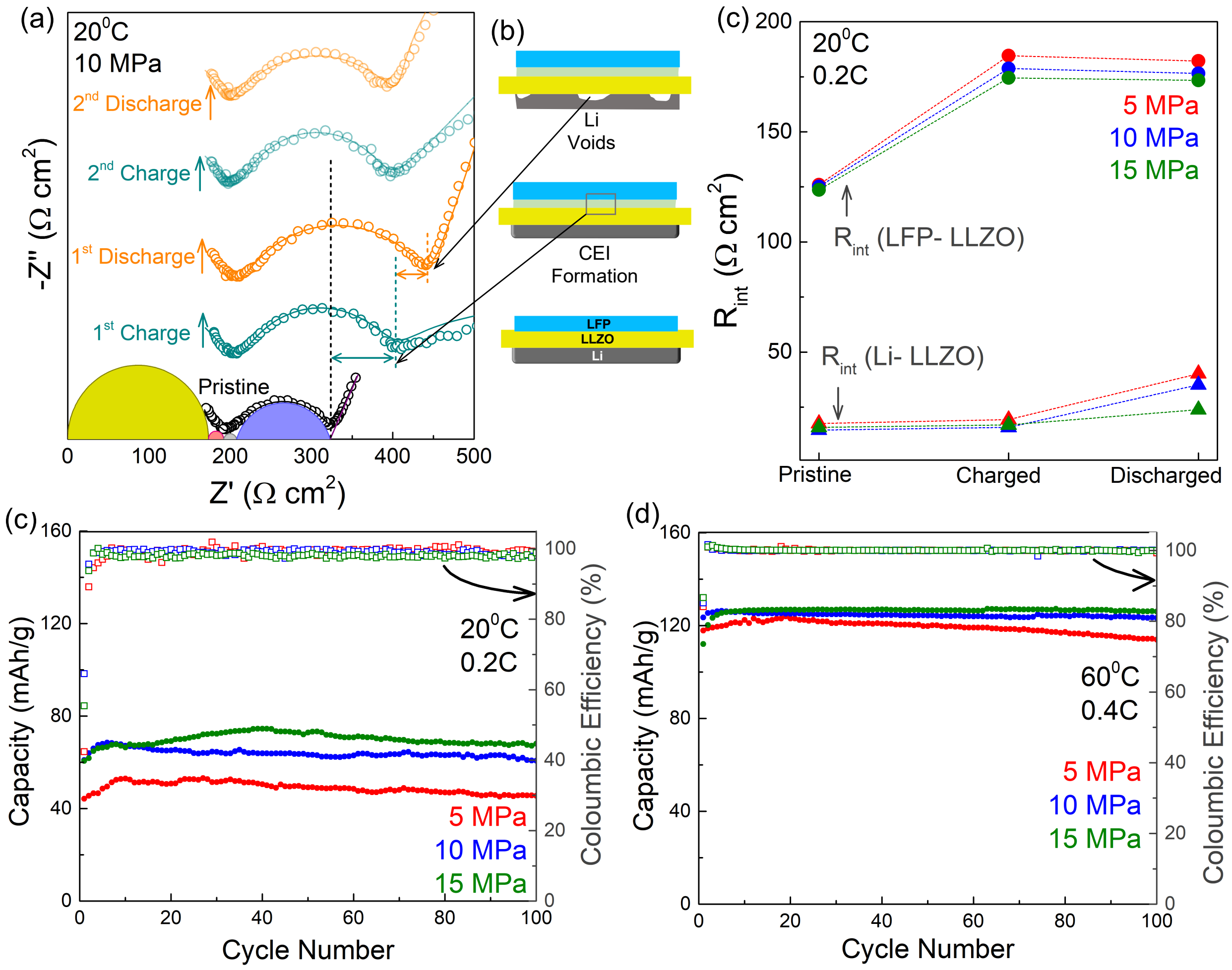

Figure 4.6: (a) Nyquist plots of a Li|LLZO|LFP full cell displaying interfacial evolution during the first charge and discharge. The yellow, pink, grey, and blue semicircles represent the resistance of bulk, grain boundary, and anodic and cathodic interface. (b) Schematic of interfacial change during full cell cycling, (c) Change in interfacial resistance of LFP|LLZO and Li|LLZO during first charge and discharge. Stack pressure dependent cycling performance of a Li|LLZO|LFP full cell at 5, 10 and 15 MPa at (d) 0.2C, 20°C and (e) 0.4C, 60°C. The areal capacity of the cathode was 2.2-2.3 mAh/cm^2.

LFP shows very negligible volume change upon lithiation/delithiation and is chemically more stable against solid electrolytes. The interfacial evolution of full cells was determined by EIS measurements. A typical Nyquist plot of LFP|LLZO|Li at 20°C indicates a significantly higher cathodic interfacial resistance ($R_{int}^{cathode}$) compared to that of a symmetric cell **(Appendix B, Figure 12)**. This is generally attributed to the intrinsic R_{int} of composite compounds (active material, Carbon, binder, and LiTFSi), charge transfer resistance ($R_{CT-cathode}$) and interfacial contact resistance ($R_{LFP-LLZO}$). The value of $R_{LFP-LLZO}$ demonstrated a pressure dependence and a stack pressure of 10 MPa was required to ensure a proper electrode attachment (fabrication pressure). The impedance spectra also exhibit a Warburg-diffusion tail at low frequencies. To isolate the cathodic and anodic interfacial contributions, we evaluated the corresponding Bode plots and identified two separate electrochemical processes in the mid-frequency range (10^2-10^4 Hz) and low-frequency range (1-10^2 Hz) **(Appendix B, Figure 12b)**. Two separate RQ (resistive - constant phase element, CPE) elements were assigned to delineate the impedance contributions. The mid-frequency range is attributed to the anodic (Li|LLZO) interface and the low-frequency range is attributed to the cathodic (LFP|LLZO) interface. To further clarify, distribution of relaxation time (DRT) analysis was carried out on the respective EIS profiles **(Appendix B, Figure 12c)**. The DRT curve in full cell showed three distinguished peaks (P3a, P3b, and P3c) within the frequency range of 1-10^3 Hz. The absence of P3b and P3c peaks in symmetric cell DRT plots signifies an additional electrochemical process that stems from the cathodic interface in full cells. Upon confirming this, we fit the impedance spectra by an equivalent circuit of total 4 RQ elements; $(RQ)_{bulk}$, $(RQ)_{GB}$, $(RQ)_{anode}$, $(RQ)_{cathode}$ and W (Warburg diffusion) **(Appendix B, Figure 11)**. It should be noted that this process was only carried out for full cells operated at 20°C. At high temperature, the interfacial contributions overlap in the EIS spectra which make the deconvolution of the Nyquist plots difficult.

For long-term full cell cycling under stack pressure, two operating conditions were considered; 0.2C at 20°C and 0.4C at 60°C (**Figure 4.6c,d**). Both operating conditions showed a low coloumbic efficiency of (<70% for 20°C and <90% for 60°C in the 1st discharging cycle. The discharge capacity for the 1st cycle also was significantly lower. This was readily recovered from the consecutive cycles. At 20°C, a noticeable stack pressure influence was observed. At 15 MPa, discharge capacity showed a continuous increase (from 50 to 73 mAh/g for 43 cycles **(Appendix B, Figure 10c)**. Similar phenomena were observed for 5 and 10 MPa, although the increment stopped earlier **(Appendix B, Figure 10a,b)**. Although the discharge capacity values are lower (30-43% of theoretical capacity of LFP, 170 mAh/g), an excellent retention rate for over 100 cycles was obtained for the full cells (highest for 15 MPa) **(Figure 6c)**. Coulombic efficiency also ranged between 98-100%. At 20°C, the capacity of the LFP composite is restricted by sluggish ion kinetics. This is usually overcome by adding a small amount of liquid electrolyte (with solvent) on the cathode side for good wettability, which is widely reported in the literature (Han et al. (2017); Lu et al. (2018)). In general, the capacity decay in solid-state cathodes is attributed to interfacial contact losses which can occur within the composite structure of the cathode itself or by delamination within bulk interfaces (Wang et al. (2019a); Barai et al. (2021)). The later process which signifies a lower electrochemically active surface area is usually responsible for a faster decay (<10 cycles) (Tsai et al. (2019)). We found that by employing a moderate stack pressure, the delamination-induced capacity decay can be effectively suppressed, as seen by the excellent retention rate. Stack pressure also plays a critical role in maintaining a conformal contact on the anodic interface. Like in symmetric cells, void formations in Li anode (during discharging) take place in full cells which grow upon long-term cycling and can eventually lead to shorting (**Figure 4.6b**). Our findings from symmetric cell measurements, where at least 10 MPa of stack pressure was recommended for LLZO, hold also for full cells.

Although creep-induced phenomena do not exist in composite cathodes, we observed a significant increase in full cell interfacial resistance after the 1st charging process (**Figure 4.6a**). After discharging and further cycling, this resistance decreases but a significant gap from the initial resistance was observed (**Figure 4.6b**). This non-reversible resistance can be attributed to the formation of a cathode-electrolyte interphase (CEI). Although the origin of this CEI layer is unclear, first-principle calculations have predicted several chemical interphases (Li_3PO_4, $LaFeO_3$, and Fe_2O_3) may form between LFP and LLZO (Miara et al. (2015)). The formation of electrochemically driven degradation products

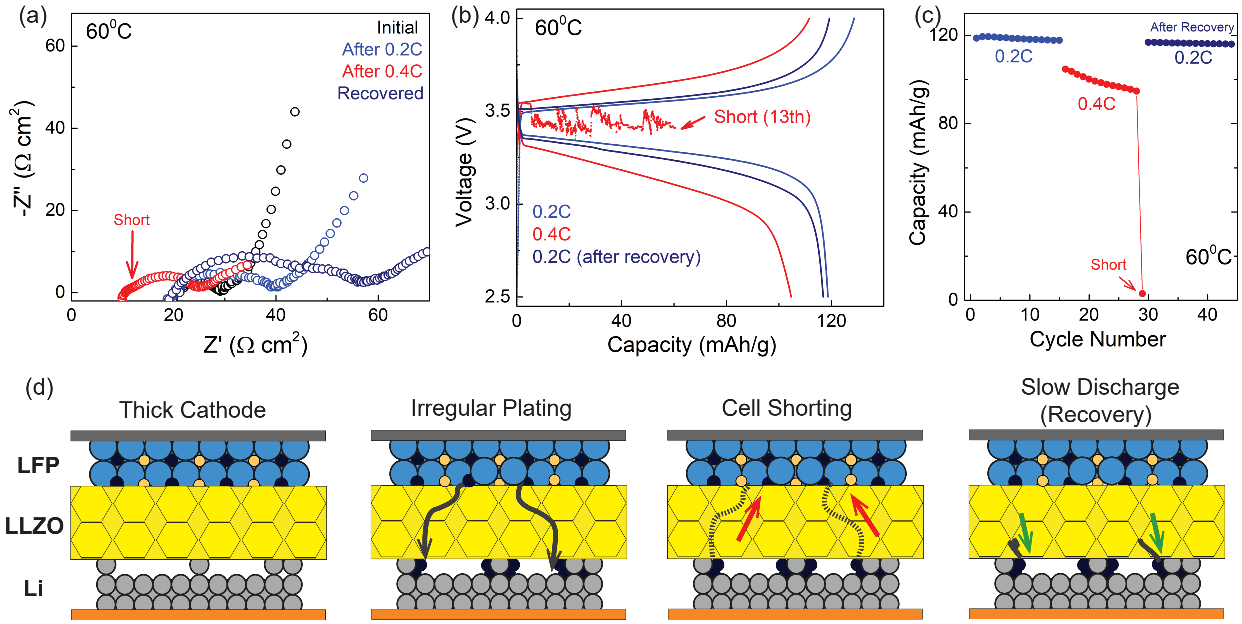

Figure 4.7: (a) Cell resistance evolution of Li |LLZO|LFP full cells with the thicker cathode (4.6 mAh/cm^2 areal capacity) after cycling at 0.2C and 0.4C. (b) Galvanostatic charge/discharge profiles at high current density showing cell failure at 0.4C at the 13th cycle and subsequent recovery after slow discharging (0.1C). (c) Cycling performance of the cell at 0.2C and 0.4C. The operating temperature was 20°C and stack pressure was 10 MPa. (d) Schematic of the cell cycling, failure, and recovery demonstrating the reversible shorting behavior in full cells.

was also observed with other cathodes (LCO, NMC) (Park et al. (2016)). In this case, we assume the CEI layer might be metastable, which stabilizes the kinetics of the cathodic interface for long-term cycling.

We also observed that the role of stack pressure becomes minimal once the operating temperature increases up to 60°C. At 0.2C, a similar full cell delivers 143 mAh/g of capacity which is due to improved kinetics of composite cathode. For longer term cycling at 0.4C, stack pressure shows a slightly higher capacity at both 10 and 15 MPa (130 mAh/g), with >98% retention (**Figure 4.6d**). The non-reversible resistance growth is also observed at 60°C but may play a similar role in stabilizing the cathodic interface **(Appendix B, Figure 13)**.

4.6.7 Plating-induced Short Circuiting in Full Cells

The impact of current density and subsequent shorting mechanism in a solid-state full cell can be fully understood with an increased areal capacity. Here, we employed a thicker composite cathode with an areal capacity of ≈4.6 mAh/cm^2 with the same active material loading (55%). Due to increased capacity, the corresponding current density with respect to Li increased to ≈2 mA/cm^2 at 0.4C. For better utilization of active materials, we operated the battery at 60°C and compared the performance with respect to (**Figure 4.6d**). At 0.2C (current density 1 mA/cm^2), the cell delivered a capacity of 120 mAh/g with good retention (**Figure 4.7c**). However, at 0.4C, the polarization in the cell noticeably increased and a faster rate of decay during discharge (3.3-3.5V) was observed (**Figure 4.7b**). The discharge capacity gradually decreased from 105 mAh/g to 95 mAh/g within 12 cycles and a shorting appeared at the 13th cycle (**Figure 4.7b**). The capacity decline and sudden shorting of the full cell can be attributed to the dendrite growth which is similar to what was observed in symmetric cells. Similar shorting in full cells for high areal loading was reported for sulfide electrolytes with NMC cathodes, but the electrochemical signature for shorting in LLZO is found to be different (Lewis et al. (2022)). The post-short EIS profile showed a decrease in cell resistance and a clear leftward shift of the semi-circle, which confirmed the existence of internal shorting (**Figure 4.7a**). However, this behavior is significantly different than what is commonly observed in a shorted symmetric cell where overall cell resistance decreases to almost 0 Ωcm^2. After a slow discharge process at 0.1C, we observed an immediate recovery of the cell, which can be seen from the EIS profile (**Figure 4.7a**). Such reversible phenomena are not generally observed in symmetric cells where Li^0 dendrite can form a permanent electronic connection between the two electrodes. This indicates the reversible nature of dendrites which can be reversed back to the anode upon slow discharging ($\text{Li}^+ + \text{e}^- \rightarrow Li$). This provides additional insights into the role of anodic (Li|LLZO) interfacial evolution in full cells. Despite the unwanted increase in cell resistance, the formation of the CEI layer does not drastically affect cell performance. However, upon further cycling at a high C-rate, high anodic interfacial voids and irregular plating can decrease the lifetime of the battery. As a result, full cells also require an optimum stack pressure (>10 MPa) to maintain a stable Li|LLZO interface during battery cycling.

4.7 Conclusion

Interfacial evolution in solid-state batteries is a highly dynamic process that requires multiple control/mitigation approaches for stable operation and high performance. Creep is one of the dominant factors in stabilizing the ever-changing alkali metal-solid electrolyte interfaces. In this work, we briefly evaluated the creep effect of Li metal with garnet LLZO electrolyte with respect to the areal capacity, stack pressure, contact resistance, current density, and temperature. Our experimental findings are further corroborated with multi-scale time-dependent contact modeling. This work is focused on key chemomechanical aspects of cell levels, for an extended amount of Li transport (5 mAh/cm^2). With the aid of 2-electrode and 3-electrode setups, we investigated the creep effect under both static and dynamic conditions. Higher stack pressure enables faster Li to creep rate and induces high Li diffusivity for preventing void formations. Static creep (resting period) noticeably improves the contact points of Li which is evident in 20°C. The time-dependent plots of Li creep showed the fastest contact recovery at the initial period of resting, which is mostly stabilized in 30-60 minutes. However, a "non-recoverable" region exists after creep which signifies an accumulated growth of pores and voids that generate within the local interfacial asperities. These local gaps are considered potential hotspots for irregular Li growth and dendrite initiation during plating. This was further corroborated by the plating profiles at high current densities where a small interfacial gap can initiate faster failure (as observed from decreasing potential). We also demonstrated a feasible approach to achieve a negligible interfacial resistance with Li which enables us to achieve a high critical current density of 1.1 mA/cm^2 at 20°C. We further investigated the impact of stack pressure and temperature on full-cell configurations. Although a slight improvement in rate performance was observed (both at 0.2C - 20°C and 0.4C - 60°C), higher stack pressure provides better prevention against delamination of Li or LFP which results in excellent retention properties (>98%) after 100 cycles. EIS evolution reveals the presence of a metastable cathode|electrolyte interphase after 1st charging cycle in all cases which may be originated from the chemical dissociation of composite cathodes. This however showed less impact on battery cycling performances. We also investigated the shorting behavior of full cells by employing a thick cathode (high areal capacity) where the importance of a stable anodic interface was further emphasized. Our work highlights the various rate-limiting factors that exist in a model solid-state Li-metal battery system which can be determined by electrochemical analysis. Further understanding of these limitations beyond the scope of electrochemistry can enable rational tuning and designing of solid electrolytes and electrodes for next-generation Li-metal batteries.

Chapter 5

Electrodeposition Dynamics in Solid-state Batteries: From Lithium metal toward Anode-free Approaches

5.1 Introduction

Boosting the energy density and cycle life in rechargeable Li-ion batteries is of utmost interest for electric vehicle and grid energy storage applications. The energy density of commercially available Li-ion batteries is limited by the low percentage of active materials in cell modules (Armand (1983a); Albertus et al. (2018)). Replacing the graphite anode with Lithium metal may improve the cell level energy density by 2-3×. However, Li metal is highly reactive in conventional liquid electrolytes which leads to low coulombic efficiency and serious morphological issues (e.g.; 'dead' Li and dendrites) (Hatzell et al. (2020); Chen et al. (2017b)). Solid electrolytes are mechanically rigid and can potentially suppress the dendritic growth and enable safer cycling performance (Hitz et al. (2019); Zheng et al. (2019)). Hence, all solid-state Li metal batteries are considered a promising alternative for next-generation power sources (Janek & Zeier (2016b)).

Li metal in a solid-state battery experiences several chemical, mechanical and electrochemical challenges due to its large volume changes. In addition, unstable electrodeposition can lead to the formation of dendrites which readily propagates through the electrolyte and cause shorting. These phenomena are attributed to dynamic chemomechanical transformations that occur at the solid|solid interfaces (Krauskopf et al. (2019b); Kasemchainan et al. (2019)). During Li plating, compressive stress buildup at the interface is considered one of the root causes of dendrite initiation. The stress generation can range between several MPa which is significantly higher than typical conversion type anodes (e.g.; Graphite, $Li_4Ti_5O_{12}$) (Koerver et al. (2018)). Lithium metal electrode kinetics is impacted by chemo-mechanical effects that occur at buried solid electrolyte-anode interfaces. Thus, the mechanical properties of the solid electrolyte can drastically impact the reversible operation of lithium metal. In addition, the morphology of the solid electrolyte-anode interface can affect electrodeposition processing (e.g. plating) (Kim et al. (2020)). Pre-existing interfacial defects are regions that experience high local ionic flux and are preferred sites ('hotspots') for Li nucleation Isolated Li plating can take place at various random hotspots, even at lower current densities, which can lead to dendrite formations. Prior computational works suggested that the current focusing at the tip of the plated Li nuclei generates a high-stress field across the surface flaws of the electrolyte (Tewari & Mukherjee (2020); Tu et al. (2020)). If thermodynamically favorable, the nuclei grow (Li^+ + $e-$ $\rightarrow$ Li), followed by stress relaxation upon contact with bulk Li. Otherwise, gradually developing high-stress points drastically alters the deposition kinetics and propagates cell shorting (Mistry & Mukherjee (2020); Li et al. (2019a)). Understanding the origin and evolution of this internal compressive stress buildup is critical to controlling the kinetic factors and tuning parameters for uniform deposition of Li.

Recently, an anode-free geometry has recently emerged as a suitable alternative to overcome the challenges associated with Li metal. Li is uniformly plated directly on the current collector (without anode) and then cycled back to the cathode during discharge. The absence of excess Li from Li-metal would result in a 2X increase in both gravimetric and volumetric energy density (Heubner et al. (2021)). This *in situ* approach for Li deposition can also mitigate bulk volume change in thick Li anode during cycling. Furthermore, the cost, energy, and technological requirements associated with anode production are further eliminated (Schnell et al. (2019)). However, several challenges are restricting the practical application of anode-free Li metal batteries. Generally, the "mossy" growth of electrodeposited Li and reactivity toward liquid electrolytes lead to continuous electrolyte decomposition and the formation of "dead Li" after multiple cycling and delivers very low coloumbic efficiency. Alternatively, solid electrolytes can potentially enable uniform Li deposition on a current collector (CC) to create a temporary reservoir of Li. Here, conformal contact between the current collector and solid electrolyte is important to avoid inhomogeneous current distribution at the SE|CC interface. However, lamination of conventional current collectors (e.g.; Cu, Ni) on solid electrolytes can be process-sensitive. This is generally achieved by high-temperature hot pressing or thin-film deposition techniques (Wang et al. (2021c); Davis et al. (2021); Krauskopf et al. (2019a); Yang et al. (2018); Liu et al. (2020)). The nature of Li deposits highly depends on current collector material, thickness, applied current density, stack pressure, and temperature. Prior works on LIPON electrolyte interfaces showed a strong current density and temperature dependence on Li nucleation, nuclei size, and subsequent growth (Motoyama et al. (2015, 2020)). The molar volume change of the deposited Li plays a pivotal role during cycling. *In-situ* plating of Li leads to the separation of SE|CC interface. This is followed by plastic deformation of plated Li due to pressure buildup. At high current densities, a significantly higher pressure buildup due to Li flux and current focusing affects the chemomechanics of Li deposition and leads to immediate cell shorting. Hence, the cycling performance of anode-free configurations is limited to low-rate operations and requires novel current collectors to allow Li deformations without significant pressure generation.

Similar to Li anode, volume change and resulting pressure build-up frequently occur within composite cathodes in solid-state batteries (Shi et al. (2020b); Koerver et al. (2017)). In conventional batteries, ion transport in cathodes is facilitated through the pores by liquid electrolyte infiltration. However, these pores act as "ion-blocking" regions in solid-state batteries. Hence, internal stress buildup evolves due to volume expansion/contraction upon lithiation/delithaition. The chemomechanical transformation of solid-state cathodes is critical in dictating the rate performance of the solid-state batteries (Ebner et al. (2013); Zhang et al. (2012)). Structural failure of cathodes is exacerbated by the presence of large pores/voids (the gap between solid particles) and low electronic/ionic transport within composite structures (Shen et al. (2019a); Kim & Rupp (2020); Delluva et al. (2020)). The volume change within the state-of-the-art cathode materials (e.g.; $LiCoO_2$

(LCO) or $LiNiMnO_2$ (NMC)) is highly anisotropic. During delithiation, the unit cell volume of LCO undergoes expansion (positive molar volume change), and NMC exhibits contraction (negative). In a composite cathode structure, this repetitive change increases local stress points and leads to elastic/plastic deformation of both active and ion conducting materials. As a result, the accumulated stress can eventually lead to low active material utilization, particle fracture, poor interfacial transport, and severe contact loss. Poor reversible capacity and faster decay of rate performance are the consequential outcomes of the cathodic degradation (Zhang et al. (2017a)). Understanding the stress evolution in cathodes is vital for mechanically optimized and rationally designed high-performance solid-state batteries (Larson et al. (2018)).

In this work, we elucidated the volume expansion of Li metal by monitoring the pressure evolution in a solid-state battery. We emphasized the stress distribution during Li plating that results in battery failure. In a full cell configuration, we employed a cathode of negligible volume change ($LiFePO_4$) to monitor the pressure buildup during the slow and fast charging process. Lastly, we explored the prospects of non-conventional current collectors for uniform Li deposition in anode-free solid-state batteries. The importance of the underlying electro-chemo-mechanics of Li is briefly discussed.

5.2 Experimental

5.2.0.1 Synthesis of LLZO Solid Electrolyte

Ta-doped $Li_7La_3Zr_2O_{12}$ solid electrolyte was prepared by ball milling the precursors LiOH (pre-dried at 200°C for 6 hours), La_2O_3 (pre-dried at 900°C for 10 hours), ZrO_2 and Ta_2O_5 in stoichiometric ratio. Anhydrous isopropanol was used as a milling solvent. The ball milling was carried out in Pulverisette premium for 4 hours at a rotation speed of 500 rpm. The mixer was then dried under air for solvent evaporation and collected via sieving. The precursor powder was then annealed at 900°C for 8 hours under air. Another round ball milling was carried out to reduce the particle size (350 rpm, for 2 hours).

The powder was then pelletized (10 mm dia) under 300 MPa for 15 minutes. The pellets were then covered with additional LLZO (mother powder) and sintered under O_2 flow at 1235°C for 8 hours. After sintering, the pellets were cleaned and wet-polished with sandpapers to ensure a smooth surface. The final pellets have a relative density of 95-96% and thickness of around 1.5 μm. The pellets were then stored in an Argon-filled glove box.

5.2.0.2 Cell Assembly

To assemble Li on LLZO, thin Li foil of 4 mm dia was punched and attached to the LLZO surface at 10 MPa. A Copper foil was pressed on top of Li foil as a current collector. Then the Li-LLZO assembly was heated up to 220°C for 30 minutes. Full cells were prepared by employing composite $LiFePO_4$ (LFP) cathode on Li-LLZO half cell. The cathode composite was prepared from a slurry comprised of LFP, conducting carbon (super P), PVDF binder, and LiTFSi salt with a weight ratio of 55:10:10:25. N-Methyl-2-pyrrolidone (NMP) was used as the solvent. The wet slurry was cast on a Carbon coated Aluminum foil and dried at 100°C for 24 hours to remove the solvent. Cathode discs (4 mm dia) were punched from the dry film and attached to LLZO by applying 10 MPa of pressure. The assembly was then transferred to the small cell chamber (Sphere Energy) and a stack pressure was applied by using a pressure frame (**Figure 5.1**). The cell chamber is equipped with a heating element and K-type thermocouple for temperature-controlled experiments. The pressure frame consists of a load cell at the bottom which is connected to a PID controller. The voltage output for pressure change was collected in real-time. An initial stack pressure of 10 MPa was applied and let the setup stabilize for at least 2 hours. The pressure drift was observed initially which is used as a reference for background correction. The pressure was recorded by using a data logger connected to the PID controller.

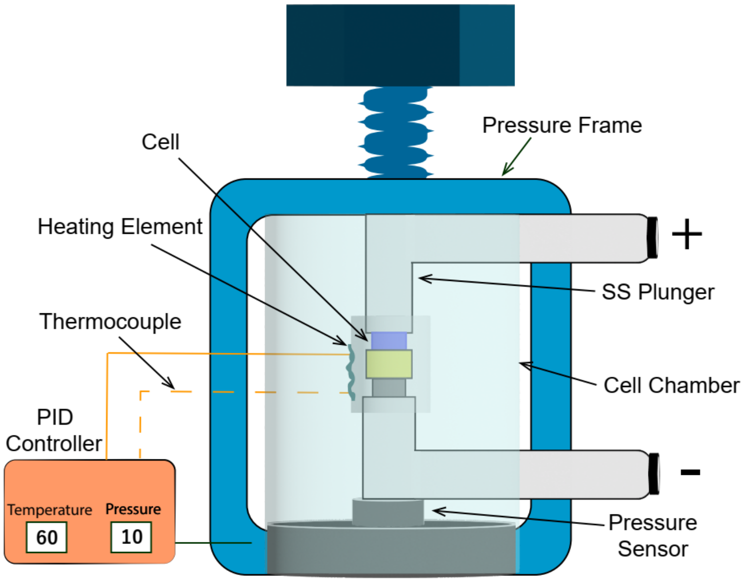

Figure 5.1: Schematic of the pressure cell setup for operando stress monitoring.

5.2.1 Anode-free Plating of Li

For anode-free plating of Li, a graphite foil was used as a current collector. A 4 mm graphite disc was punched which has a thickness of ≈300 μm. In a Li|LLZO|Graphite half cell configuration, the foil was attached on LLZO by applying 30 MPa of pressure, followed by a heat treatment at 250°C for 1 hour. The heat treatment improves the interfacial adhesion properties of LLZO and graphite. Li foil was attached on the other side by following the strategy of a typical symmetric cell. The cell was assembled in a customized Nylon chamber with controlled stack pressure.

5.2.2 Electrochemical Measurements

Potentiostatic electrochemical impedance spectroscopy (PEIS) was carried out from 1 MHz to 0.1/1 Hz. Cycling profiles of symmetric and full cells were conducted under a galvanostatic current. Full cells were cycled between 2.5- 4V.

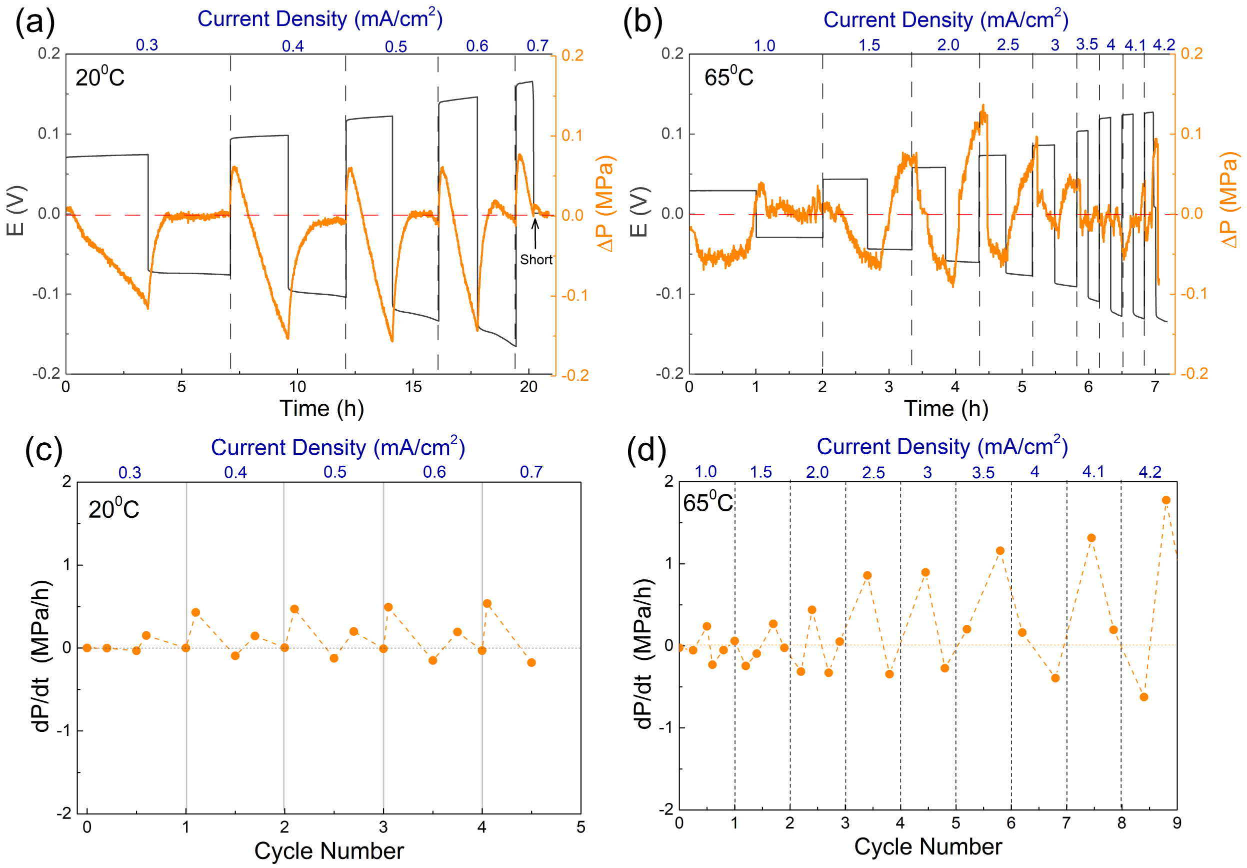

Figure 5.2: Stress response of a symmetric cell during critical current density measurement at (a) 20°C and (b) 65°C. Differential pressure (dp/dt) response of the corresponding cycles at (c) 20°C and (d) 65°C.

5.3 Results and Discussion

5.3.1 Influence of Stress Rate on Cell Shorting

During symmetric cell cycling, the stripping side faces an inevitable loss of contact points of Li and solid electrolyte due to continuous depletion of Li (Zhang & Fujimori (2020)). As a result, the contact resistance on the stripping side increases gradually which causes significant polarization (Kasemchainan et al. (2019); Krauskopf et al. (2019c)). We briefly discussed in Chapter 4 that cell polarization is attributed to the stripping electrode due to contact loss. The plating profiles are relatively flat with no sign of polarization. As both the stripping and plating side experience significant volume change, simultaneous depletion and deposition trigger pressure loss (-σ) and gain (+σ). Detection of local stresses within a battery is challenging, but system-level pressure measurements can be monitored using relatively straightforward measurement techniques. When Li is depleted away during stripping, a negative stress buildup was observed which is alleviated to an extent by a subsequent volume change at the stripping electrode. As new Li deposits on the bulk Li metal, compressive stresses gradually increase at the plating side. An interplay between two pressure was observed which dictates simultaneous contact loss and gain of Li (**Figure 5.2**). Here, we considered the negative stress rate as the primary contributor to the slow pressure buildup observed in the experiment (**Figure 5.2a**). critical current density test was carried out at room temperature (20°C), where a short circuit occurred at 0.7 mA/cm^2. During the first stage of stripping/plating, a noticeable pressure drop is observed, followed by a steady increase. The sudden drop can be correlated to the initial nucleation stage of Li plating. These phenomena were observed after the first cycle (at 0.3 mA/cm^2) where voids develop and grow over time. The pressure oscillation can be considered as the outcome of the interplay between pressure loss (due to contact loss) and pressure gain (due to new contact). We calculated the stress rate at different stages of Li plating/stripping (**Figure 5.2c**). At low current density (<0.3 mAh/cm^2), a slow nucleation rate along the defect sites favors the growth of multiple seed layers which causes a low-pressure buildup. Hence, a minor change in stress rate was observed. However, when the current density is higher, the steady "void growth-mitigation" mechanism alters significantly as the pores form faster and bulk Li diffusion can not completely replenish the interfaces. In addition, the stable plating profile is affected by irregular Li growth and isolated regions of plating. As a result, a stress factor of >0.5 MPa/h is observed, which causes cell shorting at the subsequent current density. From a pressure standpoint, preventing a pressure loss during Li depletion is critical for preventing cell shorting. During plating, Li tends to quickly recover the pressure loss by increasing the stress rate. To isolate the effect of pressure loss, we carried out a controlled stripping experiment (1 mAh/cm^2) where the stripping current density was increased from 0.3 to 1 mA/cm^2 with a 'hold' period of 30 minutes between each cycle (**Figure 5.3**). The effect of negative pressure due to contact loss was observed during the continuous stripping process which shows a clear dependence on current density. The average stress rate (dp/dt) was increased from 0.07 MPa/h to 0.4 MPa/h. The small increase of pressure during the 'hold' period can be attributed to the subsequent creep effect of Li which results in contact recovery (briefly discussed in Chapter 4).

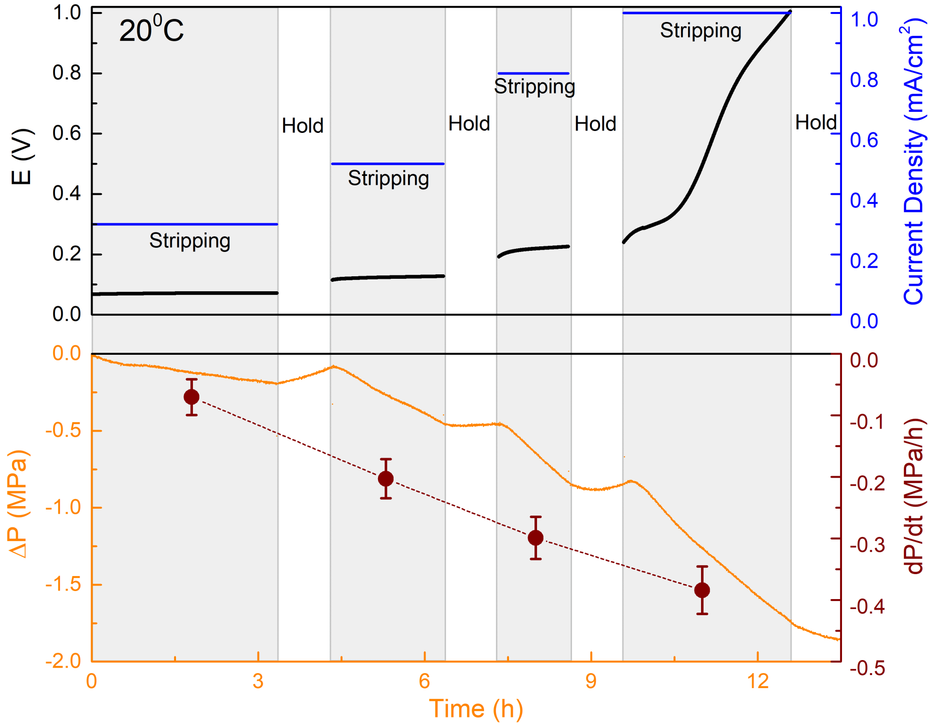

Figure 5.3: Stress response of a Li stripping test at 0.3, 0.5, 0.8 and 1 mA/cm^2. Pressure differential *(dp/dt)* was calculated for stripping at each current density.

The irregular pressure oscillation mostly disappears at the same current density when the operating temperature is increased to 65°C. Here, a gradually increasing oscillatory profile was observed after the current density was ramped to 1.5 mA/cm^2 (**Figure 5.2b**). The cell shorted at 4.2 mA/cm^2 where the stress rate reaches above 1 MPa/h. The increased stress rate for cell shorting at 65°C is due to the improved kinetics, favorable chemo-mechanics of Li metal (faster creep rate), and low charge transfer resistance. This indicates that the critical stress factor of Li|LLZO interface is dependent on temperature. Increasing the temperature facilitates a uniform internal stress balancing (positive and negative) which allows Li metal to cycle at higher current densities. A critical stress factor by measuring the differential pressure (dp/dt) can be a useful method to track the onset of cell failure.

5.3.2 Stress Response of Full cells

The operando stress measurements of a full cell configuration have been carried out extensively for aqueous Li-ion batteries (Pharr et al. (2014); Cannarella & Arnold (2014); Liu et al. (2016)). Mechanical stress evolution in electrodes can give useful insights into the state of health (SOH), capacity fade, and mechanical failure of the batteries. A small stack pressure is often employed in conventional batteries to minimize the stress evolution within confined electrodes. In an aqueous Li metal battery, a stack pressure of 350 KPa is shown to efficiently control the Li deposition morphology (Fang et al. (2021)). The pressure requirement for a solid-state Li metal battery is noticeably higher (>3 MPa) to control the void formation in Li metal (Wang et al. (2019c)). The dynamic interfacial change of Li metal can also be observed in a full cell configuration from its higher stress evolution (Koerver et al. (2018)). However, during charge-discharge, the stress evolution of a volume-constrained battery is due to the combined effect of volume change in the cathode (active material), solid electrolyte, and Li anode. The measured stress can be described via the volumetric strain of the battery constituents:

$$\delta p = -(\epsilon_{vol-cathode} + \epsilon_{vol-SE} + \epsilon_{vol-anode}).K \tag{5.1}$$

For rigid inorganic solid electrolytes, K≈K_{SE} due to the high stiffness of the solid electrolyte. Chemo-mechanical evolution of higher energy dense cathodes (e.g.; LCO or NMC) shows a substantial pressure change of a unit cell which is correlated to their pos-

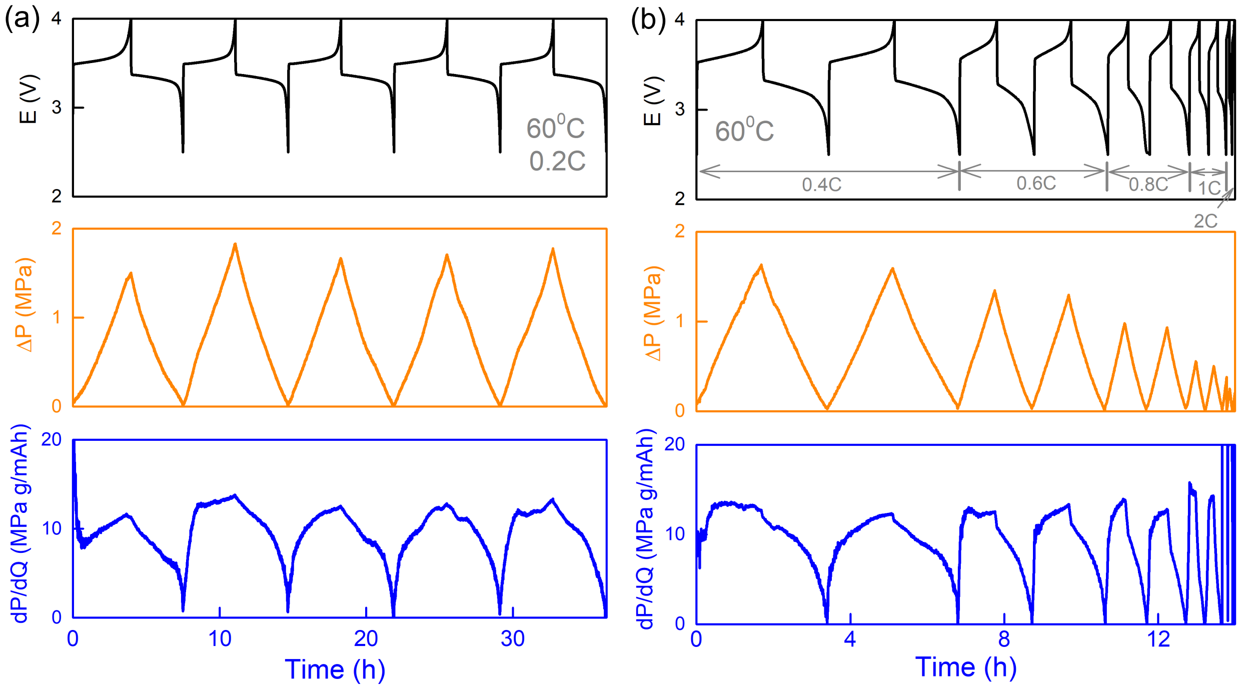

Figure 5.4: (a) Galvanostatic charge-discharge profile of a Li|LLZO|LFP full cell at 0.2C and 60°C. Stress and capacity-derivative differential pressure response of the corresponding cycles are shown below. (b) C-rate dependence of the full cell cycling at 60°C. At 2C, cell shorting was observed which was also monitored from the sudden pressure drop.

itive and negative molar volume change, respectively. In contrast, volumetric strain in LFP cathodes is minimal. LFP is a phase-transition material where the transition from the olivine phase $LiFePO_4$ to $FePO_4$ causes a triaxial strain along the three axes (a = 5.0%, b = 3.7% and c = -1.9%. As a result, the lattice experiences ≈-7% volumetric strain upon delithiation which is highly reversible (Bassett et al. (2019); Wang et al. (2005)).

We utilized an LFP composite (55% active material loading) in the full cell to monitor the stress evolution of Li metal during cycling. To avoid external pressure-related variation, the stack pressure for the operating conditions remained fixed (10 MPa). The electrochemically induced pressure change in the full cell is more or less periodic (**Figure 5.4a**). The pressure increase during charging can be correlated with the significant volume change of electrodeposited Li metal. Due to the high partial molar volume (+ve), Li exhibits a stronger volume effect which shows an increase of 1.4 MPa of pressure for an initial charging capacity of 77 mAh/g (45% lithiation). The pressure increases upon further cycling due to increasing discharge capacity. The volume effect becomes more prominent when the operating temperature was increased to 60°C. The stress profile showed a pressure variation of $\approx$ 2 MPa due to a higher volume change of Li at 60°C for a charge-discharge capacity of 140 mAh/g (83% lithiation) (**Figure 5.4a**). The coloumbic efficiency of the 1st cycle was <90% which is increased to 100% from the subsequent cycles, followed by an increase of discharge capacity. In chapter 4, we corroborated the low 1st cycle efficiency to a metastable cathode-solid electrolyte chemical interphase formation. This is also can be interpreted from the pressure profile where a higher stress rate was observed during the 1st charging cycle. We also calculated the pressure derivative of the cycles with respect to the capacity which shows a uniform pressure buildup within the stable electrochemical window of LFP (3.3-3.6V). This result clearly indicates pressure buildup in the MPa range due to Li plating on the anode which stabilizes to $\approx$1.8 MPa after the 2nd cycle.

The rate performance of all-solid-state LFP composite (at 60°C) at a low C-rate (0.2C) is relatively stable with excellent retention over multiple cycles. Here, operating temperature plays a significant role in improving the ionic transport and kinetic properties which leads to a high degree of lithiation. Hence, the corresponding stress response over multiple cycles is very similar. However, as the C-rate (current density) increased, we observed a higher stress rate during the charging and discharging process (**Figure 5.4b**). At 2C, the cell was shorted during charging. The stress profile and differential pressure (dP/dQ) profile shows over a 6-fold increase which corresponds to a substantial increment in Li-flux at the Li-LLZO interface. The morphological change in Li metal in conjunction with LLZO was visualized before where micron scale pore formation and morphological changes were observed (Dixit et al. (2020c)). Such deformation is further exacerbated at a high current density which can be traced by monitoring the variation of internal pressure. This highlights the negative aspects of the high-stress factor due to the highly heterogeneous volume change of Li metal which dictates the rate performance and cell stability of solid-state Li metal batteries.

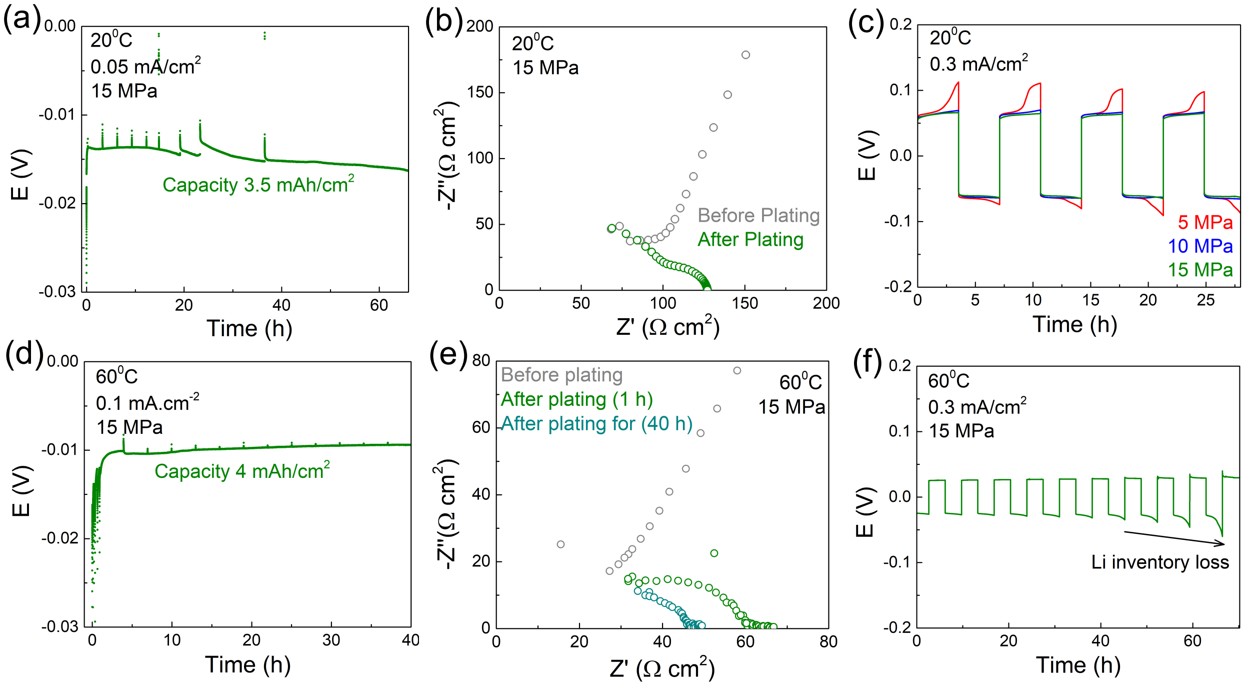

Figure 5.5: (a) Room temperature Li plating profile on a graphite foil in a Li|LLZO|Gr half-cell configuration. Around 3.5 mAh/cm^2 (18 μm thick) Li was plated. (b) Nyquist plot showing the impedance drop after plating, signifies the surface coverage of Li on a 4 mm graphite foil. (c) Stripping-plating profile of the half cell at 3 different stack pressures (5, 10 and 15 MPa). 1 mAh/cm^2 of Li was stripped and plated in each cycle. (d) Plating profile of the half cell at 60°C. (e) Nyquist plot signifying the growth of Li coverage over time. (f) Extended stripping and plating (1 mAh/cm^2) for over 60 hours, showing gradual decrease of Li loss.

5.3.3 Towards Anode-free Electrodeposition of Li

Early developed theoretical models have predicted the Li penetration susceptibility of a solid electrolyte. In reality, plating-induced Li infiltration can occur on solid electrolytes which resembles a failure following Griffith's theory of fracture (Porz et al. (2017)). The intrinsic electronic conductivity of solid electrolytes is another important criterion for Li penetration (Han et al. (2019)). For anode-free approaches, the complexity associated with uniform Li plating further intensifies. As there are no structural hosts present on the anodic side, in-situ Li plating becomes highly dependent on the nature of the current collector. Li nucleation and growth on a current collector are extremely critical which affect the overall electrochemical performance of the anode-free systems. From a mechanistic perspective, the Li plating process generates significantly higher compressive stress as there is no bulk Li reservoir available to initiate any stress relaxation mechanism. In general, the overall plating process can be divided into 4 stages: nucleation, densification, growth, and coalescence (Adair et al. (2020)). For stable plating, the growth of lateral or vertical Li needs to be plastically deformed to cover the surface area of the current collector. Hence, an ideal current collector for anode-free batteries should exhibit high Li solubility and adhesion properties. In conventional Li-ion batteries, copper foil is widely used as the current collector. However, several technical challenges are associated with laminating a copper foil on a rigid solid electrolyte (e.g.; LLZO) which is cost sensitive (Wang et al. (2021c)).

Here, we utilized the high electronic conductivity of a wrinkled graphite foil to employ it as a current collector. The ion-blocking nature of the graphite foil gives a high initial interfacial impedance during EIS measurement in a half-cell configuration (**Figure 5.5b**). The initial open-circuit voltage (OCV) was ≈1.5V. To avoid irregular Li deposition-induced shorting of LLZO, Li was plated at a lower current density (0.05 mA/cm^2) at room temperature. The plating profile shows a typical negative overpotential at the beginning of plating which corresponds to the nucleation of Li deposits on the graphite foil (**Figure 5.5a**). As the plating proceeds, more Li is accumulated on the seeds which lead to stable growth of Li. Intermittent EIS was taken to track the decrease in cell resistance (**Figure 5.5b**). The Nyquist plots showed a faster decline of interfacial resistance which corresponds to numerous Li nuclei growth on the graphite surface. After depositing a total of 3.5 mAh/cm^2 of Li, which corresponds to a thickness of ≈18 μm, we evaluated the cycling performance of the 'as-prepared' symmetric cell with respect to stack pressure. Here, the accumulated Li on graphite acts as an inventory for subsequent cycling. The cycling of the electroplated Li shows a stack pressure dependence during stripping and plating of 1 mAh/cm^2 Li at 0.3 mA/cm^2. As observed in a Li|LLZO|Li symmetric cell, low stack pressure (5 MPa) leads to a gradual polarization which corresponds to void formations and contact loss on Li|LLZO interface (**Figure 5.5c**). A stable cycling performance was observed when the stack pressure was increased to 10-15 MPa. This indicates that the in-situ plated Li film also undergoes morphological transformations during stripping which can be suppressed by applying an optimum stack pressure.

We also carried out a similar *in-situ* Li plating measurement on graphite foil at 60°C to understand the plating morphologies of Li at higher temperatures (**Figure 5.5d**). In liquid electrolytes, increasing the temperature results in the growth of large Li nuclei which readily coalesces with the neighboring nuclei to converge into a uniform film (Yan et al. (2019)). We observed a similar favorable growth mechanism on LLZO where a low nucleation overpotential was observed. Due to low charge transfer resistance, Li could be plated at a higher current density (0.1 mA.cm2 than that at 20°C. However, we saw a continuous decrease in the plating potential as more Li was plated (4 mAh/cm^2). Intermittent EIS measurements shows a slower coverage of Li on the graphite substrate at 60°C (**Figure 5.5e**). A possible explanation can be due to the more vertical growth of Li deposits (rather than lateral) at the initial stage. For extended cycling of 1 mAh/cm^2, a growing overpotential was observed during the plating process (after the 7th cycle) (**Figure 5.5f**). Within 10 cycles, the cell potential reaches 700 mV, which signifies a gradual loss in Li inventory at graphite. This loss can be attributed to 'dead' Li formation and intrinsic reaction between Li-graphite which is more prominent at increasing temperature. We hypothesized that the initial layer of deposited Li reacts with graphite to create a seed layer of LiC_6, followed by additional growth of fresh Li which can be cycled in anode-free configurations. This further implicates that the highly reactive nature of Li possesses significant challenges in anode-free architectures. A non-reactive or conversion-free (passivation) nature of the current collector is, therefore, preferred to resolve the chemomechanical issues associated with uniform plating.

5.4 Conclusion

The implication of Li metal in solid-state batteries possesses significant challenges on a cell level. This is largely due to the highly anisotropic volume change of bulk and interfacial Li. In this chapter, we emphasize the critical role of chemo-mechanically induced volume change of Li metal in a solid-state battery. With the aid of an operando stress monitoring system, we evaluated the unavoidable and dynamic internal pressure change in a Li-metal solid-state system. We corroborated that maintaining internal stress buildup below the critical stress rate is essential to prevent plating-induced shorting of cells. By employing a "low-strain" composite cathode (LFP), we assessed the stress evolution in full cells, which shows MPa range of pressure buildup. This further highlights the necessity of minimizing the volume change in Li metal for practical solid-state batteries. An excellent strategy would be to eliminate the use of Li anode (excess Li) and adopt an anode-free approach where Li is plated *in-situ* from the cathodes. Here, we demonstrate a feasible approach of using a non-conventional current collector (Graphite foil) for garnet LLZO electrolytes. We showed that Li can be plated to form a few micron thick layer which can be cycled back at 0.3 mA/cm^2 under different operating temperatures. However, the reactive nature of graphite foil complicates the reversibility of anode-free plating for extended cycling which requires further surface modifications. Controlling the growth and deposition of Li in confined domains of current collectors can facilitate smaller volume change and higher utilization of plated Li. Hence, a stable, non-reactive current collector of high surface area can significantly increase the rate performance of anode-free solid-state batteries.

Chapter 6

Summary and Conclusions

6.1 Summary

This work aims to briefly understand the complex transport phenomena of solid electrolytes and Li metal in solid-state batteries that dictates the stability and cycling performances. Interfaces within a solid-state battery consistently evolve during electrochemical cycling. Understanding the coupled electrochemical and chemomechanical phenomena at dynamic interfaces is crucial for the rational designing of solid-state architectures for higher energy density and durability.

Due to its relatively higher chemical stability, garnet oxide solid electrolytes are ideal model systems for studying the structure-function relationships which govern the electro-chemo-mechanical transformations of solid-state batteries. We briefly employed garnet LLZO and its hybrid derivatives in this work and elucidated two types of interfaces that exist in solid-state batteries. In Chapter 3, we investigated the role of intrinsic interfacial factors that control the transport mechanisms of hybrid polymer-ceramic solid electrolytes (PEO-LLZO). Hybrid electrolytes were prepared by using the conventional tape-casting method. The addition of ion-conducting fillers in PEO inhibits the crystallization kinetics and enhances the ion transport properties. A direct increase in transference number upon increasing loading indicates strong Lewis acid interactions between LLZO and anions in PEO. However, an optimum loading of LLZO particle was observed, beyond which ionic conductivity of the electrolytes drastically decreases. With the aid of advanced synchrotron X-ray nanotomography, we visualized and quantitatively assessed the structural heterogeneity of LLZO distribution within the polymer (PEO) matrix. The high spatial resolution (50 nm) of nanotomography enables the identification of the extent of particle dispersion and subsequent agglomerations. We found that the agglomerate formations highly depend on the percolated volume of ceramic particles in colloidal suspensions. LLZO particles tend to form dense clusters at high volumetric loading which experience strong electrostatic interactions within neighboring particles. Electrochemical experiments revealed that the ionic conductivity of such electrolytes decreases to almost 2 orders of magnitude. Hence, the theoretical prediction of improved percolation pathways at a high particle-to-polymer ratio is overestimated. From X-ray imaging, we quantified the active particle surface area and found a significant decrease in accessible surfaces when ceramic loading is the highest (50 vol%). The accessible surface area was also found to be the highest at the optimal ceramic loading (15 vol%) for the highest ionic conductivity. In conjunction with continuum percolation modeling, we hypothesized a surface-driven ion transport mechanism that is facilitated by the interfacial regions of particle-polymer. This work highlights the significance of strong particle-polymer interaction for providing abundant percolation pathways for ion transport. Novel processing techniques should address and resolve the key issues associated with control over interfacial regions of hybrid solid electrolytes.

In Chapter 4, the electrode|electrolyte chemomechanics on a cell level are explored. We focused on the dynamic interfacial evolution of Li metal against garnet electrolytes. Unlike the contemporary solid electrolytes such as sulfides, phosphates, and halides, LLZO showed excellent chemical and thermal stability against Li metal. However, the intrinsic lithiophilicity of LLZO is often restricted by the surface carbonate layers which are insulating. Here, we optimized the processing of LLZO to provide a carbonate-free surface with dense (>98%) microstructures. As a result, Li readily wets on LLZO and can be tailored to provide a conformal interfacial contact. We demonstrated a mechanism for achieving ultra-low ($<3\ \Omega\ \mathrm{cm}^2$) interfacial resistance which allows us to achieve a high critical current density ($>1\ \mathrm{mA/cm}^2$ at room temperature). However, void formation during Li stripping frequently occurs and this results in significant polarization. A higher degree of voids increases the local current density at the interfaces and leads to immediate short-circuiting and cell death. Stack pressure is an effective strategy to increase the diffusivity of bulk Li upon depletion. We employed a 3-electrode setup for solid-state symmetric cells to effectively isolate the stripping mechanism under stack pressure. We found that creep plays a dominant role during the electro-dissolution process as the stress-assisted diffusivity of Li continuously fills up the voids. The effect of creep is systematically evaluated with respect to the initial contact resistance, current density, stack pressure, and temperature. When the initial contact resistance is very low, the Li stripping process shows negligible polarization and pressure-induced Li creep plays a minor role in contact improvement. However, poor initial contact leads to a further exacerbated interface and high polarization where the significance of creep is more prominent. Similar phenomena were observed with respect to different stack pressures (5-15 MPa) and current densities (0.3-0.8 mA/cm^2). However, a complete recovery of Li due to creep was not achievable which signifies a permanent voiding in the interface that can not be replenished. The "non-recovered" regions are formed due to local interfacial asperities where the yield stress of Li can be significantly higher than that of bulk Li. In general, at least 15 MPa of stack pressure is required to obtain a stable stripping profile which is irrespective of the current density. This further highlights the importance of optimum stack pressure in enabling Li metal anode for stable battery operations. We also investigated the significance of stack pressure in controlling the morphology of Li plating at high current densities. While the effect is minimal, the inability to maintain local contact points at the plating side causes an irregular and isolated Li plating that leads to cell shorting. A modified operating condition by raising the temperature here is preferred, where more favorable chemomechanics of Li can enable stable deposition of a large amount of Li (5 mAh/cm^2).

The impact of stack pressure and temperature is also investigated in full cells. All solid-state composite cathode (LFP) was employed to understand the interfacial limitations that dictate the cyclability and rate performances. Unlike Li anode, the impact of stack pressure in cathodic charge transport is minimal. However, higher stack pressure (>10 MPa) is necessary for preventing electrode delamination which aids in achieving better retention properties. The rate performance of the full cell is noticeably increased at high temperatures due to improved kinetics of the cathode (and anode). We identified the presence of a metastable cathode|electrolyte interphase in all cases which readily forms during the first charging cycle. Although this may not be a rate-limiting factor, avoiding any resistive interphase growth is generally preferred for long-term battery cycling. The cell shorting behavior of a full cell is further investigated by employing a thick cathode with high areal capacity. Unlike symmetric cells, shorting in full cells is reversible where dendrites within a solid electrolyte can be healed by slow discharging. This work summarizes the interfacial and transport limitations that exist in Li-metal solid-state batteries which must be resolved for high-performing systems.

Finally, in chapter 5, we conducted a quantitative assessment of volume changes during Li electrodeposition in solid-state batteries. Pressure-related phenomena discussed in chapter 4 were based on a constant pressure system. Herein, we evaluated the intrinsic pressure buildup in a cell by monitoring the dynamic stress responses in symmetric and full cells. Operando pressure evolution in a battery provides useful insights into the bulk volume expansion and contraction of electrodes. In symmetric cell configurations, a faster rate of pressure loss (-ve) was observed when Li is depleted away from the interface. The pressure buildup on the plating side is a relatively slow process. The pressure difference on both sides corresponds to the molar volume mismatch between two Li electrodes. A critical stress factor (*dp/dt*) was identified for both cases which is synchronous to the current density. A lower stress factor for plating depicts a slow nucleation-growth rate of Li which results in uniform deposition of Li. However, faster nucleation leads to a high-stress factor that can not undergo post-growth relaxation. As a result, the void-mitigation process is affected significantly which initiates the formation and propagation of Li dendrites. From a mechanistic perspective, this can be prevented by minimizing the pressure loss during Li depletion. More balanced stress response was observed when a similar experiment was carried out at a higher temperature. Here, initial stress buildup on bulk Li is quickly mitigated due to improved kinetics and the high creep rate of Li. The origin and evolution of stress factors are further investigated in full cells. We observed significantly higher and incremental pressure buildups upon Li plating. When the C-rate (current density) is increased, the stress factor synchronously increases. Capacity-derivative differential pressure (*dP/dQ*) analysis reveals a higher stress rate during the initial stages of charging. If the Li plating rate is further increased, the corresponding stress factor experiences >5X increase which also can initiate cell shorting. Operando pressure monitoring is an effective analytical tool to track the chemo-mechanical evolution related to heterogeneous volume changes in Li. Lastly, we extended our knowledge of complex Li deposition mechanisms for an anode-free approach. We employed pristine graphite foils as current collectors in half-cell configurations to understand the plating morphologies at different temperatures. A good interfacial bond between the current collector and solid electrolyte is mandatory for enabling lower Li nucleation potential and stable deposition. Upon creating a Li reservoir by *in-situ* plating, we demonstrated stable stripping/plating profiles at 0.3 mA/cm^2 for both 20°C and 60°C. However, the low reversibility or coloumbic efficiency for prolonged cycling of anode-free solid-state systems requires a chemically stable current collector for controlled Li deposition.

6.2 Conclusion

All-solid-state Li-metal batteries can potentially deliver unprecedented energy densities with utmost safety and reliability which are highly desired features for future EV and consumer electronic applications. A myriad of unique battery chemistries has been developed over the last two decades, which signifies major progress in novel battery technology development. However, high-performance solid-state batteries also require a broad understanding of the complex transport phenomena and interfacial challenges that are still halting its transition from lab-scale towards scalable mass production. In this work, we briefly investigated these various aspects of interfaces in solid-state Li metal batteries. With the aid of advanced imaging and analytical techniques, we explored the underlying structure-function dependence of solid electrolytes and the chemomechanical evolution of solid electrodes which can be leveraged toward developing high-performing batteries. The findings of this work are expected to expand our knowledge on battery construction, operation, failures, and various performance limiting factors. We hope our efforts in this work will help in developing novel and rational designing of battery architectures for scalable production.

Appendix A

Supporting Information: Chapter 3

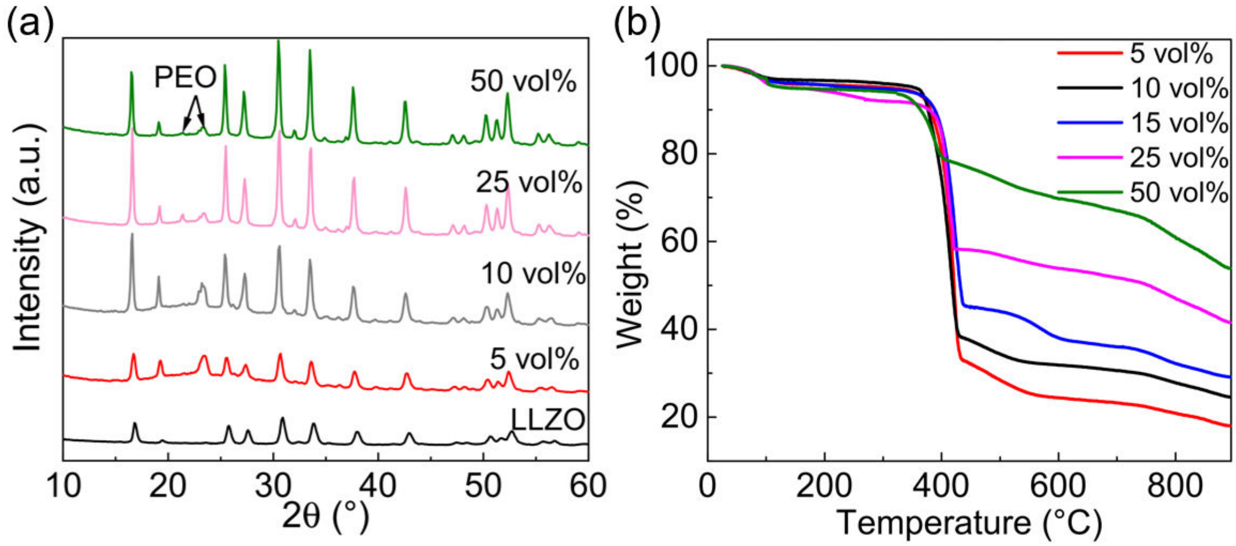

Figure 1.1: (a) XRD and (b) TGA of PEO-LLZO electrolytes at different loading

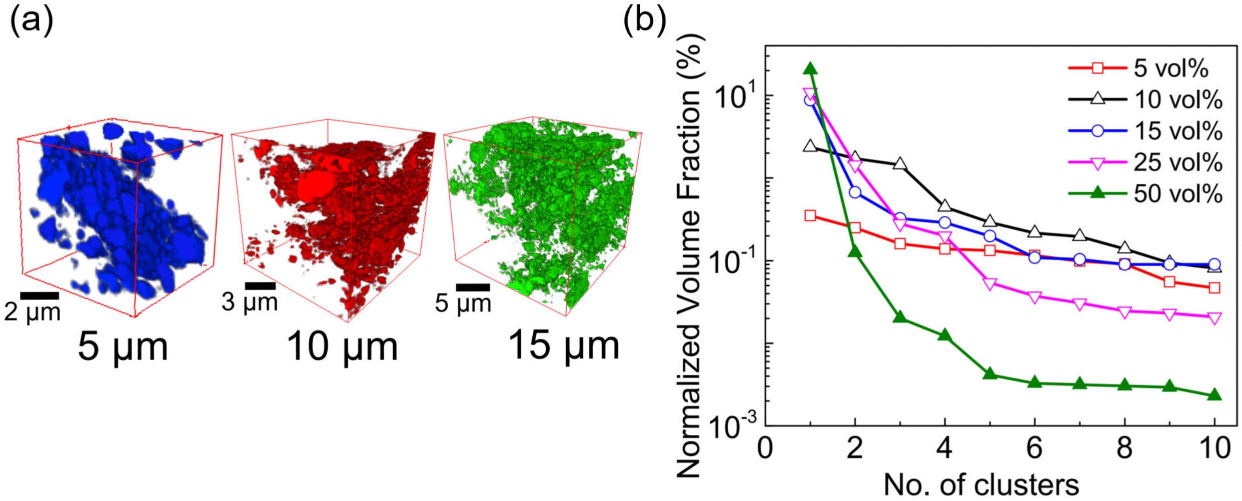

Figure 1.2: (a) Reconstructed images at 5, 10 and 15 μm sub-volume and (b) normalized area of 10 largest clusters

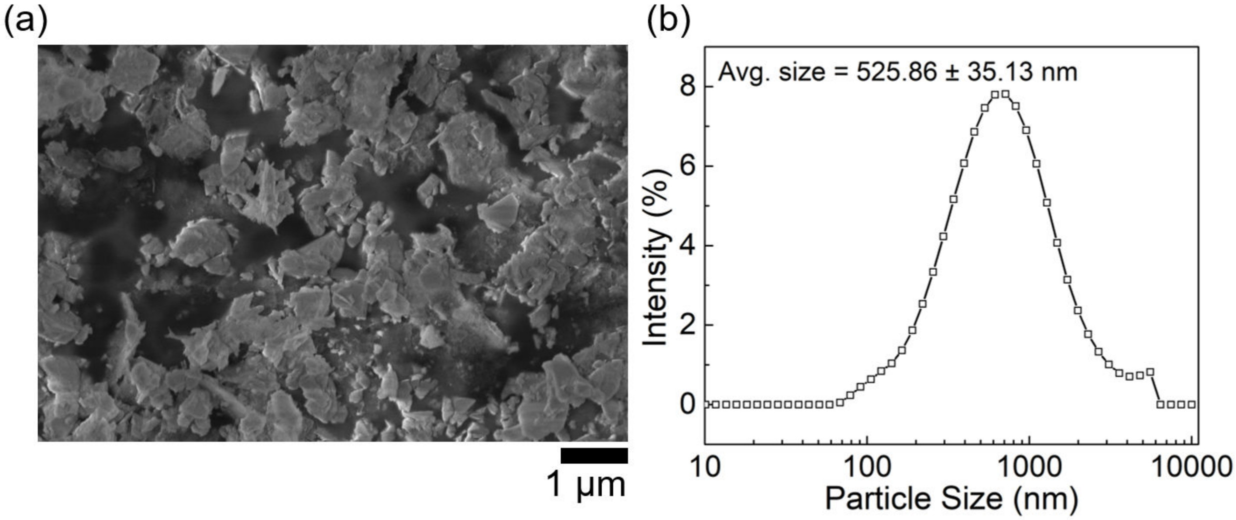

Figure 1.3: (a) SEM image of Al-LLZO powder and (b) LLZO particle size distribution from dynamic light scattering (DLS)

1.0.1 Code for Surface Area Calculation

```
clc;

clear all;

fname = ’3dimages/10vol/10vol_300x300_binary. tif’;

info = imfinfo(fname);

num_images = numel(info);

for k = 1:num_images

A(:,:,k) = imread (fname, k, ’Info’, info);

A_perimeter = bwperim(A,8);

savestack(A_perimeter,’Test_15_perimeter.tif’)

Area = sum(sum(sum(A_perimeter)));

Volume = sum(sum(sum(A)));

SAtoVolume = Area/Volume
```

```
imshow(A(:,:,1))
figure()
imshow(A_perimeter(:,:,1))
end
```

1.0.2 Code for Particle Cluster Calculation

```
clc;
clear all;
fname = ’10% vol loading.tif’;
info = imfinfo(fname);
num_images = numel(info);
for k = 1:num_images
A(:,:,k) = imread(fname, k, ’Info’, info);
end
[labeledImage, numberOfBlobs] = bwlabeln(A,26);
blobMeasurements = regionprops(labeledImage, ’area’);
allAreas = [blobMeasurements.Area];
[sortedAreas, sortIndexes] = sort(allAreas, ’descend’);
biggestBlob1 = ismember(labeledImage, sortIndexes(1));
biggestBlob2 = ismember(labeledImage, sortIndexes(2));
biggestBlob3 = ismember(labeledImage, sortIndexes(3));
biggestBlob4 = ismember(labeledImage, sortIndexes(4));
```

```
biggestBlob5 = ismember(labeledImage, sortIndexes(5));

for ii = 1 : size(biggestBlob1, 3)

biggestBlobRGB1(:,:,:,ii) = label2rgb(biggestBlob1(:,:,ii),’parula’,’k’);

biggestBlobRGB2(:,:,:,ii) = label2rgb(biggestBlob2(:,:,ii),’jet’,’k’);

biggestBlobRGB3(:,:,:,ii) = label2rgb(biggestBlob3(:,:,ii),’hsv’,’k’);

biggestBlobRGB4(:,:,:,ii) = label2rgb(biggestBlob4(:,:,ii),’hot’,’k’);

biggestBlobRGB5(:,:,:,ii) = label2rgb(biggestBlob5(:,:,ii),’cool’,’k’);

end

biggestBlobRGB = biggestBlobRGB1+biggestBlobRGB2+biggestBlobRGB3 +biggestBlobRGB4+biggestBlobRGB5;

savestack(biggestBlobRGB,’50% vol loading_Connected.tif’)

end
```

Appendix B

Supporting Information: Chapter 4

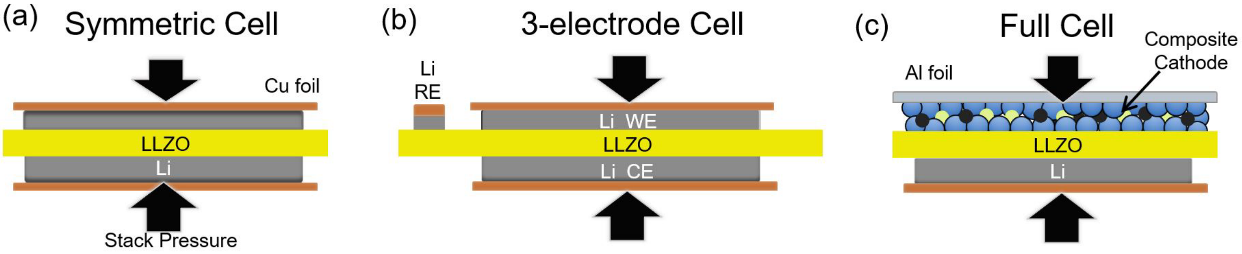

Figure 2.1: Schematic of the solid-state cell types used in this work, (a) symmetric cell, (b) 3-electrode symmetric cell with Li foil as reference electrode and (c) full cell with composite cathode (LFP).

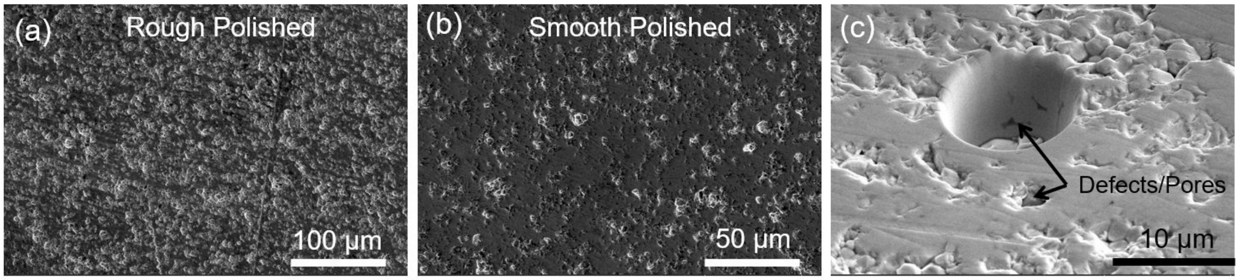

Figure 2.2: SEM images of LLZo showing of (a) rough surface LLZO and (b) smooth surface. (c) SEM image of a FIB section of LLZO, showing microstructural pores.

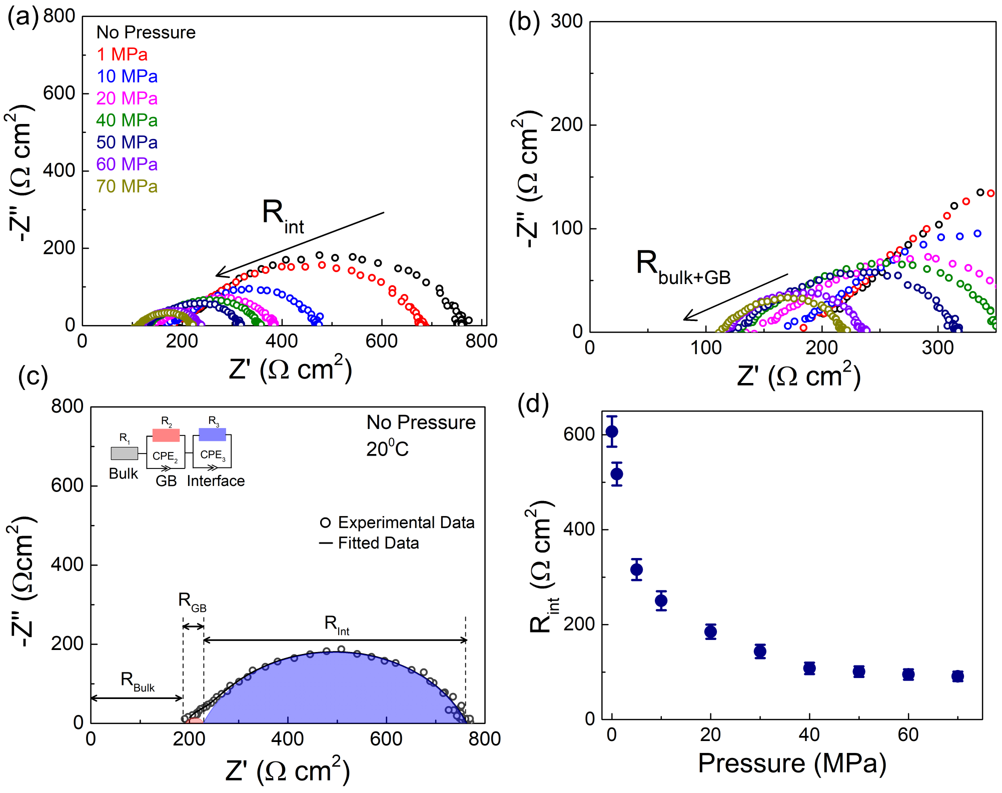

Figure 2.3: (a) Nyquist plots showing stack pressure dependence on interfacial resistance of Li-LLZO. (b) Zoomed in plot of (a) highlighting the change in bulk resistance, indicating Li electrode area expansion. (c) EIS spectra fitting and (d) change in interfacial resistance with respect to pressure.

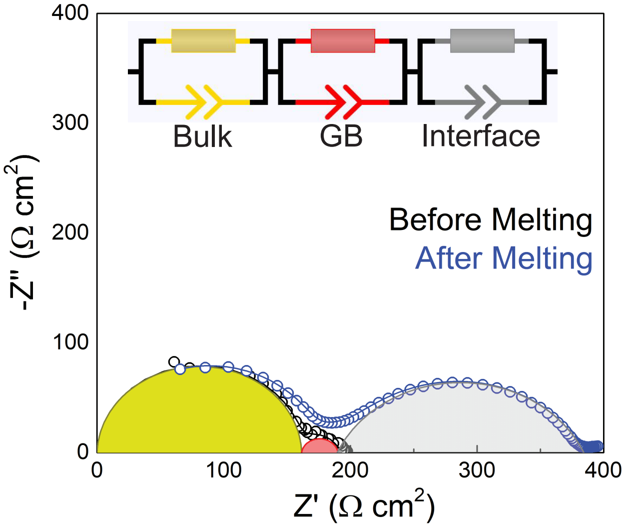

Figure 2.4: Nyquist plot showing negligible (≈ 0Ω.cm^2) of interfacial resistance after heat-treatment at 220°C.

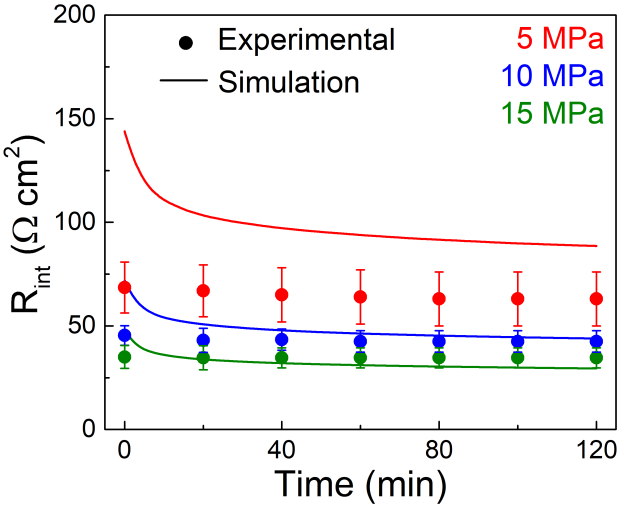

Figure 2.5: Stack pressure and subsequent time-dependent creep (pure) effect on a Li|LLZO interface at 5, 10 and 15 MPa. Li was attached on LLZO pellet and no electrochemistry was conducted. Simulation was carried out on model LLZO surface.

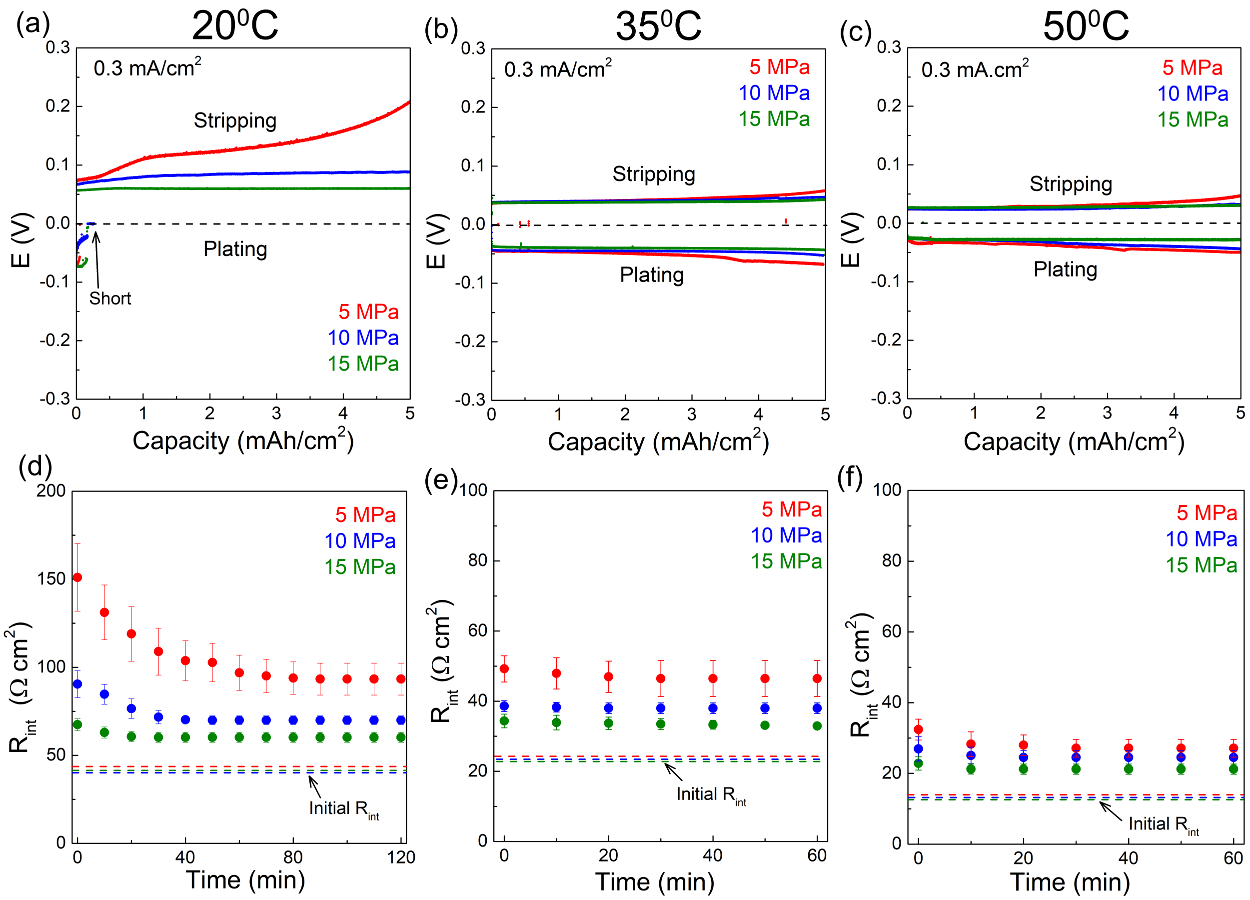

Figure 2.6: In a 2-electrode setup, stripping and plating profile of a Li|LLZO|Li symmetric cell at 5,10 and 15 MPa at (a) 20°C, (b) 35°C and (c) 50°C. During post-strip hold, change in interfacial resistance due to Li creep at (d) 20°C, (e) 35°C and (f) 50°C.

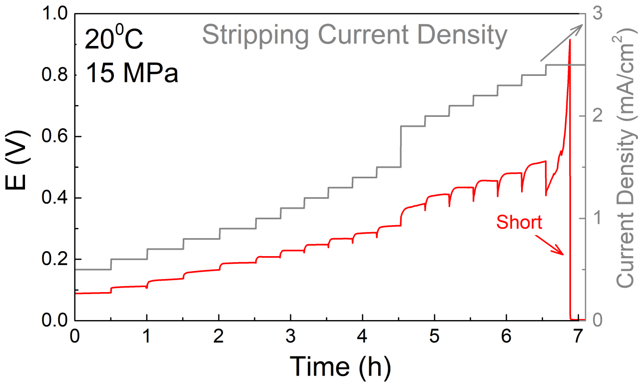

Figure 2.7: Critical 'stripping' current density measurement of Li|LLZO|Li symmetric cell at room temperature. This demonstrates that Li can be stripped at a substantial higher current density than the typical current density limit of LLZO. It should be noted that at the end of each stripping/plating period, a resting period of 15 minutes was introduced in the measurement protocol to allow Li creep.

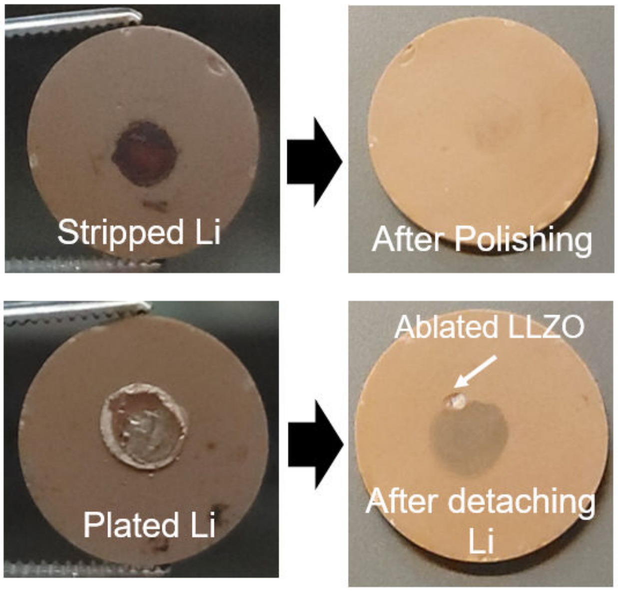

Figure 2.8: Snapshot of stripped and plated LLZO.

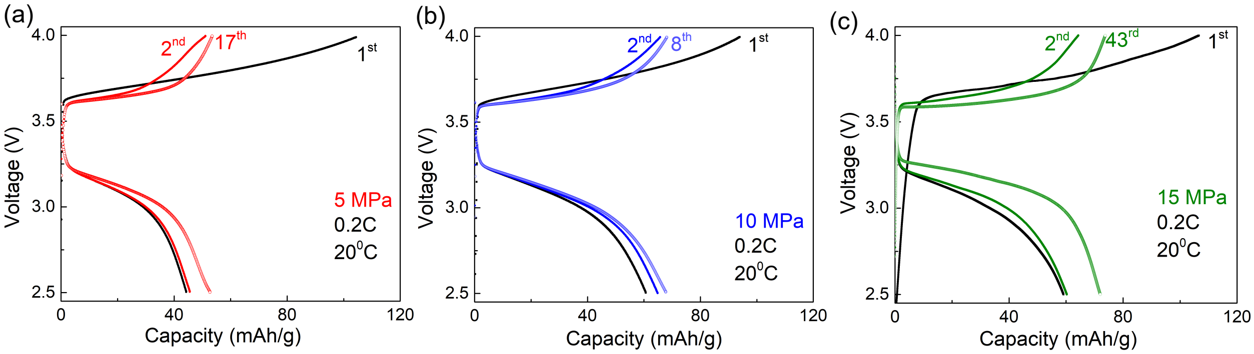

Figure 2.9: Charge/discharge curves of Li|LLZO|LFP full cells at 20°C and 0.2C under (a) 5 MPa, (b) 10 MPa and (c) 15 MPa of stack pressure.

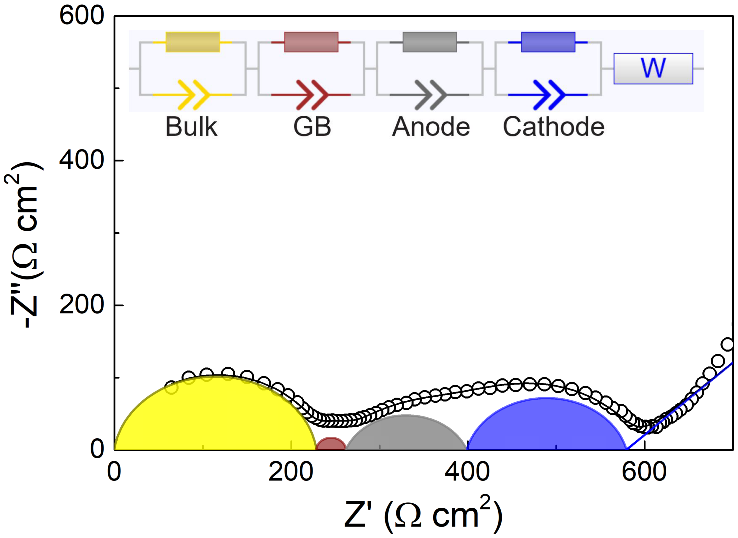

Figure 2.10: EIS fitting of a full cell. Deconvolution of the spectra shows resistance from bulk, grain boundary, anodic interface and cathodic interface.

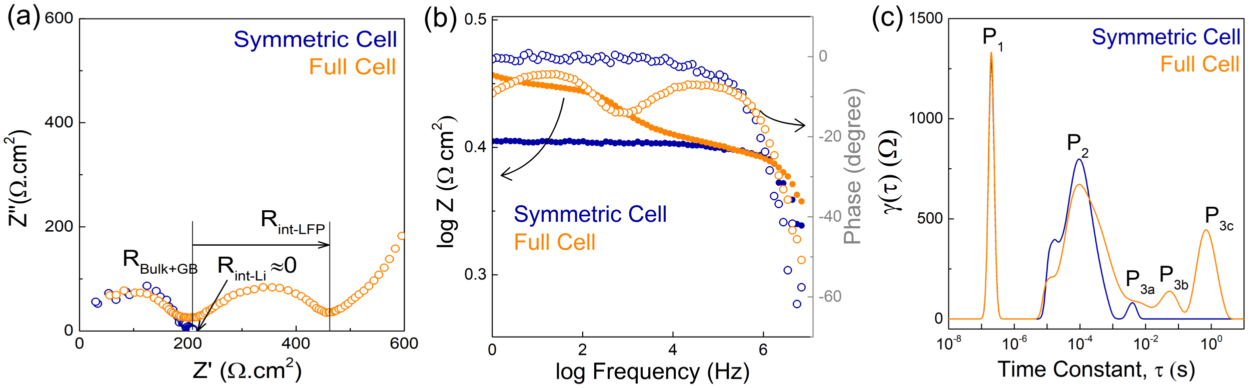

Figure 2.11: Room temperature Nyquist plot of a symmetric and full cell, (b) corresponding Bode plots and (c) DRT curves.

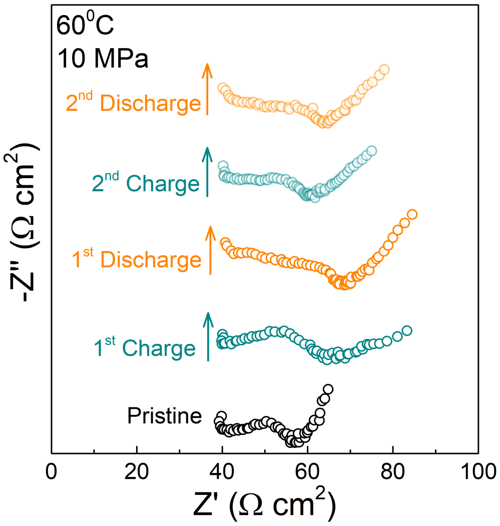

Figure 2.12: Nyquist plots of a full cell showing interfacial impedance evolution during charging and discharging (C-rate 0.4) at 60°C.

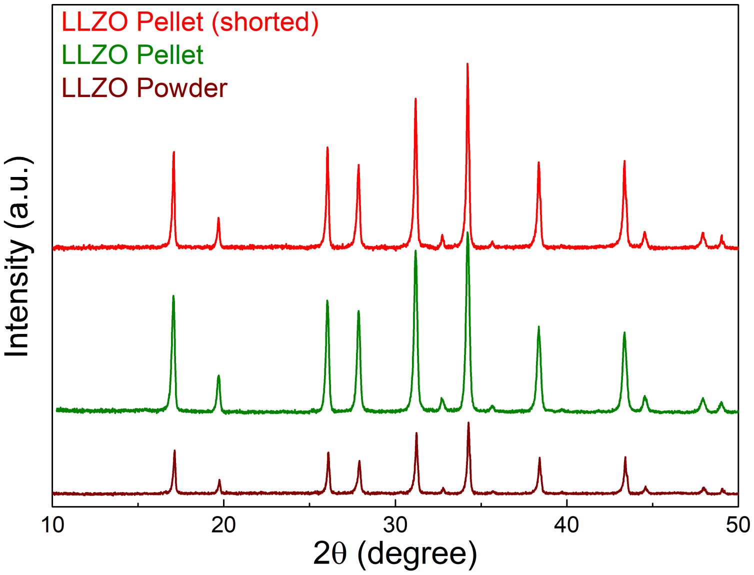

Figure 2.13: X-ray diffraction results of cubic LLZO powder, LLZO pellet and LLZO pellet (shorted).

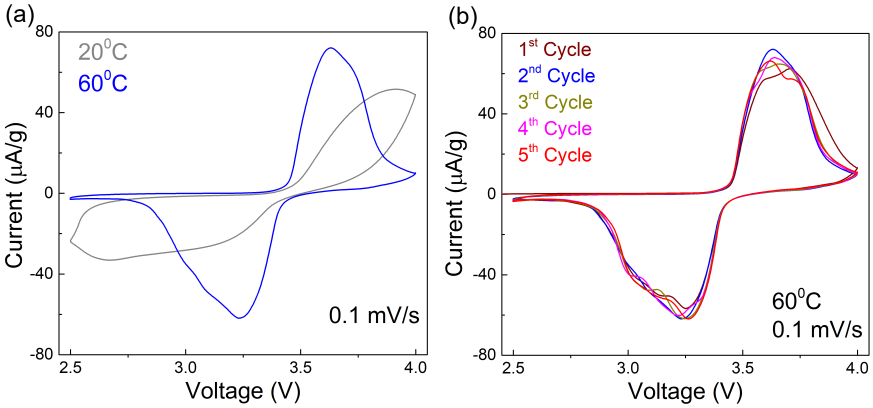

Figure 2.14: (a) Cyclic voltammetry (CV) comparison of LFP|LLZO|Li full cells at 20°C and 60°C. (b) CV plot of full cells over multiple cycles at 60°C.

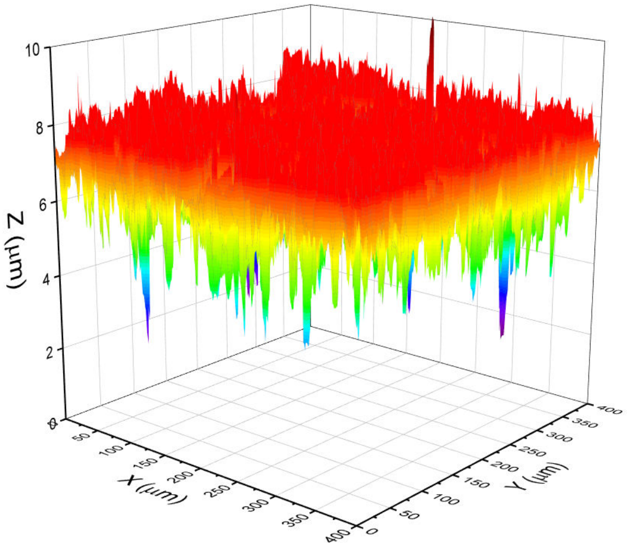

Figure 2.15: 3D surface mapping of polished LLZO surface.

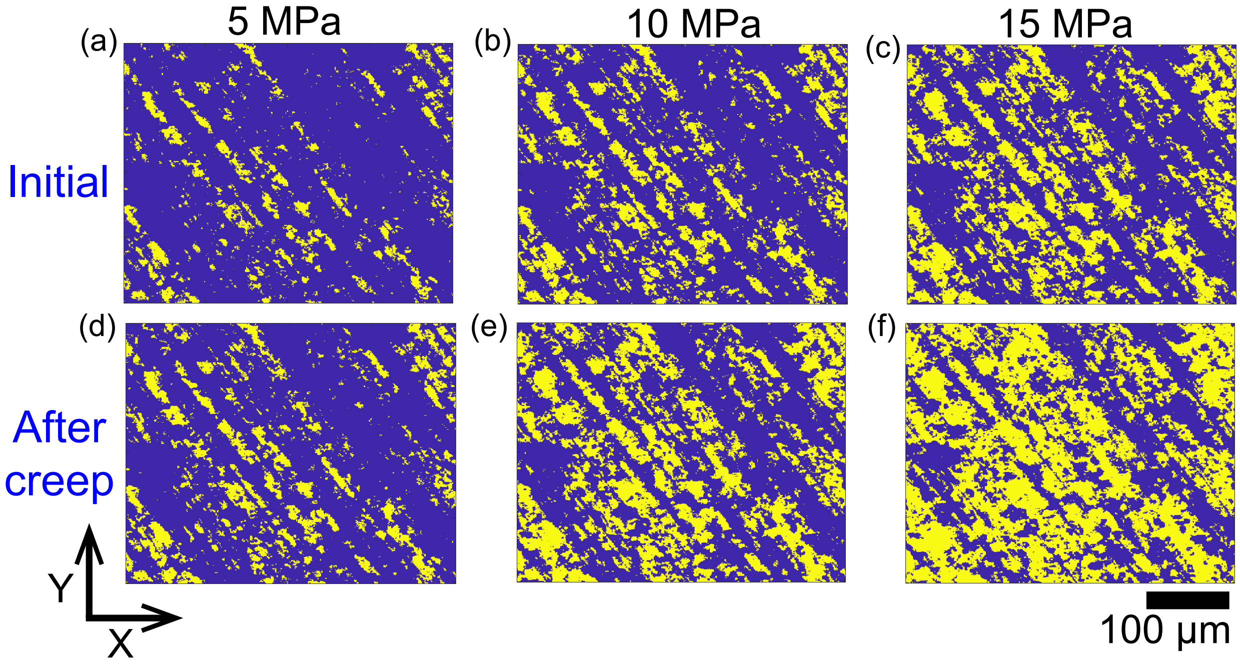

Figure 2.16: Contact map of Li-LLZO interface after applying stack pressure of (a) 5 MPa, (b) 10 MPa and (C) 15 MPa. Corresponding contact maps of the same interfaces after pure creep of Li at (c) 5 MPa, (d) 10 MPa and (e) 15 MPa. Yellow represents contact regions and blue represents non-contact regions in the plots.

Appendix C

Supporting Information: Chapter 5

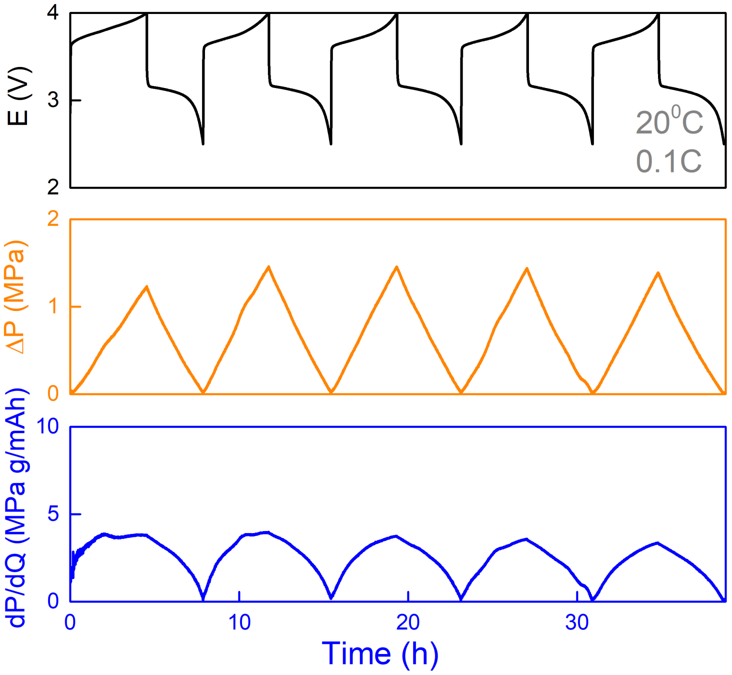

Figure 3.1: Stress evolution and differential pressure (dP/dQ) profile of a Li|LLZO|LFP full cell cycling at 20°C.

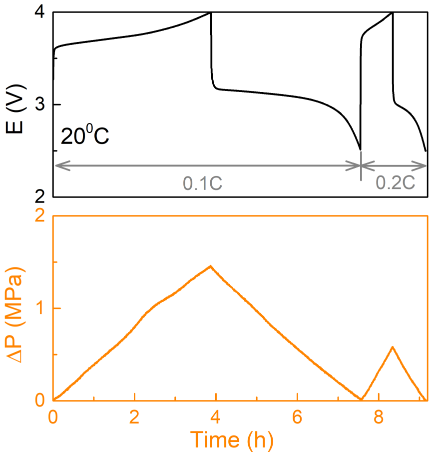

Figure 3.2: Stress evolution of a full cell at 0.1C and 0.2C (20°C).

REFERENCES

Adair K. R., Banis M. N., Zhao Y., Bond T., Li R., Sun X., 2020, Advanced Materials, 2002550, 2002550

Administration U. S. E. I., 2022, 2022

Åhman M., Nilsson L. J., Johansson B., 2017, Climate Policy, 17, 5, 634

Ahn D. B., Lee K. H., Lee S. Y., 2022, Current Opinion in Electrochemistry, 32, 100889

Al L., Po T., 2018, 6, 1055

Albertus P., Anandan V., Ban C., et al., 2021, ACS Energy Letters, 6, 4, 1399

Albertus P., Babinec S., Litzelman S., Newman A., 2018, Nature Energy, 3, 1, 16

Armand M., 1983a, Solid State Ionics, 10, 745

Armand M., 1983b, Solid State Ionics, 9, 745

Asano T., Sakai A., Ouchi S., Sakaida M., Miyazaki A., Hasegawa S., 2018, Advanced Materials, 30, 44, 1

Ashby D. S., Choi C. S., Edwards M. A., Talin A. A., White H. S., Dunn B. S., 2020, ACS Applied Energy Materials, 3, 9, 8402

Asif M., Muneer T., 2007, Renewable and Sustainable Energy Reviews, 11, 7, 1388

Azhari L., Bong S., Ma X., Wang Y., 2020, Matter, 3, 6, 1845

Aziz S. B., Woo T. J., Kadir M. F., Ahmed H. M., 2018, Journal of Science: Advanced Materials and Devices, 3, 1, 1

Bae J., Li Y., Zhang J., et al., 2018, 78712, 2096

Bai P., Li J., Brushett F. R., Bazant M. Z., 2016, Energy and Environmental Science, 9, 10, 3221

Balaish M., Gonzalez-Rosillo J. C., Kim K. J., Zhu Y., Hood Z. D., Rupp J. L., 2021, Nature Energy, 6, 3, 227

Banerjee A., Wang X., Fang C., Wu E. A., Meng Y. S., 2020, Chemical Reviews

Barai P., Fister T., Liang Y., et al., 2021, Chemistry of Materials, 12

Bartsch T., Strauss F., Hatsukade T., et al., 2018, ACS Energy Letters, 3, 10, 2539

Bassett K. L., Özgür Çapraz Ö., Özdogru B., Gewirth A. A., Sottos N. R., 2019, Journal of The Electrochemical Society, 166, 12, A2707

BloombergNEF, 2021, 2021

Bolsen T., Leeper T. J., Shapiro M. A., 2014, American Politics Research, 42, 1, 65

Bonnick P., Niitani K., Nose M., Suto K., Arthur T. S., Muldoon J., 2019, Journal of Materials Chemistry A, 7, 42, 24173

Brand C., Boardman B., 2008, Energy Policy, 36, 1, 224

Bruce P. G., West A. R., 1982, Journal of Solid State Chemistry, 44, 3, 354

Buannic L., Naviroj M., Miller S. M., Zagorski J., Faber K. T., Llordés A., 2019, Journal of the American Ceramic Society, 102, 3, 1021

Cannarella J., Arnold C. B., 2014, Journal of Power Sources, 245, 745

Carlo F. D., Xiao X., Jacobsen C., 2014, Journal of Synchrotron Radiation, 21, 1188

Chang W., May R., Wang M., et al., 2021, Nature Communications, 6369, 1

Chen C.-F., Barai P., Mukherjee P. P., 2016, Current Opinion in Chemical Engineering, 13, 82

Chen F., Yang D., Zha W., et al., 2017a, Electrochimica Acta, 258, 1106

Chen H., Yang Y., Boyle D. T., et al., 2021a, Nature Energy, 6, August

Chen K. H., Namkoong M. J., Goel V., et al., 2020a, Journal of Power Sources, 471, May, 228475

Chen K. H., Wood K. N., Kazyak E., et al., 2017b, Journal of Materials Chemistry A, 5, 23, 11671

Chen R., Nolan A. M., Lu J., et al., 2020b, Joule, 4, 4, 812

Chen S., Nie Z., Tian F., et al., 2022, 2113318, 1

Chen S., Zhang J., Nie L., et al., 2021b, Advanced Materials, 33, 1, 1

Chen S., Zhang J., Nie L., et al., 2021c, Advanced Materials, 33, 1, 1

Chen X., Vereecken P. M., 2019, Advanced Materials Interfaces, 6, 1, 1

Chen X. C., Liu X., Samuthira Pandian A., Lou K., Delnick F. M., Dudney N. J., 2019, ACS Energy Letters, 4, 1080

Chen Y., Wang Z., Li X., et al., 2020c, Nature, 578, 7794, 251

Cheng L., Chen W., Kunz M., et al., 2015, ACS Applied Materials and Interfaces, 7, 3, 2073

Cheng X. B., Zhang R., Zhao C. Z., Zhang Q., 2017, Chemical Reviews, 117, 15, 10403

Choi S.-J., Lee S.-H., Ha Y.-C., et al., 2018, Journal of The Electrochemical Society, 165, 5, A957

Combustion F. F., 2015

Connell J. G., Fuchs T., Hartmann H., et al., 2020, Chemistry of Materials

Croce F., Appetecchi G., Persi L., Scrosati B., 1998, Nature, 394, 6692, 456

Cronau M., Szabo M., König C., Wassermann T. B., Roling B., 2021, ACS Energy Letters, 3072–3077

Culver S. P., Koerver R., Zeier W. G., Janek J., 2019, Advanced Energy Materials, 1900626, 1

Davis A. L., Kazyak E., Liao D. W., Wood K. N., Dasgupta N. P., 2021, Journal of The Electrochemical Society, 168, 7, 070557

Dawson J. A., Attari T. S., Chen H., Emge S. P., Johnston K. E., Islam M. S., 2018, Energy and Environmental Science, 11, 10, 2993

Dawson J. A., Canepa P., Clarke M. J., Famprikis T., Ghosh D., Islam M. S., 2019, Chemistry of Materials, 31, 14, 5296

De Klerk N. J., Wagemaker M., 2018, ACS Applied Energy Materials, 1, 10, 5609

Delbeke J., Runge-Metzger A., Slingenberg Y., Werksman J., 2019, Towards a Climate-Neutral Europe: Curbing the Trend, 24–45

Delluva A. A., Delluva A. A., Dudoff J., et al., 2020, ACS Applied Materials and Interfaces, 12, 22, 24992

Devaux D., Harry K. J., Parkinson D. Y., et al., 2015, Journal of The Electrochemical Society, 162, 7, A1301

Dienemann L. L., Saigal A., Zimmerman M. A., 2021, Journal of Electrochemical Energy Conversion and Storage, 18, 4

Dietrich C., Weber D. A., Sedlmaier S. J., et al., 2017, Journal of Materials Chemistry A, 5, 34, 18111

Ding Y., Cano Z. P., Yu A., Lu J., Chen Z., 2019, Electrochemical Energy Reviews, 2, 1, 1

Dixit M. B., Harkey B. A., Shen F., Hatzell K. B., 2018a, Journal of The Electrochemical Society, 165, 5, F264

Dixit M. B., Park J. S., Kenesei P., Almer J., Hatzell K. B., 2021, Energy and Environmental Science, 14, 9, 4672

Dixit M. B., Regala M., Shen F., Xiao X., Hatzell K. B., 2018b, ACS Applied Materials & Interfaces, 11, 2022

Dixit M. B., Singh N., Horwath J. P., et al., 2020a, Matter, 3, 6, 2138

Dixit M. B., Verma A., Zaman W., et al., 2020b, ACS Applied Energy Materials, 3, 10, 9534

Dixit M. B., Zaman W., Bootwala Y., Zheng Y., Hatzell M. C., Hatzell K. B., 2019, ACS applied materials & interfaces, 11, 48, 45087

Dixit M. B., Zaman W., Hortance N., et al., 2020c, Joule, 4, 1, 207

Doux J. M., Nguyen H., Tan D. H., et al., 2020a, Advanced Energy Materials, 10, 1

Doux J. M., Yang Y., Tan D. H., et al., 2020b, Journal of Materials Chemistry A, 8, 10, 5049

Dudney N. J., 1985, Journal of the American Ceramic Society, 68, 10, 538

Duffner F., Kronemeyer N., Tübke J., Leker J., Winter M., Schmuch R., 2021, Nature Energy, 6, 2, 123

Dussart T., Rividi N., Fialin M., Toussaint G., Stevens P., 2021

Ebner M., Marone F., Stampanoni M., Wood V., 2013, Science, 342, November, 716

Energy Information Administration (EIA), 2013, , January

Famprikis T., Kudu O. U., Dawson J. A., et al., 2020, Journal of the American Chemical Society, 142, 43, 18422

Fang C., Lu B., Pawar G., et al., 2021, Nature Energy, 6, 10, 987

Fleig J., Pham P., Sztulzaft P., Maier J., 1998, 115, 739

Fu Z., Zhang L., Gritton J. E., et al., 2020, ACS Applied Materials and Interfaces, 12, 22, 24693

Gao X., Liu B., Hu B., et al., 2022, Joule, 6, 3, 636

Garcia-Mendez R., Smith J. G., Neuefeind J. C., Siegel D. J., Sakamoto J., 2020, Advanced Energy Materials, 10, 19

Ghidiu M., Ruhl J., Culver S. P., Zeier W. G., 2019, Journal of Materials Chemistry A, 7, 30, 17735

Gurevitch I., Buonsanti R., Teran A. A., et al., 2013, Journal of The Electrochemical Society, 160, 9, A1611

Gürsoy D., De Carlo F., Xiao X., Jacobsen C., 2014, J. Synchrotron Radiat., 21, 5, 1188

Hallinan D. T., Balsara N. P., 2013, Annual Review of Materials Research, 43, 503

Hamming L. M., Qiao R., Messersmith P. B., Brinson L. C., 2009, Composites science and technology, 69, 11-12, 1880

Han F., Westover A. S., Yue J., et al., 2019, Nature Energy, 4, 3, 187

Han X., Gong Y., Fu K., et al., 2017, Nature Materials, 16, 5, 572

Hänsel C., Kundu D., 2021, Advanced Materials Interfaces, 8, 10, 1

Hao S., Bailey J. J., Iacoviello F., et al., 2021, Advanced Functional Materials, 31, 10, 1

Harry K. J., Hallinan D. T., Parkinson D. Y., MacDowell A. A., Balsara N. P., 2014, Nature Materials, 13, 1, 69

Haslam C. G., Wolfenstine J. B., Sakamoto J., 2022, Journal of Power Sources, 520, December 2021, 230831

Hatz A. K., Calaminus R., Feijoo J., et al., 2021, ACS Applied Energy Materials, 4, 9, 9932

Hatzell K. B., Chen X. C., Cobb C. L., et al., 2020, ACS Energy Letters, 5, 3, 922

Hatzell K. B., Dixit M. B., Berlinger S. A., Weber A. Z., 2017, Journal of Materials Chemistry A, 5, 39, 20527

Hatzell K. B., Zheng Y., 2021, MRS Energy Sustainability, , 0123456789, 1

Heubner C., Maletti S., Auer H., et al., 2021, Advanced Functional Materials, 2106608

Hikima K., Totani M., Obokata S., Muto H., Matsuda A., 2022, ACS Applied Energy Materials, 5, 2, 2349

Hitz G. T., McOwen D. W., Zhang L., et al., 2019, Materials Today, 22, February, 50

Hlushkou D., Reising A. E., Kaiser N., et al., 2018, Journal of Power Sources, 396, June, 363

Hu M., Hu T., Li Z., et al., 2018, ACS Nano, 12, 4, 3578

Huang X., Lu Y., Guo H., et al., 2018, ACS Applied Energy Materials, 1, 10, 5355

Huo H., Liang J., Zhao N., et al., 2020, ACS Energy Letters, 5, 7, 2156

IEA, 2021, Global EV Outlook 2021, 101

Iwasaki S., Hamanaka T., Yamakawa T., et al., 2014, Journal of Power Sources, 272, 1086

Janek J., Zeier W. G., 2016a, Nature Energy, 1, 9, 1

Janek J., Zeier W. G., 2016b, Energy, 500, 400, 300

Jin L., Howlett P. C., Pringle J. M., et al., 2014, Energy and Environmental Science, 7, 10, 3352

Jin Y., Liu K., Lang J., et al., 2018, Nature Energy, 3, 9, 732

Judez X., Eshetu G. G., Li C., Rodriguez-Martinez L. M., Zhang H., Armand M., 2018, Joule, 2, 11, 2208

Kamaya N., Homma K., Yamakawa Y., et al., 2011, Nature materials, 10, 9, 682

Karabelli D., Birke K. P., Weeber M., 2021, Batteries, 7, 1

Kasemchainan J., Zekoll S., Spencer Jolly D., et al., 2019, Nature Materials, 18, 10, 1105

Kato Y., Hori S., Saito T., et al., 2016a, Nature Energy, 1, 4, 1

Kato Y., Hori S., Saito T., et al., 2016b, Nature Energy, 1, 4, 16030

Kato Y., Shiotani S., Morita K., Suzuki K., Hirayama M., Kanno R., 2018, Journal of Physical Chemistry Letters, 9, 3, 607

Kazyak E., Garcia-Mendez R., LePage W. S., et al., 2020a, Matter, 2, 4, 1025

Kazyak E., Shin M., Lepage W. S., Cho T. H., Dasgupta N. P., 2020b, Chemical Communications, 56, 99, 15537

Kendrick E., Islam M. S., Slater P. R., 2007, Journal of Materials Chemistry, 17, 30, 3104

Keplinger C., Sun J.-y., Foo C. C., Rothemund P., Whitesides G. M., Suo Z., 2013, 341, August, 984

Kerman K., Luntz A., Viswanathan V., Chiang Y.-M., Chen Z., 2017, Journal of The Electrochemical Society, 164, 7, A1731

Kim I., Park J., Nama T. H., et al., 2013, Journal of Power Sources, 244, 646

Kim K. J., Balaish M., Wadaguchi M., Kong L., Rupp J. L., 2021, Advanced Energy Materials, 11, 1, 1

Kim K. J., Rupp J. L., 2020, Energy & Environmental Science, 13, 12, 4930

Kim S., Jung C., Kim H., et al., 2020, Advanced Energy Materials, 10, 12, 1

Kinzer B., Davis A. L., Krauskopf T., et al., 2021, Matter, 4, 6, 1947

Koerver R., Aygün I., Leichtweiß T., et al., 2017, Chemistry of Materials, 29, 13, 5574

Koerver R., Zhang W., De Biasi L., et al., 2018, Energy and Environmental Science, 11, 8, 2142

Krauskopf T., Dippel R., Hartmann H., et al., 2019a, Joule, 3, 8, 2030

Krauskopf T., Hartmann H., Zeier W. G., Janek J., 2019b, ACS Applied Materials and Interfaces, 11, 15, 14463

Krauskopf T., Hartmann H., Zeier W. G., Janek J., 2019c, ACS Applied Materials and Interfaces, 11, 15, 14463

Krauskopf T., Mogwitz B., Hartmann H., Singh D. K., Zeier W. G., Janek J., 2020a, Advanced Energy Materials, 2000945

Krauskopf T., Richter F. H., Zeier W. G., Janek J., 2020b, Chemical Reviews

Krawiec W., Scanlon Jr L., Fellner J., Vaia R., Vasudevan S., Giannelis E., 1995, Journal of Power Sources, 54, 2, 310

Kudu Ö. U., Famprikis T., Fleutot B., et al., 2018, Journal of Power Sources, 407, October, 31

Kwak H., Han D., Lyoo J., et al., 2021, Advanced Energy Materials, 11, 12, 1

Lamb W. F., Wiedmann T., Pongratz J., et al., 2021, Environmental Research Letters, 16, 7

Larson J. M., Gillette E., Burson K., Wang Y., Lee S. B., Reutt-Robey J. E., 2018, Science advances, 4, 6, eaas8927

Lee C., Han S. Y., Lewis J. A., et al., 2021a, ACS Energy Letters, 6, 9, 3261

Lee M. J., Shin D. O., Kim J. Y., et al., 2021b, Energy Storage Materials, 37, February, 306

LePage W. S., Chen Y., Kazyak E., et al., 2019, Journal of The Electrochemical Society, 166, 2, A89

Lewis J., Javier F., Cortes Q., et al., 2020, , 2

Lewis J. A., Cortes F. J. Q., Liu Y., et al., 2021, Nature Materials, c

Lewis J. A., Javier F., Cortes Q., et al., 2019

Lewis J. A., Lee C., Liu Y., et al., 2022

Li J., Ma C., Chi M., Liang C., Dudney N. J., 2015, Advanced Energy Materials, 5, 4, 1401408

Li Q., Yi T., Wang X., et al., 2019a, Nano Energy, 63, July, 103895

Li Z., Huang H. M., Zhu J. K., et al., 2019b, ACS Applied Materials and Interfaces, 11, 1, 784

Liang J., Li X., Adair K. R., Sun X., 2021, Accounts of Chemical Research, 54, 4, 1023

Lin D., Liu Y., Cui Y., 2017, Nature Nanotechnology, 12, 3, 194

Liu B., Zhang L., Xu S., et al., 2018, Energy Storage Materials, 14, April, 376

Liu F., Bin F., Xue J., et al., 2020, ACS Applied Materials and Interfaces, 12, 20, 22710

Liu G., Shi J., Zhu M., et al., 2021, Energy Storage Materials, 38, March, 249

Liu S., Wang Q., 2002, Journal of Tribology, 124, 1, 36

Liu S., Wang Q., Liu G., 2000, Wear, 243, 1-2, 101

Liu S., Zhang J., Dong R., et al., 2016, Angewandte Chemie - International Edition, 55, 40, 12516

Liu W., Liu N., Sun J., et al., 2015, Nano Letters, 15, 4, 2740

Liu Z., Fu W., Payzant E. A., et al., 2013, Journal of the American Chemical Society, 135, 3, 975

Lobe S., Bauer A., Uhlenbruck S., Fattakhova-Rohlfing D., 2021, Advanced Science, 8, 11, 1

Loho C., Djenadic R., Bruns M., Clemens O., Hahn H., 2017, Journal of The Electrochemical Society, 164, 1, A6131

Lu Y., Das S. K., Moganty S. S., Archer L. A., 2012, Advanced Materials, 24, 32, 4430

Lu Y., Huang X., Ruan Y., Wang Q., Kun R., Wen Z., 2018, 18853–18858

Luo W., Gong Y., Zhu Y., et al., 2016, Journal of the American Chemical Society, 138, 37, 12258

Ma X., Xu Y., 2022, Electrochimica Acta, 409, 139986

MacFarlane D. R., Huang J., Forsyth M., 1999, Nature, 402, 6763, 792

Manthiram A., Yu X., Wang S., 2017a, Nature Reviews Materials, 2, 4, 1

Manthiram A., Yu X., Wang S., 2017b, Nature Reviews Materials, 2, 4, 16103

Masias A., Felten N., Garcia-Mendez R., Wolfenstine J., Sakamoto J., 2019, Journal of Materials Science, 54, 3, 2585

Maslyn J. A., Loo W. S., Mcentush K. D., et al., 2018

Mauger A., Armand M., Julien C. M., Zaghib K., 2017, Journal of Power Sources, 353, 333

Meesala Y., Jena A., Chang H., Liu R. S., 2017, ACS Energy Letters, 2, 12, 2734

Menkin S., Okeefe C. A., Gunnarsdóttir A. B., et al., 2021, Journal of Physical Chemistry C, 125, 30, 16719

Miara L., Windmüller A., Tsai C. L., et al., 2016, ACS Applied Materials and Interfaces, 8, 40, 26842

Miara L. J., Richards W. D., Wang Y. E., Ceder G., 2015, Chemistry of Materials, 27, 11, 4040

Minnmann P., Quillman L., Burkhardt S., Richter F. H., Janek J., 2021, Journal of The Electrochemical Society, 168, 4, 040537

Mistry A., Mukherjee P. P., 2020, Journal of the Electrochemical Society, 167, 8, 082510

Miura A., Rosero-Navarro N. C., Sakuda A., et al., 2019, Nature Reviews Chemistry, 3, 3, 189

Moreno D., Bootwala Y., Tsai W.-Y., et al., 2018, Environmental Science & Technology Letters, 5, 12, 745

Motoyama M., Ejiri M., Iriyama Y., 2015, Journal of The Electrochemical Society, 162, 13, A7067

Motoyama M., Hirota M., Yamamoto T., Iriyama Y., 2020, ACS Applied Materials and Interfaces, 12, 34, 38045

Mu M., Schmieg J., Dierickx S., et al., 2022, 2

Muy S., Voss J., Schlem R., et al., 2019, iScience, 16, 270

Ning Z., Jolly D. S., Li G., et al., 2021, Nature Materials

Notten P. H., Roozeboom F., Niessen R. A., Baggetto L., 2007, Advanced Materials, 19, 24, 4564

Nykvist B., Nilsson M., 2015, Nature Climate Change, 5, 4, 329

Oh D. Y., Kim D. H., Jung S. H., Han J. G., Choi N. S., Jung Y. S., 2017, Journal of Materials Chemistry A, 5, 39, 20771

Oh D. Y., Kim K. T., Jung S. H., et al., 2021, Materials Today, xxx, xx, 37

Ohashi A., Kodama M., Xueying S., et al., 2020, Journal of Power Sources, 470, March, 228437

Ohno S., Bernges T., Buchheim J., et al., 2020, ACS Energy Letters, 5, 3, 910

Olabi A. G., Abdelkareem M. A., 2022, Renewable and Sustainable Energy Reviews, 158, January, 112111

Palenstijn W. J., Batenburg K. J., Sijbers J., 2011, Journal of Structural Biology, 176, 2, 250

Pandian A. S., Chen X. C., Chen J., et al., 2018, Journal of Power Sources, 390, 153

Park C. H., Park M., Yoo S. I., Joo S. K., 2006, Journal of Power Sources, 158, 2 SPEC. ISS., 1442

Park K., Yu B. C., Jung J. W., et al., 2016, Chemistry of Materials, 28, 21, 8051

Pfenninger R., Struzik M., Garbayo I., Stilp E., Rupp J. L., 2019, Nature Energy, 4, 6, 475

Pharr M., Suo Z., Vlassak J. J., 2014, Journal of Power Sources, 270, 569

Ping W., Wang C., Lin Z., et al., 2020, Advanced Energy Materials, 10, 25, 1

Popovic J., 2021a, Macromolecular Chemistry and Physics, 2100344, 1

Popovic J., 2021b, Nature Communications, 12, 1, 8

Popovic J., Brandell D., Ohno S., Hatzell K. B., Zheng J., Hu Y. Y., 2021, Journal of Materials Chemistry A, 9, 10, 6050

Porz L., Swamy T., Sheldon B. W., et al., 2017, 1701003, 1

Qiao R., Deng H., Putz K. W., Brinson L. C., 2011a, Journal of Polymer Science Part B: Polymer Physics, 49, 10, 740

Qiao R., Deng H., Putz K. W., Brinson L. C., 2011b, 740–748

Randau S., Weber D. A., Kötz O., et al., 2020, Nature Energy, 5, 3, 259

Riegger L. M., Schlem R., Sann J., Zeier W. G., Janek J., 2021, Angewandte Chemie, 133, 12, 6792

Rivers M. L., 2012, in Proc. SPIE, vol. 8506, 85060U

Roman H. E., 1990, Journal of Physics: Condensed Matter, 2, 17, 3909

Saccoccio M., Yu J., Lu Z., et al., 2017, Journal of Power Sources, 365, 43

Salvatierra R. V., Chen W., Tour J. M., 2021, Advanced Energy and Sustainability Research, 2, 5, 2000110

Sastre J., Lin T. Y., Filippin A. N., et al., 2019, ACS Applied Energy Materials, 2, 12, 8511

Sastre J., Priebe A., Döbeli M., Michler J., Tiwari A. N., Romanyuk Y. E., 2020, Advanced Materials Interfaces

Schaefer J. L., Moganty S. S., Yanga D. A., Archer L. A., 2011, Journal of Materials Chemistry, 21, 27, 10094

Schiffer Z. J., Manthiram K., 2017, Joule, 1, 1, 10

Schlenker R., Stępień D., Koch P., et al., 2020, ACS applied materials interfaces, 12, 17, 20012

Schleussner C. F., Rogelj J., Schaeffer M., et al., 2016, Nature Climate Change, 6, 9, 827

Schneider C. A., Rasband W. S., Eliceiri K. W., 2012, Nature Methods, 9, 7, 671

Schnell J., Günther T., Knoche T., et al., 2018, Journal of Power Sources, 382, February, 160

Schnell J., Knörzer H., Imbsweiler A. J., Reinhart G., 2020, Energy Technology, 8, 3

Schnell J., Tietz F., Singer C., Hofer A., Billot N., Reinhart G., 2019, Energy and Environmental Science, 12, 6, 1818

Schwietert T. K., Arszelewska V. A., Wang C., et al., 2020, Nature Materials, 19, 4, 428

Schwöbel A., Hausbrand R., Jaegermann W., 2015, Solid State Ionics, 273, 51

Scrosati B., 2001, The Chemical Record, 1, 2, 173

Sebastian M. T., Jantunen H., 2010, International Journal of Applied Ceramic Technology, 7, 4, 415

Seitzman N., Guthrey H., Sulas D. B., Platt H. A. S., Al-Jassim M., Pylypenko S., 2018, Journal of The Electrochemical Society, 165, 16, A3732

Shao Y., Wang H., Gong Z., et al., 2018, ACS Energy Letters, 3, 6, 1212

Sharafi A., Haslam C. G., Kerns R. D., Wolfenstine J., Sakamoto J., 2017a, Journal of Materials Chemistry A, 5, 40, 21491

Sharafi A., Haslam C. G., Kerns R. D., Wolfenstine J., Sakamoto J., 2017b, Journal of Materials Chemistry A, 5, 40, 21491

Sharafi A., Meyer H. M., Nanda J., Wolfenstine J., Sakamoto J., 2016, Journal of Power Sources, 302, 135

Shen F., Dixit M. B., Xiao X., Hatzell K. B., 2018a, ACS Energy Letters, 3, 4, 1056

Shen F., Dixit M. B., Xiao X., Hatzell K. B., 2018b, ACS Energy Letters, 3, 4, 1056

Shen F., Dixit M. B., Zaman W., Hortance N., Rogers B., Hatzell K. B., 2019a, Journal of The Electrochemical Society, 166, 14, A3182

Shen F., Dixit M. B., Zaman W., Hortance N., Rogers B., Hatzell K. B., 2019b, Journal of The Electrochemical Society, 166, 14, A3182

Shen F., Guo W., Zeng D., et al., 2020, ACS applied materials interfaces, 12, 27, 30313

Shi T., Tu Q., Tian Y., et al., 2020a, Advanced Energy Materials, 10, 1, 1902881

Shi T., Zhang Y.-Q., Tu Q., Wang Y., Scott M., Ceder G., 2020b, Journal of Materials Chemistry A, 8, 34, 17399

Spencer Jolly D., Ning Z., Hartley G. O., et al., 2021, ACS Applied Materials Interfaces, 13, 19, 22708

Sripad S., Viswanathan V., 2017, ACS Energy Letters, 2, 7, 1669

Stephan A. M., Nahm K., 2006, Polymer, 47, 16, 5952

Stöffler H., Zinkevich T., Yavuz M., et al., 2019, Journal of Physical Chemistry C, 123, 16, 10280

Su J., Huang X., Song Z., et al., 2019, Ceramics International, 45, 12, 14991

Swamy T., Chen X., Chiang Y. M., 2019, Chemistry of Materials, 31, 3, 707

Tan D. H., Xu P., Yang H., et al., 2020a, MRS Energy & Sustainability, 7

Tan D. H. S., Xu P., Yang H., et al., 2020b, MRS Energy Sustainability, 7, 1, 1

Taylor N. J., Stangeland-Molo S., Haslam C. G., et al., 2018, Journal of Power Sources, 396, June, 314

Tenhaeff W. E., Yu X., Hong K., Perry K. A., Dudney N. J., 2011, Journal of the Electrochemical Society, 158, 10, A1143

Tewari D., Mukherjee P. P., 2020, The Journal of Physical Chemistry C, 0–29

Tian H. K., Liu Z., Ji Y., Chen L. Q., Qi Y., 2019, Chemistry of Materials, 31, 18, 7351

Tominaga Y., Yamazaki K., 2014, Chemical communications, 50, 34, 4448

Tominaga Y., Yamazaki K., Nanthana V., 2015, Journal of the Electrochemical Society, 162, 2, A3133

Tsai C. L., Ma Q., Dellen C., et al., 2019, Sustainable Energy and Fuels, 3, 1, 280

Tu Q., Barroso-Luque L., Shi T., Ceder G., 2020, Cell Reports Physical Science, 1, 7, 100106

Tzika P., Boyce M., Parks D., 2000, Journal of the Mechanics and Physics of Solids, 48, 9, 1893

van Aarle W., Palenstijn W. J., De Beenhouwer J., et al., 2015, Ultramicroscopy, 157, 2015, 35

Vaselabadi S. A., Shakarisaz D., Ruchhoeft P., Strzalka J., Stein G. E., 2016, Journal of Polymer Science, Part B: Polymer Physics, 54, 11, 1074

Villaluenga I., Wujcik K. H., Tong W., et al., 2016, Proceedings of the National Academy of Sciences, 113, 1, 52

Wang C. W., Ren F. C., Zhou Y., et al., 2021a, Energy and Environmental Science, 14, 1, 437

Wang D., Sun Q., Luo J., et al., 2019a, ACS Applied Materials and Interfaces, 11, 5, 4954

Wang D., Wu X., Wang Z., Chen L., 2005, Journal of Power Sources, 140, 1, 125

Wang H., Gao H., Chen X., et al., 2021b, Advanced Energy Materials, 11, 42, 1

Wang M., Wolfenstine J. B., Sakamoto J., 2019b, Electrochimica Acta, 296, 842

Wang M. J., Carmona E., Gupta A., Albertus P., Sakamoto J., 2020a, Nature Communications, 11, 1, 1

Wang M. J., Chang J. Y., Wolfenstine J. B., Sakamoto J., 2020b, Materialia, 12, June, 100792

Wang M. J., Choudhury R., Sakamoto J., 2019c, Joule, 3, 9, 2165

Wang M. J., Kazyak E., Dasgupta N. P., Sakamoto J., 2021c, Joule, 5, 6, 1371

Wang Q., Liu B., Shen Y., et al., 2021d, Advanced Science, 8, 17, 1

Wang S., Zhang Y., Zhang X., et al., 2018, ACS Applied Materials and Interfaces, 10, 49, 42279

Wang W., Yi E., Fici A. J., Laine R. M., Kieffer J., 2017, The Journal of Physical Chemistry C, 121, 5, 2563

Wang Y., Zanelotti C. J., Wang X., et al., 2021e, Nature Materials, 20, 9, 1255

Wenzel S., Leichtweiss T., Krüger D., Sann J., Janek J., 2015a, Solid State Ionics, 278, 98

Wenzel S., Leichtweiss T., Krüger D., Sann J., Janek J., 2015b, Solid State Ionics, 278, 98

Wenzel S., Sedlmaier S. J., Dietrich C., Zeier W. G., Janek J., 2018, Solid State Ionics, 318, 102

Wenzel S., Weber D. A., Leichtweiss T., Busche M. R., Sann J., Janek J., 2016, Solid State Ionics, 286, March, 24

Wood K. N., Noked M., Dasgupta N. P., 2017, ACS Energy Letters, 2, 3, 664

Wu B., Yang Y., Liu D., et al., 2020, Journal of The Electrochemical Society, 166, 16, A4141

Xiao Y., Turcheniuk K., Narla A., et al., 2021, Nature Materials

Xu C., Ahmad Z., Aryanfar A., Viswanathan V., Greer J. R., 2017, Proceedings of the National Academy of Sciences of the United States of America, 114, 1, 57

Xu L., Lu Y., Zhao C. Z., et al., 2021a, Advanced Energy Materials, 11, 4

Xu L., Lu Y., Zhao C. Z., et al., 2021b, Advanced Energy Materials, 11, 4

Xu P., Dai Q., Gao H., et al., 2020, Joule, 4, 12, 2609

Xu R., Liu F., Ye Y., et al., 2021c, Advanced Materials, 33, 49, 1

Xu X., Hou G., Nie X., et al., 2018, Journal of Power Sources, 400, August, 212

Yan H., Tantratian K., Ellwood K., et al., 2022, Advanced Energy Materials, 12, 2, 1

Yan K., Wang J., Zhao S., et al., 2019, Angewandte Chemie, 131, 33, 11486

Yang C., Zhang L., Liu B., et al., 2018, 1–6

Yang L., Tao X., Huang X., et al., 2021a, ACS Applied Materials and Interfaces, 13, 47, 56054

Yang L., Tao X., Huang X., et al., 2021b, ACS Applied Materials and Interfaces, 13, 47, 56054

Yang X., Adair K. R., Gao X., Sun X., 2021c, Energy and Environmental Science, 14, 2, 643

Yu H. C., Taha D., Thompson T., et al., 2019, Journal of Power Sources, 440, July, 227116

Yu S., Schmidt R. D., Garcia-Mendez R., et al., 2016, Chemistry of Materials, 28, 1, 197

Yu T., Liang J., Luo L., et al., 2021, Advanced Energy Materials, 11, 36, 1

Yu X., Manthiram A., 2020, ACS Applied Materials and Interfaces

Zahiri B., Patra A., Kiggins C., et al., 2021, Nature Materials

Zaman W., Hatzell K. B., 2022, Current Opinion in Solid State and Materials Science, 26, 4, 101003

Zaman W., Hortance N., Dixit M. B., De Andrade V., Hatzell K. B., 2019, Journal of Materials Chemistry A, 7, 41, 23914

Zhang J., Lu B., Song Y., Ji X., 2012, Journal of Power Sources, 209, 220

Zhang R., Fujimori S., 2020, Environmental Research Letters, 15, 3

Zhang W., Nie J., Li F., Wang Z. L., Sun C., 2018a, Nano Energy, 45, January, 413

Zhang W., Schröder D., Arlt T., et al., 2017a, Journal of Materials Chemistry A, 5, 20, 9929

Zhang X., Liu T., Zhang S., et al., 2017b, Journal of the American Chemical Society, 139, 39, 13779

Zhang X., Wang Q. J., Harrison K. L., et al., 2019, Journal of The Electrochemical Society, 166, 15, A3639

Zhang X., Wang Q. J., Harrison K. L., Roberts S. A., Harris S. J., 2020, Cell Reports Physical Science, 1, 2, 100012

Zhang Z., Chen S., Yang J., et al., 2018b, ACS applied materials & interfaces, 10, 3, 2556

Zhao C., Sun Q., Luo J., et al., 2020, Chemistry of Materials, 32, 23, 10113

Zhao C. Z., Zhang X. Q., Cheng X. B., et al., 2017, Proceedings of the National Academy of Sciences of the United States of America, 114, 42, 11069

Zhao L., Wang Q. J., Zhang X., et al., 2022, Journal of Power Sources, 531, March, 231305

Zheng H., Wu S., Tian R., et al., 2020, Advanced Functional Materials, 30, 6, 1

Zheng J., Hu Y.-Y., 2018, ACS applied materials & interfaces, 10, 4, 4113

Zheng J., Tang M., Hu Y.-Y., 2016a, Angewandte Chemie International Edition, 55, 40, 12538

Zheng J., Tang M., Hu Y. Y., 2016b, Angewandte Chemie - International Edition, 55, 40, 12538

Zheng J., Wang P., Liu H., Hu Y., 2019, ACS Applied Energy Materials

Zhou Q., Xu B., Chien P. H., et al., 2020, Small Methods, 9, 1

Zhu X., Wang K., Xu Y., et al., 2021, Energy Storage Materials, 36, January, 291

Zou P., Sui Y., Zhan H., et al., 2021, Chemical Reviews, 121, 10, 5986